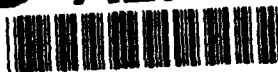


AD-A278 682



Final Technical Report C94-02
Contract F29601-92-C-0005

February 7, 1994

DTIC
ELECTE
APR 29 1994
S F D

Center for Seismic Studies
Final Technical Report
October 1992 - October 1993

Anne Henson
Hans Israelsson

APPROVED FOR RELEASE
DISTRIBUTION UNLIMITED

This document has been approved
for public release and sale; its
distribution is unlimited.



Science Applications International Corporation
Center for Seismic Studies
1300 N. 17th Street, Suite 1450
Arlington, VA 22209

DTIC QUALITY ASSURED 3
94-13040





ADVANCED RESEARCH PROJECTS AGENCY
3701 NORTH FAIRFAX DRIVE
ARLINGTON, VA 22203-1714



April 20, 1994

Ms. Lynne Adams
PKVA (505-846-5935 x136)
Department of the Air Force
Phillips Laboratory
Kirtland Air Force Base, NM 87117-6008

SUBJECT: Approval for Unlimited Distribution
Center for Seismic Studies, Final Technical Report, October 1992-October 1993
Report C94-02
Contract No. F29601-92-C-0005

ARPA/NMRO has carefully reviewed the subject technical report submitted by Science Applications International Corporation under the subject contract, and has certified that this report contains no critical or sensitive data, information or technology. As a result of this investigation, the report is approved for public release, distribution unlimited.

The contractor shall include a copy of this letter with each copy of the subject report released to individuals or organizations outside of the US Government or their contractors, as documentation that the contents have been reviewed and that unlimited distribution of the report has been approved.

The procedure described above is consistent with the distribution procedures specified in the subject contract. Please let me know if you have any questions.

Steven R. Bratt
Program Manager
Nuclear Monitoring Research Office



4 28

14

REPORT DOCUMENTATION PAGE			Form Approved OMB No. 0704-0188	
<small>Public reporting burden for this collection of information is estimated to average 1 hour per response, including the time for reviewing instructions, searching existing data sources, gathering and maintaining the data needed, and completing and reviewing the collection of information. Send comments regarding this burden estimate or any other aspect of this collection of information, including suggestions for reducing this burden, to Washington Headquarters Services, Directorate for Information Operations and Reports, 1215 Jefferson Davis Highway, Suite 1204, Arlington, VA 22202-4302, and to the Office of Management and Budget, Paperwork Reduction Project (0704-0188), Washington, DC 20503.</small>				
1. AGENCY USE ONLY (Leave blank)	2. REPORT DATE February 7, 1994	3. REPORT TYPE AND DATES COVERED Technical October 92 - October 93		
4. TITLE AND SUBTITLE Center for Seismic Studies Final Technical Report October 1992 - October 1993		5. FUNDING NUMBERS F29601-92-C-0005		
6. AUTHOR(S) Anne Henson Hans Israelsson				
7. PERFORMING ORGANIZATION NAME(S) AND ADDRESS(ES) Science Applications International Corporation Center for Seismic Studies 1300 N. 17th Street, Suite 1450 Arlington, VA 22209		8. PERFORMING ORGANIZATION REPORT NUMBER C94-02		
9. SPONSORING/MONITORING AGENCY NAME(S) AND ADDRESS(ES) Advanced Research Projects Agency 3701 N. Fairfax Drive Arlington, VA 22203		10. SPONSORING/MONITORING AGENCY REPORT NUMBER		
11. SUPPLEMENTARY NOTES				
12a. DISTRIBUTION/AVAILABILITY STATEMENT Approved for Public Release Distribution Unlimited			12b. DISTRIBUTION CODE	
13. ABSTRACT (Maximum 200 words) A 1992 study by Suteau-Henson where azimuth bias and scatter were systematically measured for regional phases of events recorded at ARCESS is extended here by mapping the observed bias and scatter around ARCESS. In another study, the optimization of polarization analysis at IMS/IRIS stations in the Former Soviet Union is addressed. Also in this report, a procedure to stack waveforms recorded by a network of seismic stations for detection of depth phases, sP and pP is defined. The constraint on focal depth provided by origin times determined from travel time ratios of P and S waves is also studied. Finally, we perform some computational experiments to outline the depth estimation capability of the GSETT-2 global network and a hypothetical network consisting primarily of high sensitive array stations.				
14. SUBJECT TERMS Scatter Waveforms GSETT-2 ARCESS Depth Phases Polarization Analysis Focal Depth			15. NUMBER OF PAGES 106	
			16. PRICE CODE	
17. SECURITY CLASSIFICATION OF REPORT UNCLASSIFIED	18. SECURITY CLASSIFICATION OF THIS PAGE UNCLASSIFIED	19. SECURITY CLASSIFICATION OF ABSTRACT UNCLASSIFIED	20. LIMITATION OF ABSTRACT NONE	

Table of Contents

Mapping Azimuth Bias and Scatter Around ARCESS	11
Introduction	11
Observations of Azimuth Bias and Scatter	11
Mapping the Observations	13
Interpolating the Observations	15
Comparison of F-K and 3-C Pn Azimuth Bias	15
Discussion	20
References	20
 Optimization of Polarization Analysis at the IMS/IRIS	
Stations in the Former Soviet Union	23
Introduction	23
Exploration of the Parameter Space	24
Performance Comparison for Phase Identification	26
S / P / T Classification	26
S / P / T / N Classification	26
Performance Comparison for Azimuth Estimation	29
Combined Optimization	32
Conclusions.....	35
Acknowledgments	35
References.....	36
 Stacking of Waveforms for Depth Estimation	37
Introduction	37
Data	37
Depth Traces	39
Frequency filtering	39
Binary trace	39
Masking of PcP window	42
Transformation into depth traces	42
Stacking of Binary Traces and Candidate Depths	42
Applicability	46
Comparison of Candidate and NEIS Depths	50
Earthquake Source Radiation Pattern and Depth Phases.....	50
Concluding Remarks	52
References	56
 Constraining Origin Time with S/P Travel Time Ratios	
and Depth Estimation	57
Constraining Origin Time With S/P Travel Time Ratio	57

Accession For	
NTIS	CRA&I <input checked="" type="checkbox"/>
DTIC	TAB <input type="checkbox"/>
Unannounced <input type="checkbox"/>	
Justification	
By	
Distribution /	
Availability Codes	
Dist	Avail and/or Special
A-1	

Ts/Tp Ratios From IMS Data	62
Examples of Depth Estimation Using IMS Data	69
Concluding Remarks	73
References.....	73

Assessing Depth Estimation Capability: Examples

for Global Networks	77
Introduction	77
The Networks	77
Depth Estimation and Simulations	79
Surface Reflected Phases - Moveout and Azimuthal Coverage	81
Depth Errors Using S Phases	84
Concluding Remarks	91
References.....	93

List of Figures

- Figure 1. The distribution of f-k azimuth as a function of signal-to-noise ratio is plotted for the Pn, Pg, Sn, and Lg phases of events from the mining area north of Apatity (Kola Peninsula), located at ARCESS. For each plot, the dotted line denotes the mean of the observations, while the dashed line corresponds to the actual azimuth. The lines marked by squares represent 2 standard deviations, as fitted by an exponential decay with constant rate. 12
- Figure 2. The azimuth bias (f-k azimuth minus true azimuth) is plotted for the four regional phases, Pn, Pg, Sn, Lg, from events corresponding to the mine locations in Table 1 and recorded at ARCESS. The circles denote negative bias, and the crosses denote positive bias. The symbol size is proportional to the amount of bias. The location of the ARCESS array is shown by a triangle. The arc represents a distance of 500 km from the array. 14
- Figure 3. The standard deviation of the f-k azimuth for a signal-to-noise ratio of 10 is plotted for the four regional phases, Pn, Pg, Sn, Lg, from events corresponding to the mine locations in Table 1 and recorded at ARCESS. The symbol size is proportional to the standard deviation in (the maximum is 10). The location of the ARCESS array is shown by a triangle. The arc represents a distance of 500 km from the array. 16
- Figure 4. The observations of azimuth bias in Figure 2 were interpolated and extrapolated to cover a regular latitude and longitude grid (with increments 0.5 in longitude and 0.25 in latitude). The resulting values (in) are displayed on contour plots for the four regional phases, Pn, Pg, Sn, and Lg. 17
- Figure 5. The observations of azimuth scatter in Figure 3 (standard deviation in for an SNR of 10) were interpolated and extrapolated to cover a regular latitude and longitude grid (with increments 0.5 in longitude and 0.25 in latitude). The resulting values are displayed on contour plots for the four regional phases, Pn, Pg, Sn, and Lg. 18
- Figure 6. The azimuth bias is plotted for Pn from events corresponding to the mine locations in Table 1 and recorded at ARCESS. At the top, the difference between the f-k azimuth and the mine azimuth is plotted, while at the bottom is shown the difference between the azimuth from polarization of 3-component data (from Suteau-Henson, 1992b) and the mine azimuth. The circles denote negative bias, and the crosses denote positive bias. The symbol size is proportional to the amount of bias. The location of the ARCESS array is shown by a triangle. The arc represents a distance of 500 km from the array. 19

Figure 7. The phase identification performance (percentage of correctly identified detections) is displayed for eleven polarization recipes (described in the text and Table 3) at each of five IMS/IRIS stations. Detections in the three groups regional S, regional P, and teleseismic were classified. For each station, the standard recipe (S), the optimum recipe for azimuth estimation from Riviere-Barbier *et al.* (1992), when it applies, and the preferred recipe from this experiment are highlighted.27

Figure 8. The phase identification performance (percentage of correctly identified detections) is displayed for eleven polarization recipes (described in the text and Table 3) at station ARU. Detections in the three phase groups, regional S, regional P, and Teleseismic, were classified. In spite of somewhat lower overall performance (see Figure 7), recipe A3 is preferred to K3 due to its higher success rate for the regional P group.28

Figure 9. The phase identification performance (percentage of correctly identified detections) is displayed for each of the four groups (regional S, regional P, Teleseismic, and Noise), and their average, at each of five IMS/IRIS stations. The results are shown for the standard recipe "S", the optimum recipe "A" for azimuth estimation (from Riviere-Barbier *et al.*, 1992) when it applies, and the best recipe "B" obtained for the S / P / T classification problem.30

Figure 10. The distributions of azimuth residuals (azimuth from polarization minus azimuth from *NEIC* location) of teleseismic P arrivals are displayed for eleven polarization recipes (described in the text and Table 3), at each of four IMS/IRIS stations.31

Figure 11. The combined performance for phase identification and azimuth estimation is displayed for a set of eleven polarization recipes (described in the text and Table 3), at four IMS/IRIS stations. The classification problem considered is the separation of regional S, regional P, and teleseismic detections.33

Figure 12. The combined performance for phase identification and azimuth estimation is displayed for four of the IMS/IRIS stations. The data set used for phase identification included all four detection groups (regional S, regional P, Teleseismic, and Noise). At each station, the performance was estimated for the standard recipe S, the optimum recipe for azimuth estimation from Riviere-Barbier *et al.* (1992), when it applied, and a selected subset of recipes that performed well for the S / P / T combined optimization experiment (see Figure 11). The resulting preferred recipes are highlighted.34

Figure 13. The map shows the geographical distribution of the events and the seismic stations for which waveform data were analyzed. The two underground nuclear explosions in the South Pacific are marked with crosses.	38
Figure 14. The signal processing and transformation in the time domain, upper frame, and in the depth domain, lower frame. The time domain processing involves bandpass filtering to enhance the signal-to-noise ratio, forming of a STA/LTA trace, masking of window for expected arrival time of PcP, and transformation into a binary trace. The binary trace in the time domain is mapped into two binary traces in the depth domain, one each for pP and sP.	40
Figure 15. The scatter diagrams shows the ratios of the periods of pP/P, to the left, and of sP/P to the right, as a function of the delay times.	41
Figure 16. STA/LTA traces plotted as a function of epicentral distance for all the waveforms. Only the parts of the traces with the STA/LTA above the threshold, 1.75, were marked as black dots.	43
Figure 17. The figure shows waveforms and binary traces sections for three events in the Afghanistan-USSR border region on : (a) 91/05/13 at 23:55:33.7, (b) 91/04/26 at 22:24:05.3, and (c) 91/05/13 08:32:43.8. Station codes and epicentral distances are indicated to the right of each waveform. The waveform sections also include, at the top, envelope stacks of pP and sP as a function of depth and the standard deviation of the first arrival time P residuals as a function of depth (SIGMA P RES in the diagrams). The signal-to-noise ratio, SNR, and the P residual for the NEIS hypocenter solution are shown to the right for each waveform.	44
Figure 18. (a) The figure shows how the candidate depth is defined from a pP depth trace stack.	47
Figure 18. (b) The barplot shows the number of events with and without candidate depth as a function of depths reported by NEIS. Most of the NEIS depths were constrained to 33 km and a significant portion of those had candidate depths.	48
Figure 19. The geographical distribution in the Western (a) and Eastern (b) hemispheres of events with and without candidate depths.	49

Figure 20. Success rates, given as percentages, to define candidate depths as a function of the number of waveforms and azimuthal coverage. Azimuthal coverage is given as the number of 45 degree sectors around the source to station azimuth for which there is one or more station with waveform data.51

Figure 21. Depths taken as the average of the lower and upper values of the candidate depths ('pP DEPTHS' in the diagrams) compared with NEIS depths. Comparisons are made as a function of the number of phases in the stacked trace, 1, 2, 3, and more than 3. Somewhat arbitrarily, a difference of 20 km between the two types of depth is accepted for agreement ('agree.' given as percentages in the diagrams).53

Figure 22. Comparison of theoretical and observed amplitude ratios pP/P and sP/P for the event on 91/04/26 17:36:59 with latitude 7.40 N and longitude 126.71 E and mb(NEIS)=5.5.54

Figure 23. Correlation coefficients for observed and theoretical pP/P and sP/P amplitude ratios plotted against the difference between pP delay time and source duration for GSETT-2 events that were recorded at more than 5 stations.55

Figure 24. The derivative dT/dh as a function of distance for depths between 12 and 75 km.58

Figure 25. The ratio for travel times of S and P as a function of epicentral distances for different velocity models.60

Figure 26. Comparisons of the standard deviations of the depth estimates obtained with and without constrained origin times for two synthetic examples, with recorded phases of Pn and Sn as illustrated by the maps to the left. 61

Figure 27. Comparisons of origin times calculated from travel time ratios of S and P waves and the associated estimates of the travel time ratios.63

Figure 28. Standard deviation of origin time for different standard deviations in the S/P. from 0.1 to 1 per cent, as a function of epicentral distance. The curves were obtained with a Gaussian random number generator with the standard deviations of the P and S arrival times being 0.7 and 1.4 s, respectively.64

Figure 29. Empirical distribution functions of Pn and Sn arrival time residuals for IMS data. The lines represent approximations to Gaussian distributions; the dashed and solid lines correspond to robust and conventional estimates of the standard deviations (SD1 and SD2 respectively).65

Figure 30. Epicenters of the events that were analyzed and the locations of the mini arrays.	66
Figure 31. Epicenters of the Steigen earthquakes determined by the Bergen Seismological Observatory.	67
Figure 32. Comparison of Pn and Sn residuals of the Steigen earthquakes.	68
Figure 33. Empirical distribution functions of the S/P travel time ratios to ARA0, FIA0, and NRA0 for the Steigen earthquakes.	70
Figure 34. Comparison of depth estimates obtained with a free depth and with origin time constrained with the S/P travel time ratio.	71
Figure 35. Histograms of depths for possible earthquakes and mining events determined with conventional free depth method and with origin times constrained with S/P travel time ratio.	72
Figure 36. The 90% detection thresholds of the GSETT-2 network (a), the ALPHA network (b), and a network consisting of the ALPHA stations and 50 oceanic stations (c).	78
Figure 37. The 50% detection thresholds of the teleseismic window for station in the GSETT-2 and ALPHA networks and a network consisting of the ALPHA stations and 50 oceanic stations.	80
Figure 38. Median of the moveout observed of the total possible moveout in the distance range 30 to 90 degrees (in per cent) as a function of ganitude, mb, or median of the detection thresholds (see Fig 36a-b)	82
Figure 39. Median of azimuthal coverage given as the percentage of 8, 45 degree azimuth sectors in which the event was detected for the GSETT-2 and the ALPHA network. The shaded zones represent the median of the detection thresholds (see Fig 36a-b).	83
Figure 40. The ratio of depth errors from determinations with only P waves and with both P and S waves.	85
Figure 41. Median of depth error as a function of mb for estimates based on P and S waves for three networks: GSETT-2, ALPHA, and ALPHA + a 50 station oceanic network. The shaded zones represent the median of the detection thresholds (see Fig 36a-b).	86

Figure 42. Upper limit of depth error as a function of mb for estimates based on P and S waves for three networks: GSETT-2, ALPHA, and ALPHA + a 50 station oceanic network. The shaded zones represent the median of the detection thresholds (see Fig 36a-b).87

Figure 43. The difference in detection thresholds (90%) for detecting both P and S waves, and only P waves at three stations.89

Figure 44. Comparison of the difference between the 90% depth error and the actual depth with mb (to the left) and with the actual depth (to the right) for simulated events. Plus signs and open circles are used for events with the difference less than and greater than 0 and the two types of events are separated with a dashed horizontal line. The full vertical lines in the left frame correspond to the range of the detection thresholds for the ALPHA network.90

Figure 45. The geographical distribution of the simulated events.92

List of Tables

Table 1. Mine Locations	13
Table 2. Number of Detections in Data Set	24
Table 3. Description of Recipes	25
Table 4. Event source parameters and depth estimates	74

Mapping Azimuth Bias and Scatter Around ARCESS

Anne Suteau-Henson

Introduction

Azimuth biases of events located by arrays are well documented (e.g., Mykkeltveit *et al.*, 1990; Vogfiord and Langston, 1992). To our knowledge, however, no attempt has been made to use such knowledge to appropriately correct, and thereby improve, event locations by automated systems such as the *Intelligent Monitoring System* (IMS, Bache *et al.*, 1990).

In a previous Report (Suteau-Henson, 1992b), variations of azimuth residuals, from both polarization and f-k analysis, were studied as a function of azimuth and distance for events recorded at the NORESS and ARCESS arrays by the IMS. In another study (Suteau-Henson, 1992a), the azimuth bias and scatter were systematically measured for regional phases of events recorded at ARCESS. The latter study is extended here by mapping the observed bias and scatter. They apparently are slowly varying in the area surrounding the array, and can be approximated by a smooth surface, through interpolation and extrapolation of the observations. The result is tables of azimuth corrections and azimuth weights (inversely proportional to the amount of scatter for a given signal-to-noise ratio) for each regional phase, covering a latitude and longitude grid around ARCESS. Such tables can then be used to improve automated locations by the IMS, in the same way traveltimes correction tables are used to improve distance estimates.

Observations of Azimuth Bias and Scatter

A model was proposed by Suteau-Henson (1992a), to fit the statistical distribution of azimuth estimates from f-k analysis for regional phases from specific event clusters around ARCESS. It was shown that for events associated with a given mine (or mining area), the distribution of azimuth as a function of signal-to-noise ratio (SNR) could be described by its mean (usually different from the "true" mine azimuth and phase-specific), and by its SNR-dependent standard deviation (usually phase-specific). The SNR-dependence of the standard deviation could be fitted by an exponential decay. Such fits to the data are shown, as an example, for events from the mining area north of Apatity in Figure 1. To simplify modelling of the standard deviation, a constant decay rate was assumed for all seismic phases and the entire area around ARCESS. Such a simple model fits the data reasonably well.

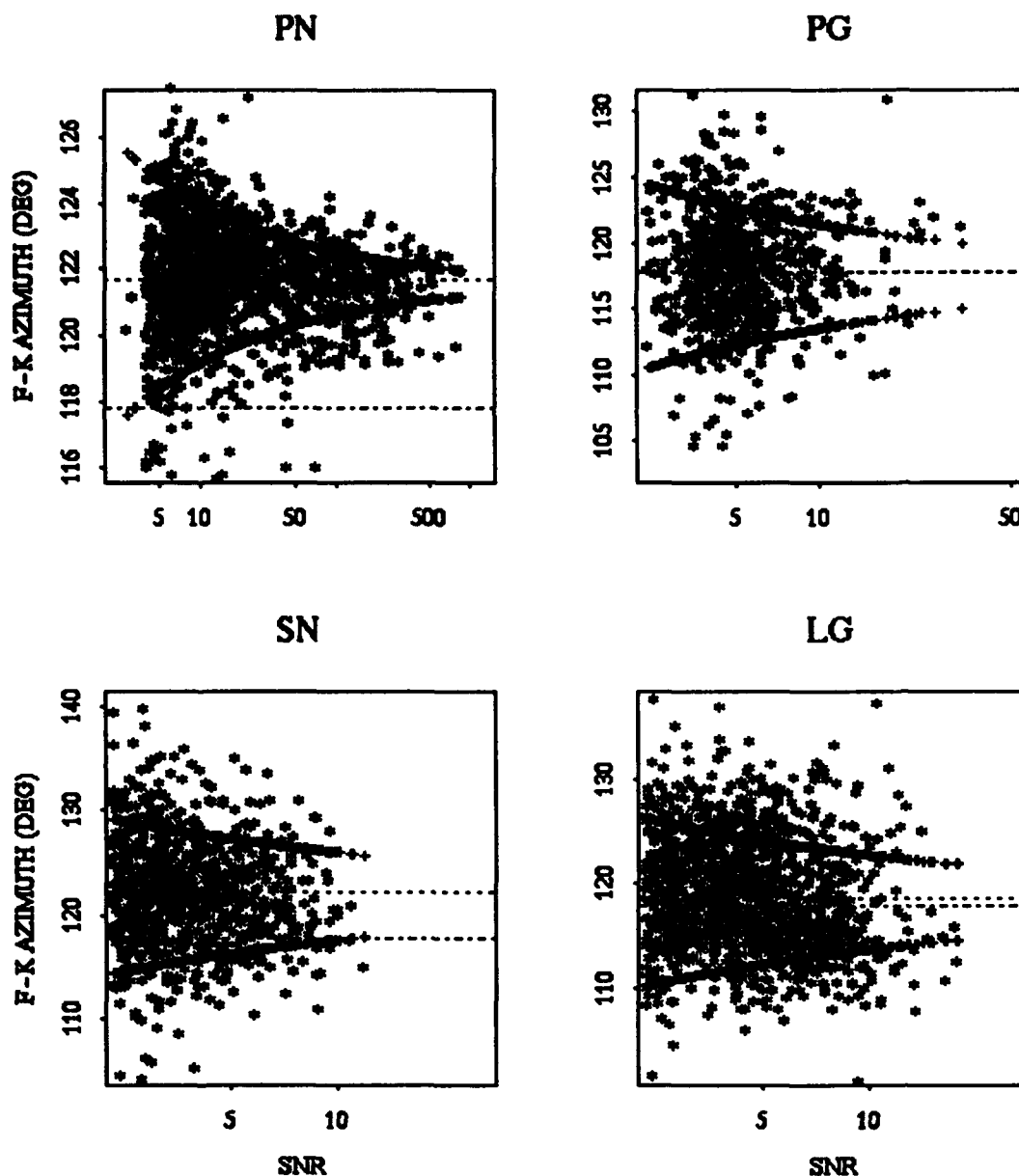


Figure 1: The distribution of f-k azimuth as a function of signal-to-noise ratio is plotted for the Pn, Pg, Sn, and Lg phases of events from the mining area north of Apatity (Kola Peninsula), located at ARCESS. For each plot, the dotted line denotes the mean of the observations, while the dashed line corresponds to the actual azimuth. The lines marked by squares represent ± 2 standard deviations, as fitted by an exponential decay with constant rate.

The data set used for this study covers two years of IMS operation (from November 1, 1990 to November 1, 1992). The locations of the mines (or mining areas) for which azimuth bias and scatter were thus measured are given in Table 1. The locations are those

Table 1: Mine Locations

Mine or Mining Area	Latitude N	Longitude E
Kiruna ^a	67.833	20.205
Malmberget / Aitik	67.15	20.785
Saattopora	67.79	24.43
Varanger ^b	70.48	28.50
Nikel	69.42	30.80
Olenogorsk	68.16	33.18
Apatity	67.645	33.87
Kovdor	67.56	30.44
Elijaervi	65.78	24.70

a. A. Dahle (personal communication)

b. S. Mykkeltveit (personal communication)

from the Helsinki University (M. Uski, personal communication), unless noted otherwise.

Event clusters that were not in the vicinity of a known mine or quarry were not included. Clusters of events that could be associated with any of several mines spanning a wide azimuth range could not be used. For mining areas with several closely spaced mines (e.g., Malmberget/Aitik, Apatity), the average location is given in Table 1.

Mapping the Observations

In Figure 2 the observations of azimuth bias (observed azimuth minus "true" azimuth) at the nine mine locations in Table 1 are plotted on a map of the area around ARCESS for each of the four regional phases, Pn, Pg, Sn, and Lg. Although the resulting distribution differs with each phase type, some general trends are observed:

- The azimuth bias tends to be negative southwest and south of the array, and positive east, northeast and southeast of the array;

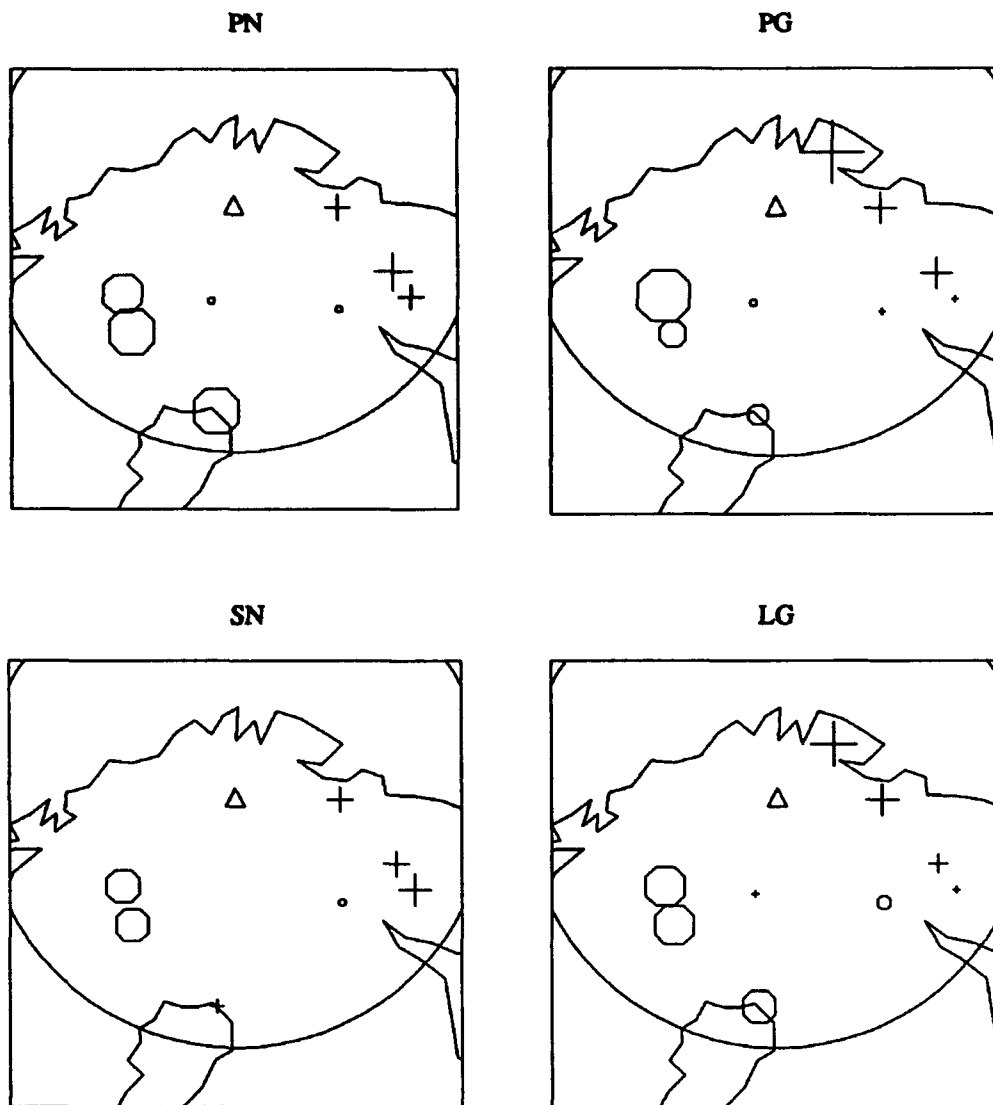


Figure 2: The azimuth bias ($f-k$ azimuth minus true azimuth) is plotted for the four regional phases, Pn, Pg, Sn, Lg, from events corresponding to the mine locations in Table 1 and recorded at ARCESS. The circles denote negative bias, and the crosses denote positive bias. The symbol size is proportional to the amount of bias. The location of the ARCESS array is shown by a triangle. The arc represents a distance of 500 km from the array.

- The azimuth bias varies smoothly over the area around ARCESS, remaining within 10° .

Similar maps are shown in Figure 3 for the observed azimuth scatter. As the scatter is a function of SNR, the values plotted arbitrarily correspond to the standard deviation (in $^\circ$) for an SNR of 10.

Interpolating the Observations

As the variations of azimuth bias and scatter around ARCESS are generally slow, they can be fitted by a smooth surface. Interpolation and extrapolation of the observations mapped in Figures 2 and 3 were performed, resulting in values of azimuth bias and scatter covering a regular latitude and longitude grid around ARCESS. The contour plots of Figures 4 and 5 display these values for the bias and scatter, respectively. Note that the results for the Sn phase are less reliable, due to sparse observations. The figures show that:

- The azimuth bias varies smoothly from about -10° to the southwest to about $+10^\circ$ to the northeast.
- Apart from a low near Saattopora (standard deviation less than 3°), the azimuth scatter is characterized by larger gradients for the P-type than for the S-type phases. Pn to the north and Pg to the northeast have large standard deviations (from 5 to 12°). The Lg scatter is larger to the south (more than 5°). Elsewhere, the standard deviation is less than 4° for all phases at this SNR level. Note, however, that for a given magnitude, the SNR of secondary phases is always relatively low (as it is measured against the coda), so that on average, standard deviations for S-type phases are typically larger than those shown in Figure 5.

Comparison of F-K and 3-C Pn Azimuth Bias

In an attempt to obtain corroborating evidence for the observed azimuth bias from f-k analysis, the azimuth bias from polarization analysis of three-component data was similarly measured for the Pn phase at the locations in Table 1. The data set used was that from Suteau-Henson (1992b) which is about four times smaller than that used for the f-k studies (hence, resulting in greater uncertainties) and not overlapping with it. The f-k and 3-component (3-C) Pn azimuth biases are compared in Figure 6. There is a good qualitative agreement between the two sets of observations.

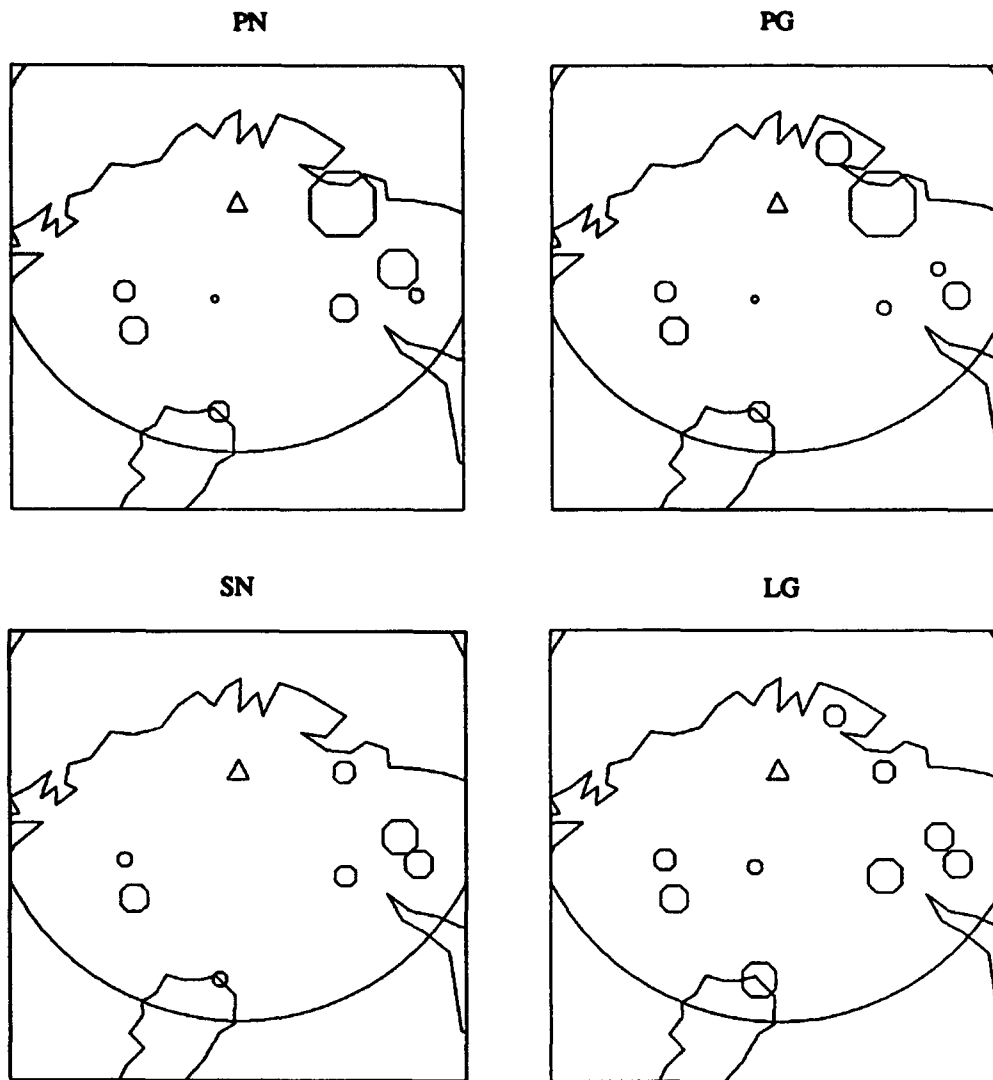


Figure 3: The standard deviation of the f-k azimuth for a signal-to-noise ratio of 10 is plotted for the four regional phases, Pn, Pg, Sn, Lg, from events corresponding to the mine locations in Table 1 and recorded at ARCESS. The symbol size is proportional to the standard deviation in $^{\circ}$ (the maximum is 10°). The location of the ARCESS array is shown by a triangle. The arc represents a distance of 500 km from the array.

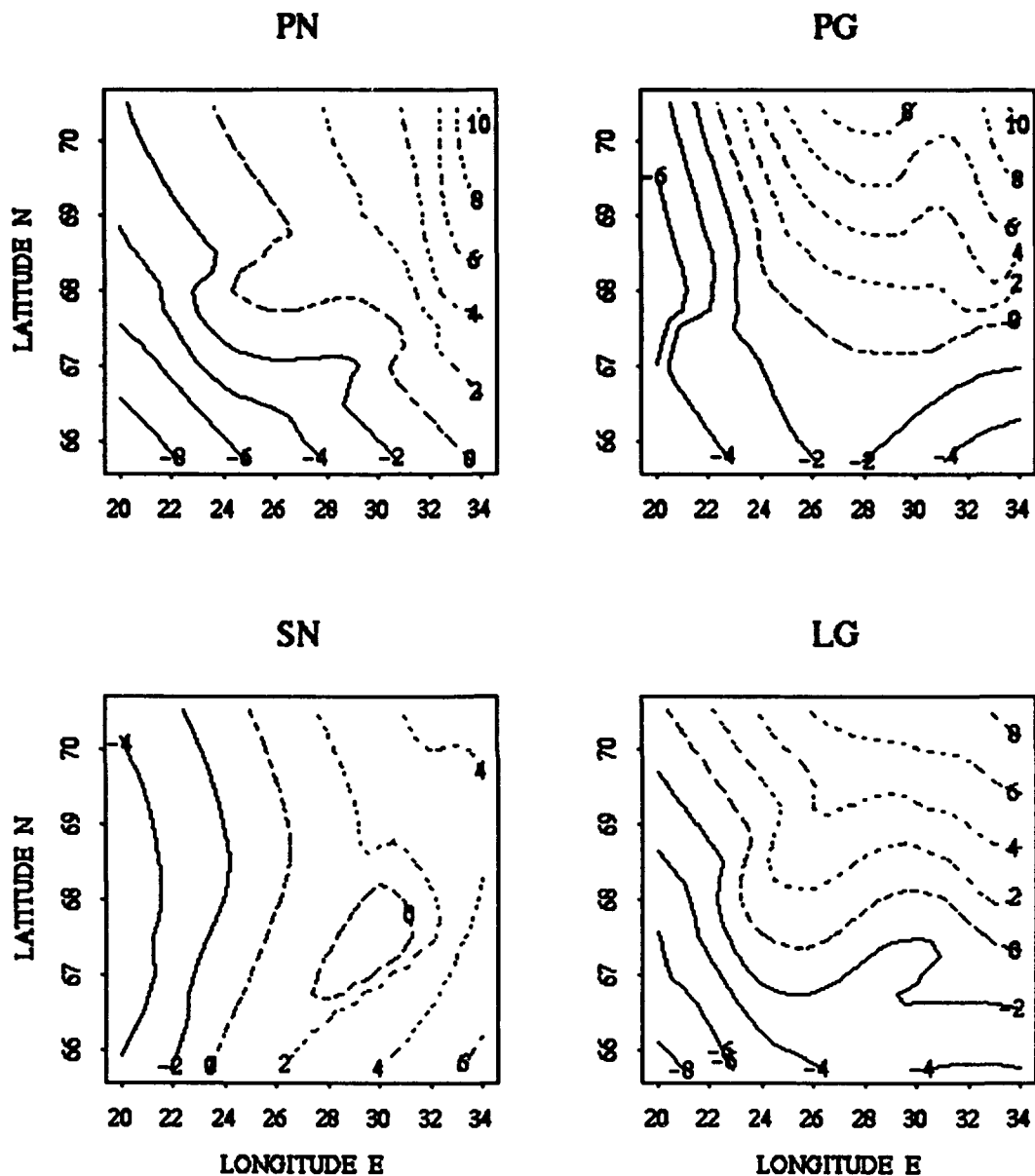


Figure 4: The observations of azimuth bias in Figure 2 were interpolated and extrapolated to cover a regular latitude and longitude grid (with increments 0.5° in longitude and 0.25° in latitude). The resulting values (in $^\circ$) are displayed on contour plots for the four regional phases, Pn, Pg, Sn, and Lg.

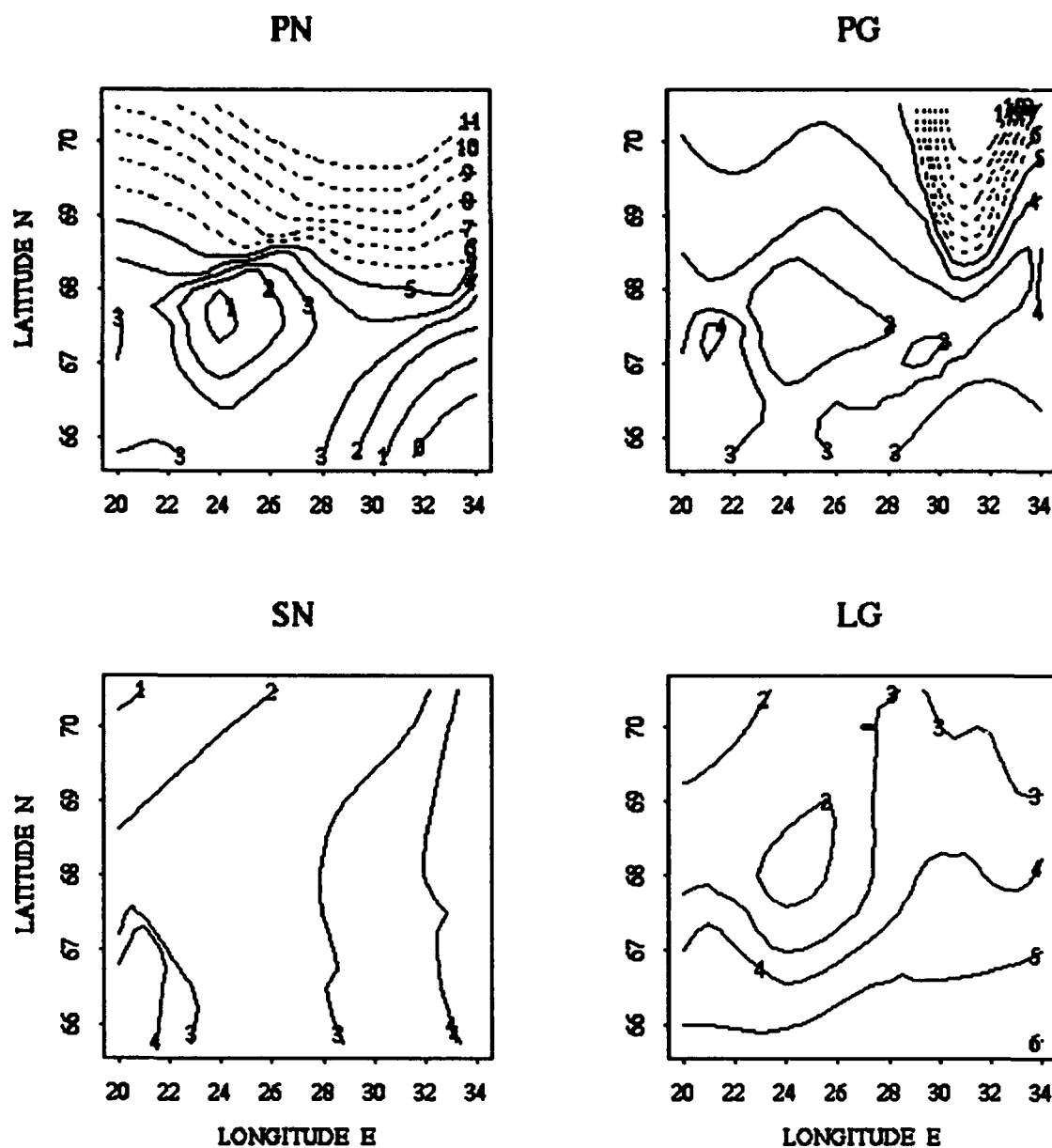


Figure 5: The observations of azimuth scatter in Figure 3 (standard deviation in $^{\circ}$ for an SNR of 10) were interpolated and extrapolated to cover a regular latitude and longitude grid (with increments 0.5° in longitude and 0.25° in latitude). The resulting values are displayed on contour plots for the four regional phases, Pn, Pg, Sn, and Lg.

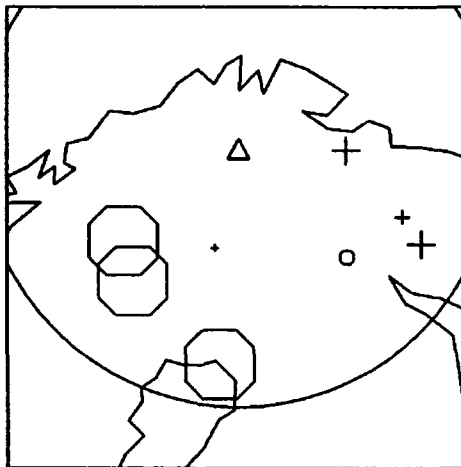
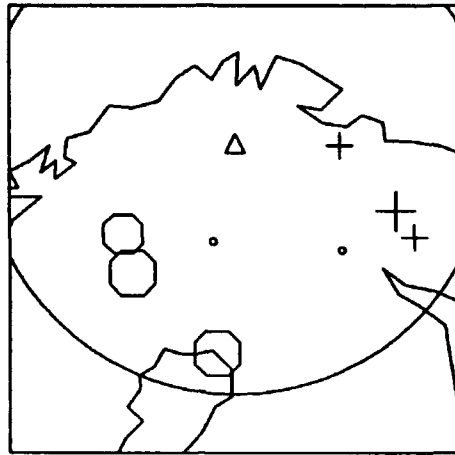


Figure 6: The azimuth bias is plotted for Pn from events corresponding to the mine locations in Table 1 and recorded at ARCESS. At the top, the difference between the f-k azimuth and the mine azimuth is plotted, while at the bottom is shown the difference between the azimuth from polarization of 3-component data (from Suteau-Henson, 1992b) and the mine azimuth. The circles denote negative bias, and the crosses denote positive bias. The symbol size is proportional to the amount of bias. The location of the ARCESS array is shown by a triangle. The arc represents a distance of 500 km from the array.

Discussion

Our observations of azimuth bias around ARCESS are in agreement with the study by Vogfjord and Langston (1992). They carefully analyzed the ARCESS recordings of a few large events from known mines. They found biases for the azimuths from f-k analysis, that generally depended on phase type. For example, PmP and SmS of events from the quarry on the Varanger peninsula showed an azimuth 5° larger than that of the Pg and Sg crustal phases. The phase identification used in this study is that currently in use in the IMS and does not include Moho reflections. For close events such as those from the Varanger quarry, the f-k analysis window for the Pg phase includes both the crustal phase (Pg) and the intensive Moho reflection (PmP), which explains why the P-phase azimuth has a large positive bias (Vogfjord, personal communication). A similar explanation can be given for the S-phase bias. Vogfjord and Langston (1992) speculate that the observed biases are due to lateral heterogeneities, that affect phases differently, depending on their path and frequency content. Thurber *et al.* (1991) modelled the amount of bias produced by different kinds of heterogeneities (dipping Moho, velocity gradients at different depths in the crust and upper mantle), as well as the distance range and azimuth span affected. A better understanding of the relation between laterally heterogeneous structure and azimuth bias would help predict bias in areas with known structure, but sparse seismicity or little "ground truth".

In Fennoscandia, more knowledge has been acquired about location of specific events, through a correlation of the event identification given in the Helsinki Bulletin (i.e., association with a particular mine) and that resulting from a cluster analysis (Riviere-Barbier, 1993). A result of this study is a set of well-controlled events that will further constrain estimates of azimuth bias.

Mapping observations of azimuth bias and scatter as demonstrated here makes it possible to build azimuth-correction tables and weight tables that can be used in the IMS to improve automated locations.

References

- Bache, T. C., S. R. Bratt, J. Wang, R. M. Fung, C. Kobryn, and J. W. Given (1990). The Intelligent Monitoring System, *Bull. Seism. Soc. Am.* **80**, 1833-1851.
- Mykkeltveit, S., F. Ringdal, T. Kvaerna, and R. W. Alewine (1990). Application of Regional Arrays in Seismic Verification Research, *Bull. Seism. Soc. Am.* **80**, 1777-1800.
- Riviere-Barbier, F. (1993). Constructing a Reference Event List for ARCESS, *Center for Seismic Studies Special Report*, CSS 93-03.

- Suteau-Henson, A. (1992a). Improvement of Azimuth Estimation in the IMS, in *Center for Seismic Studies Semiannual Technical Report*, March-October 1992, CSS 92-04, 25-43.
- Suteau-Henson, A. (1992b). Azimuth Variations at NORESS and ARCESS, in *Center for Seismic Studies Semiannual Technical Report*, March-October 1992, CSS 92-04, 81-91.
- Thurber, C. H., C. G. Munson, and S. R. Bratt (1991). Arrival azimuth Bias at Fennoscandian Arrays (unpublished manuscript).
- Vogfjord, K. S. and C. A. Langston (1992). Short-Period Regional Phases from Fennoscandian Arrays, in *Papers Presented at 14th Annual PL/DARPA Seismic Research Symposium*, 16-18 September 1992, Tucson, AZ, 450-456.

Optimization of Polarization Analysis at the IMS/IRIS Stations in the Former Soviet Union

Anne Suteau-Henson

Introduction

This study is part of an effort to integrate data from six three-component (3-C) IRIS/IDA stations in the former Soviet Union, AAK, ARU, GAR, KIV, OBN and TLY, within the automated processing of the *Intelligent Monitoring System* (IMS, Bache *et al.*, 1990). This contribution consisted of optimizing the measurement of polarization attributes at each station, for use in phase identification and azimuth estimation. In a previous study (Riviere-Barbier *et al.*, 1992), the capabilities for phase identification were investigated at four of the stations (ARU, GAR, KIV, and OBN), using polarization measurements obtained with one "recipe" (i.e., set of processing parameters) for all stations. This recipe was adapted from that used in the IMS for the Scandinavian arrays. Station-specific recipes, significantly different from the "standard" recipe, were found to optimize azimuth estimation.

In this study, optimization of phase identification at each station is addressed. The parameter space for polarization analysis is explored, and the performance of the resulting recipes is compared. A similar experiment is carried out for azimuth estimation. Finally, the possibility of a combined optimization of phase identification and azimuth estimation is considered. For each station, one single recipe can be selected that jointly optimizes both, thus considerably simplifying the automated processing.

The data set consists of the detections from automated processing of continuous data covering the period July 6 - 25, 1991. At each station, the detections were divided into four groups: Regional S ("S"), Regional P ("P"), Teleseismic ("T"), and Noise ("N"), based on the identification given by the analyst who reviewed the data. The data set is described in Table 2. Not enough data were available at OBN for this study. At ARU, a large noise detection group was reduced to a size of 60 to make it commensurate with the other groups at that station (the statistical method used to classify the detections works best for groups of similar sizes). Except for AAK and GAR, the statistical results must be considered as preliminary due to small populations.

Table 2: Number of Detections in Data Set

Station	Regional S	Regional P	Teleseismic	Noise	All
AAK	261	254	156	56	727
ARU	35	20	123	60	238
GAR	364	341	149	203	1057
KIV	101	79	62	47	289
TLY	67	52	104	54	277

Exploration of the Parameter Space

For each detection in the data set, polarization analysis was performed to obtain polarization measurements for a set of recipes, including the standard recipe used for the IMS arrays. The following processing parameters were varied:

- the frequency bands to include in the analysis;
- the length of overlapping time windows in which to measure polarization near the detection;
- the amount of overlap between time windows;
- the length of the waveform segment analyzed around the detection;
- the time delay between the beginning of the segment and the onset of the detection.

Other parameters (length and positioning of pre-detection noise segment) were shown to have little effect in previous studies (Riviere-Barbier *et al.*, 1992). For the new recipes, the length of the filter taper was increased, and the SNR threshold (determining the frequency bands selected for the analysis) was set higher, compared to their values in the standard recipe. The method for automated polarization analysis is described in greater detail in Suteau-Henson (1991).

In order to compare the performance of various recipes for phase identification, classical discriminant analysis was performed as a method of classification. Polarization measurements were used as predictors, along with dominant frequency and signal-to-noise ratio (SNR). Two problems were considered:

- classification of the three signal groups (S / P / T), not including coda detections;
- classification of all detection groups (i.e., including coda detections and the noise detection group).

As the first problem is less computationally-intensive, it could be investigated with a larger set of recipes. Eleven different recipes were tried and are described in Table 3.

Table 3: Description of Recipes

Recipe	Freq. Band (Hz)	Window Length (sec)	Overlap	Segment Length (sec)	Onset Delay (sec)	Filter Taper (sec)	SNR Thresh.
S	1-4	2	0.5	8	4	0.5	1.5
A1	0.5-2	1.5	0.5	5	0.5	5	2
A2	0.5-4	1.5	0.5	5	0.5	5	2
A3	0.5-8	1.5	0.5	5	0.5	5	2
G1	1-2	1	0.5	3	1	5	2
G2	1-4	1	0.5	3	1	5	2
G3	1-8	1	0.5	3	1	5	2
K1	0.5-2	1.5	0.75	3	0.5	5	2
K2	0.5-4	1.5	0.75	3	0.5	5	2
K3	0.5-8	1.5	0.75	3	0.5	5	2
A4	0.5-8	1.5	0.5	5	1	5	2

Exploring the effect of frequency band was emphasized. A previous study (Riviere-Barbier *et al.*, 1992) showed that the best recipes for azimuth estimation did not include any frequencies above 2 Hz. On the other hand, wide-band recipes perform better for phase identification, as expected since higher frequencies afford better discrimination between regional and teleseismic P, in particular. The eleven recipes can be briefly described as follows:

- (8) Standard Recipe (S),
- (9) ARU Azimuth Recipe (A1), i.e., as optimized by Riviere-Barbier *et al.* (1992) for station ARU,
- (10) Same as (2), but including the 2-4 Hz band (A2),
- (11) Same as (3), but including the 4-8 Hz band (A3),
- (12) GAR Azimuth Recipe (G1),
- (13) Same as (5), but including the 2-4 Hz band (G2),
- (14) Same as (6), but including the 4-8 Hz band (G3),

- (15) KIV Azimuth Recipe (K1),
- (16) Same as (8), but including the 2-4 Hz band (K2),
- (17) Same as (9), but including the 4-8 Hz band (K3),
- (18) Same as (4), but with different positioning of the waveform segment (A4).

Note that, although the higher frequency band included is 4-8 Hz, in practice, an anti-aliasing filter applied to the data strongly attenuates frequencies above 5 Hz.

Performance Comparison for Phase Identification

S / P / T Classification

The first experiment attempted to separate regional S, regional P, and teleseismic detections, using polarization measurements and dominant frequency as predictors. The results are shown in Figure 7, in terms of overall performance at each station for each recipe. The following observations can be made:

- The performance for phase identification of the recipes that were previously found to optimize azimuth estimation for ARU, GAR, and KIV ("azimuth recipes", from Riviere-Barbier *et al.*, 1992) is poor, especially at GAR and KIV, confirming our previous results.
- At all stations except ARU, where the success rate is low regardless of recipe, adding the 2-4 Hz band to the analysis improves the performance.
- At KIV and TLY, results are further improved by adding the 4-8 Hz band.
- The "GAR recipes" (G1, G2, G3) that do not include the 0.5-1 Hz "teleseismic" band, perform poorly at AAK and GAR.
- The performance of the standard recipe S (that includes frequencies from 1 to 4 Hz) is generally average, but poor at TLY.

The resulting preferred recipes for each station are all wide-band and include frequencies up to 8 Hz. At a given station, several recipes often had similar overall performance. In such a case, their relative performance for the different phase groups was considered. The recipe that performed best for regional P was preferred. For example, Figure 8 shows the performance at ARU for each phase group and each recipe, and illustrates the selection of recipe A3 rather than K3 at this station.

S / P / T / N Classification

Coda detections were included in each of the three phase groups, and the noise detection group was added to the data set in a more realistic test of the polarization parameters for phase identification. Also, SNR was included in the set of predictors. At each sta-

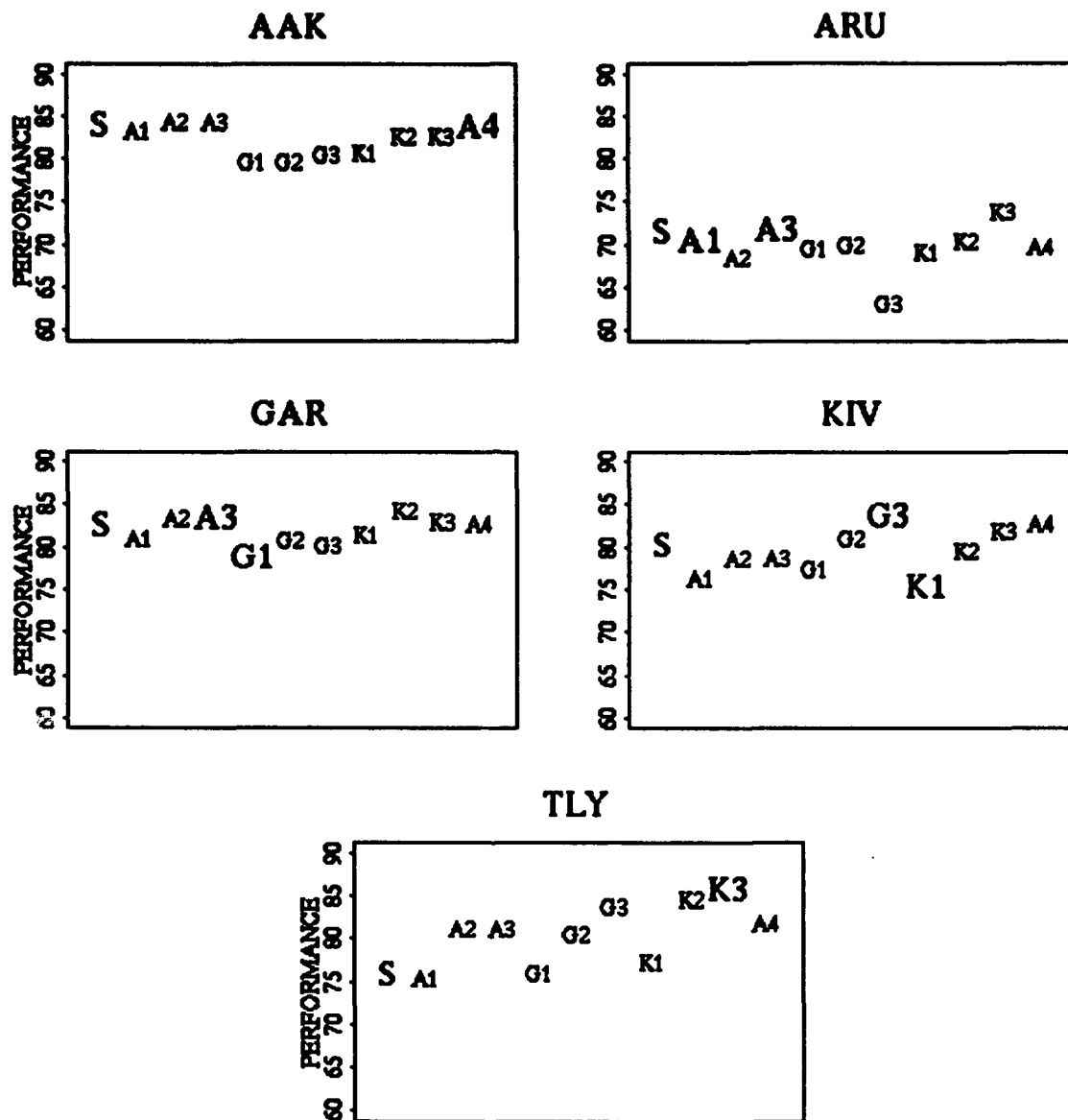


Figure 7: The phase identification performance (percentage of correctly identified detections) is displayed for eleven polarization recipes (described in the text and Table 3) at each of five IMS/IRIS stations. Detections in the three groups regional S, regional P, and teleseismic were classified. For each station, the standard recipe (S), the optimum recipe for azimuth estimation from Riviere-Barbier et al. (1992), when it applies, and the preferred recipe from this experiment are highlighted.

ARU

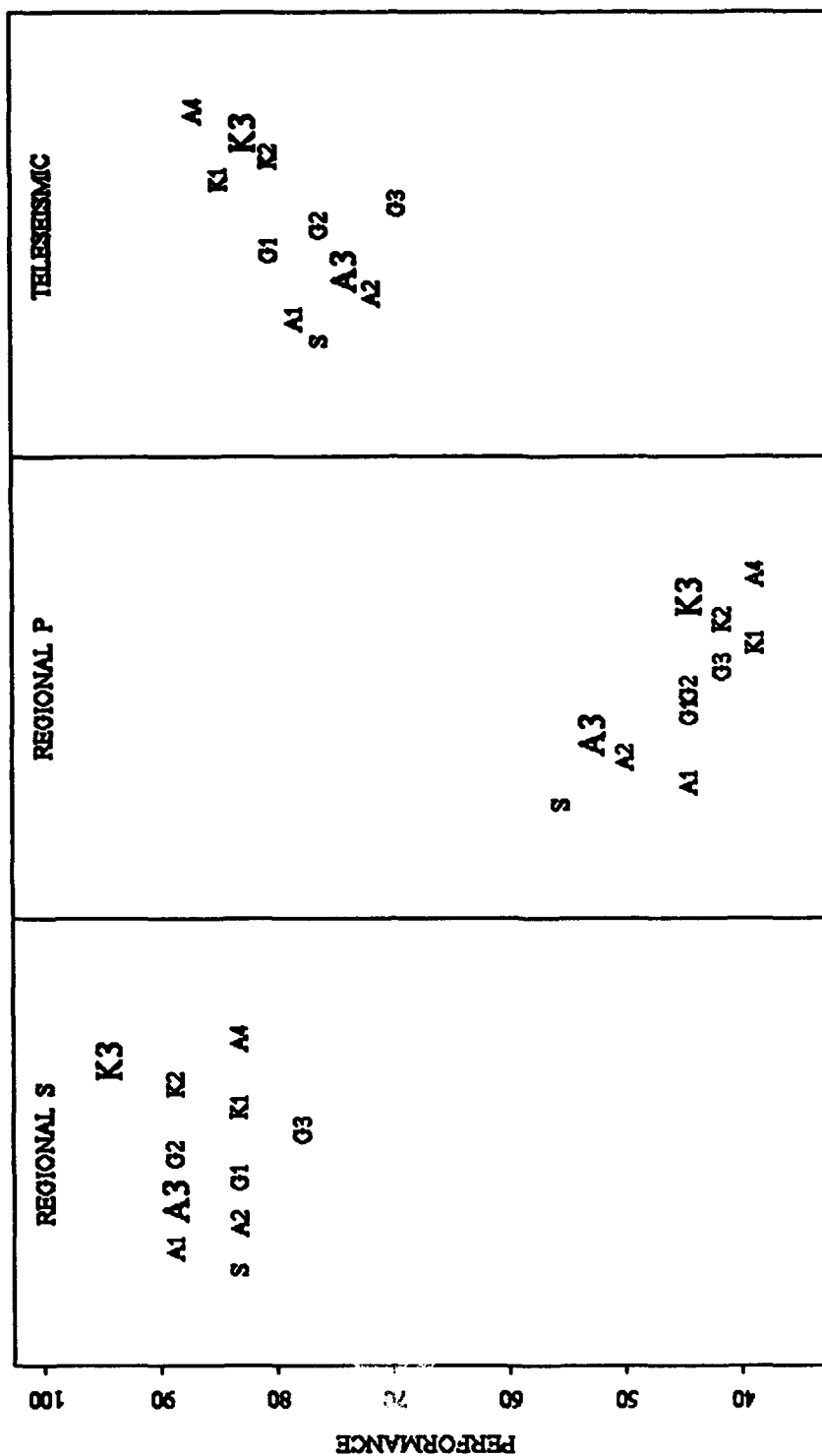


Figure 8: The phase identification performance (percentage of correctly identified detections) is displayed for eleven polarization recipes (described in the text and Table 3) at station ARU. Detections in the three phase groups, regional S, regional P, and Teleseismic, were classified. In spite of somewhat lower overall performance (see Figure 7), recipe A3 is preferred to K3 due to its higher success rate for the regional P group.

tion, the performance for each of the four detection groups, as well as the overall performance, were compared for three recipes: the standard recipe (S), the azimuth recipe (A) when available for this station, and the "best" recipe (B) obtained in the previous experiment. The results are displayed in Figure 9 and show the following:

- The low-frequency azimuth recipes (A) have a low overall classification rate as in the previous test, along with a poor performance for regional P.
- The high-frequency recipe B outperforms the standard recipe S at TLY, and has a comparable overall performance at the other stations.
- At all stations except ARU, the B recipes classify regional P detections better than the standard recipe.

Therefore, at each station except ARU, the "best" recipe from the previous experiment still qualifies as the preferred recipe for phase identification when all detections are included in the test. Its advantage over the standard recipe is particularly evident at TLY.

Performance Comparison for Azimuth Estimation

The performance for azimuth estimation of the set of eleven recipes was compared at each station. The data sets used for this study were obtained by matching the event origins after analyst review with origins from the *NEIC* Bulletin. Azimuth residuals (observed azimuth from polarization minus azimuth from the *NEIC* location) were calculated for teleseismic P arrivals. Figure 10 describes the distribution of azimuth residuals at AAK, ARU, GAR, and TLY for each recipe. At KIV, very poor results were obtained regardless of recipe, because of the assumption of rectilinear (instead of elliptical) particle motion used in the polarization analysis (see Riviere-Barbier *et al.*, 1992). Therefore, station KIV was excluded from this experiment. The figure shows the following:

- The standard recipe S and the GAR recipes (G1, G2, G3) perform relatively poorly for azimuth estimation, especially at AAK and TLY. This indicates a sensitivity to the length of overlapping time windows used to make polarization measurements (see Table 3).
- The azimuth recipes (A1 at ARU and G1 at GAR) are not optimum, especially for GAR.
- At all stations, the minimum variance is obtained with a recipe including the 2-4 Hz band, and at AAK and GAR the best recipe includes the 4-8 Hz band.
- Except for the poorly performing GAR recipes, the variance does not significantly increase as higher frequencies are included.

Therefore, based on these results, an optimization scheme for both phase identification and azimuth estimation utilizing only one polarization recipe appears feasible.

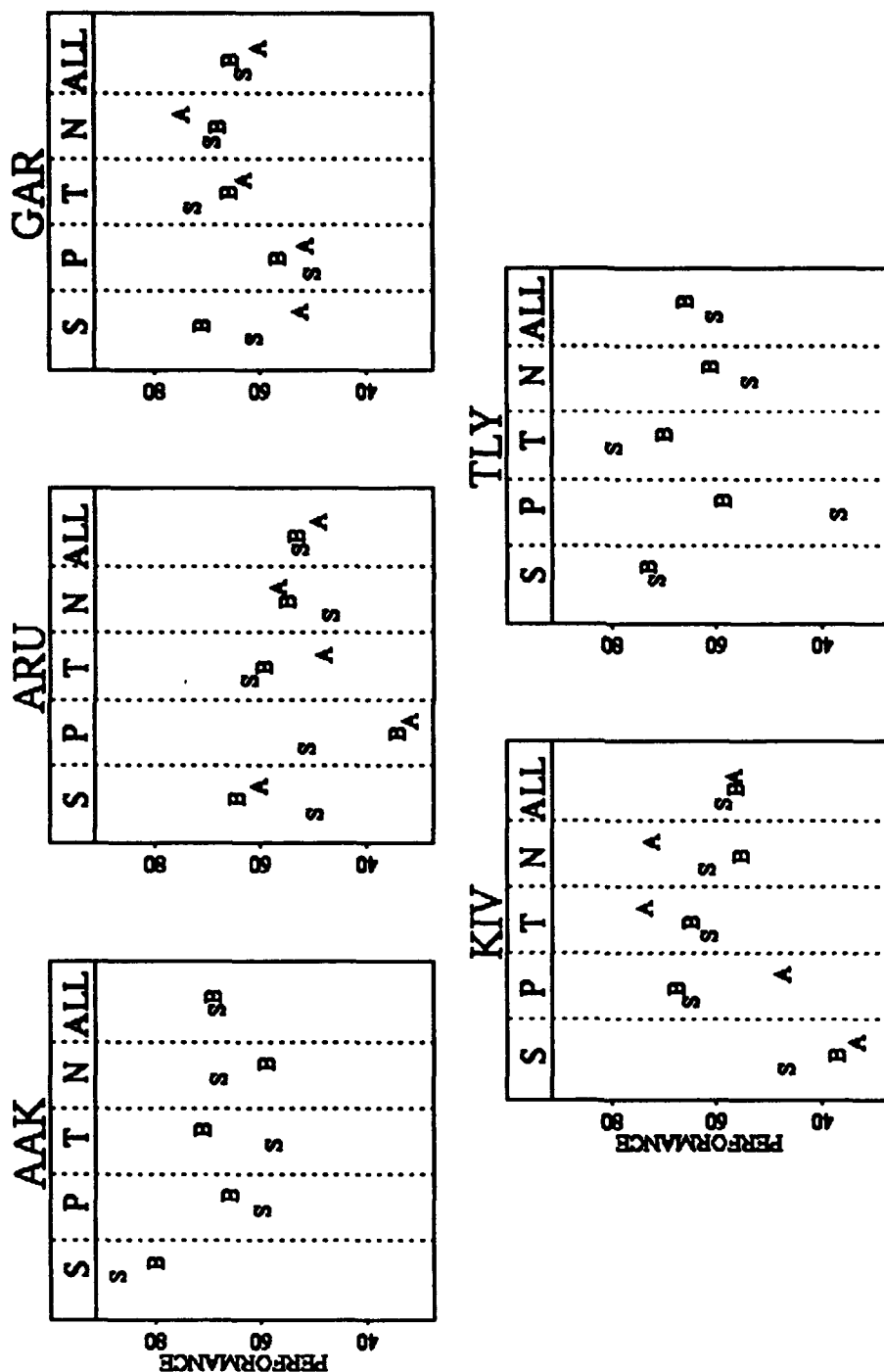


Figure 9: The phase identification performance (percentage of correctly identified detections) is displayed for each of the four groups (regional S, regional P, Teleseismic, and Noise), and their average, at each of five IMS/IRIS stations. The results are shown for the standard recipe "S", the optimum recipe "A" for azimuth estimation (from Riviere-Barbier et al., 1992) when it applies, and the best recipe "B" obtained for the S / P / T classification

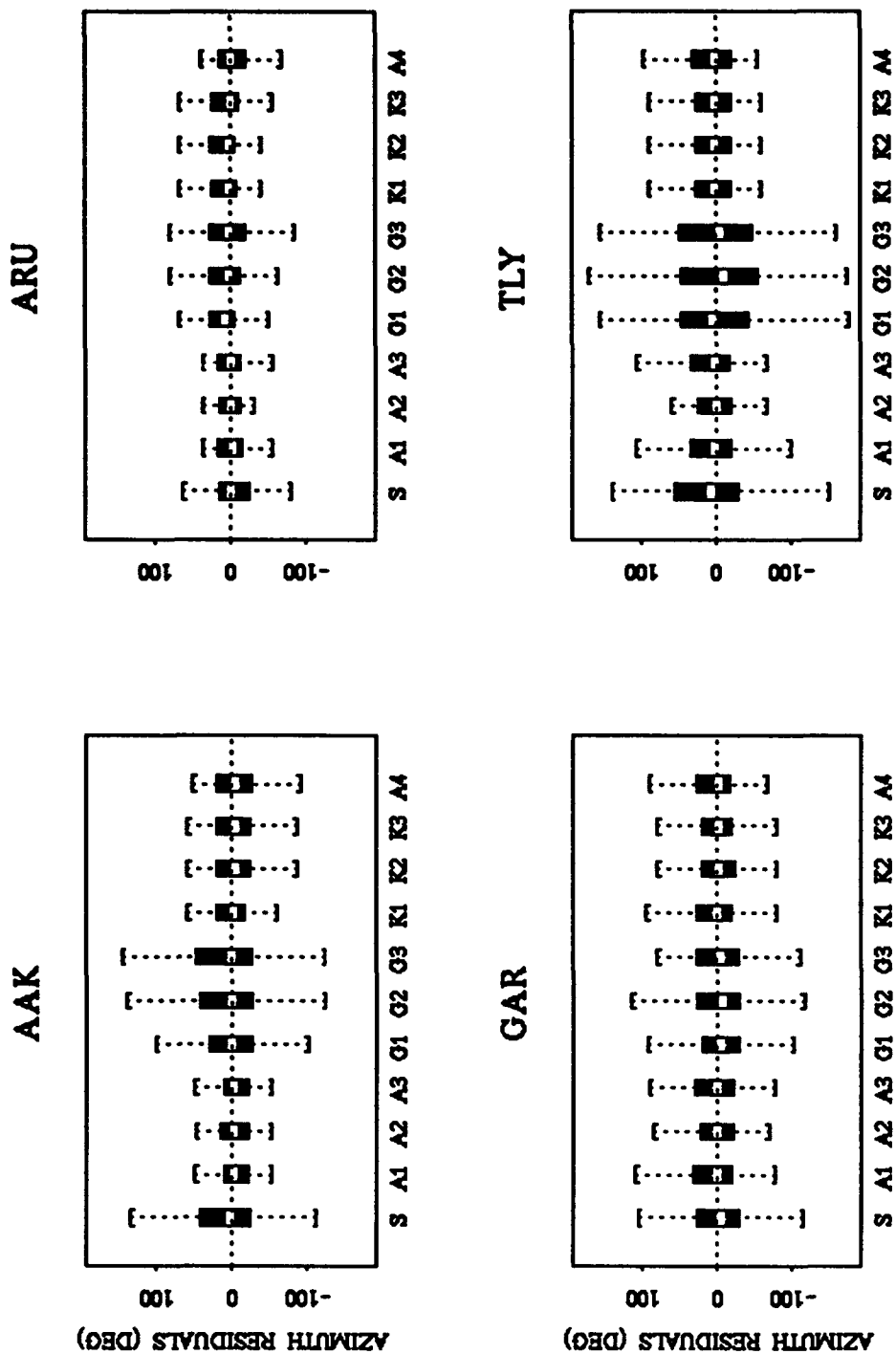


Figure 10: The distributions of azimuth residuals (azimuth from polarization minus azimuth from NEIC location) of teleseismic P arrivals are displayed for eleven polarization recipes (described in the text and Table 3), at each of four IMS/IRIS stations.

Combined Optimization

A weighted average was used to estimate the overall performance of various recipes for phase identification and azimuth estimation combined. At the 3-C IMS/IRIS stations, phase identification is more important than azimuth estimation, and therefore, was given a weight of 2. Also, as the correct identification of regional P is more crucial than that of other detections, it was assigned a weight of 1.75.

The statistics for azimuth estimation displayed in Figure 10 were converted to measures of performance (in percent), comparable to the classification performance for phase identification. This was achieved by subtracting the lower from the upper 95% confidence limits, and linearly transforming the result (x) to obtain an "azimuth estimation performance" y (using the formula: $y = 100 - 1.4 x$). The results of combining the performance for phase identification with that for azimuth estimation are displayed in Figure 11 for the set of eleven recipes, and for the S / P / T classification experiment described in the previous section. They can be summarized as follows:

- The GAR recipes (G1, G2, G3) and the standard recipe S (except at ARU) have a poor combined performance.
- ARU or KIV recipes with frequency ranging at least up to 4 Hz (i.e, A2, A3, K2, K3) perform best.

Finally, for each station, a subset of recipes was selected and tried on the data set including the coda and noise detections which is more realistic for phase identification in the IMS. This subset included the standard recipe S, the azimuth recipe (at stations where it applied), the best recipe from phase identification optimization alone, and any other promising recipe based on the results of the earlier test of combined optimization on a smaller data set (see Figure 11). Figure 12 shows the resulting combined performance. In summary,

- at AAK, GAR and TLY the best performance is obtained for wide-band recipes, including frequencies from 0.5 to 8 Hz;
- at ARU a better performance results from the use of a recipe that does not include the higher frequencies (the 4-8 Hz band).

Therefore, only at ARU does including azimuth estimation in the optimization significantly alter the results. This may be due to the small number of regional arrivals in the data set for that station, and a larger data set should be analyzed to reach definite conclusions.

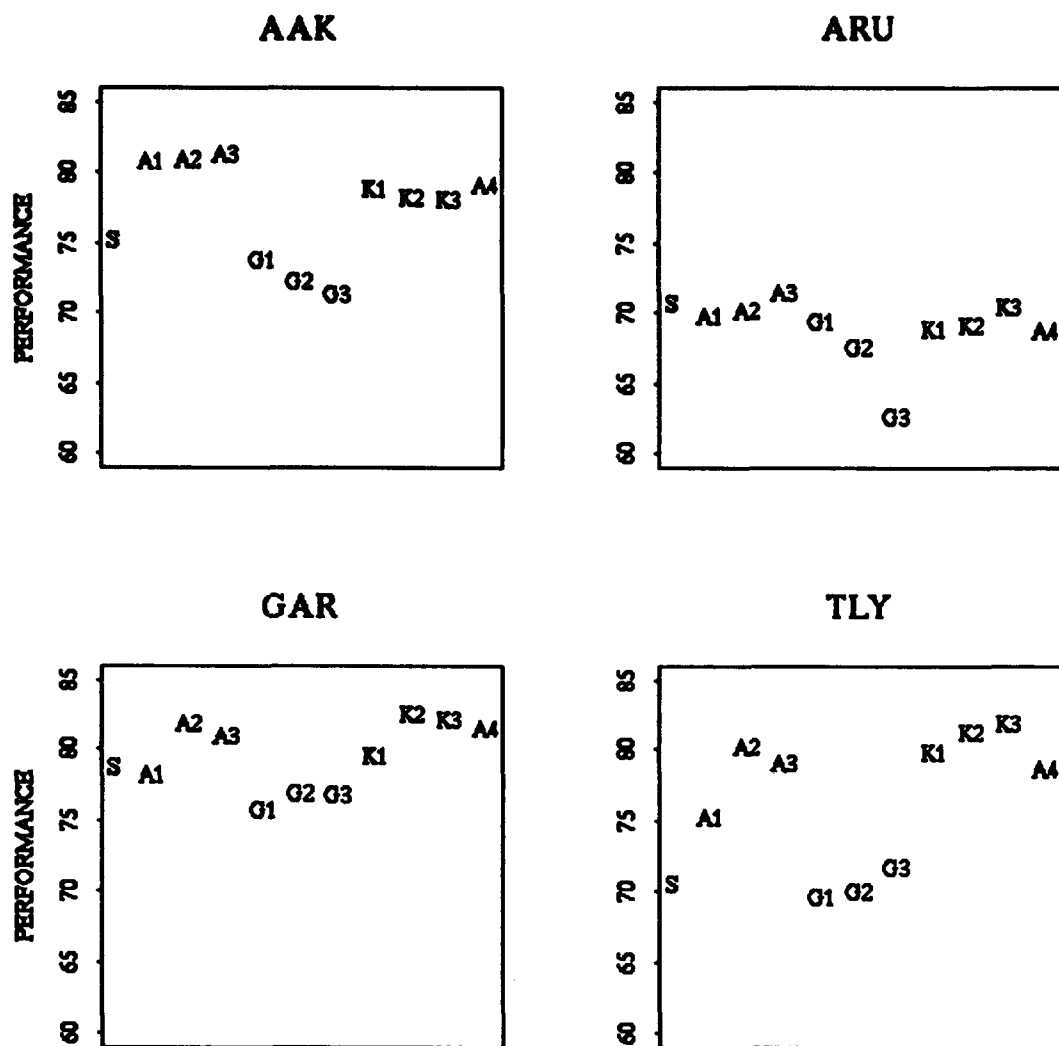


Figure 11: The combined performance for phase identification and azimuth estimation is displayed for a set of eleven polarization recipes (described in the text and Table 3), at four IMS/IRIS stations. The classification problem considered is the separation of regional S, regional P, and teleseismic detections.

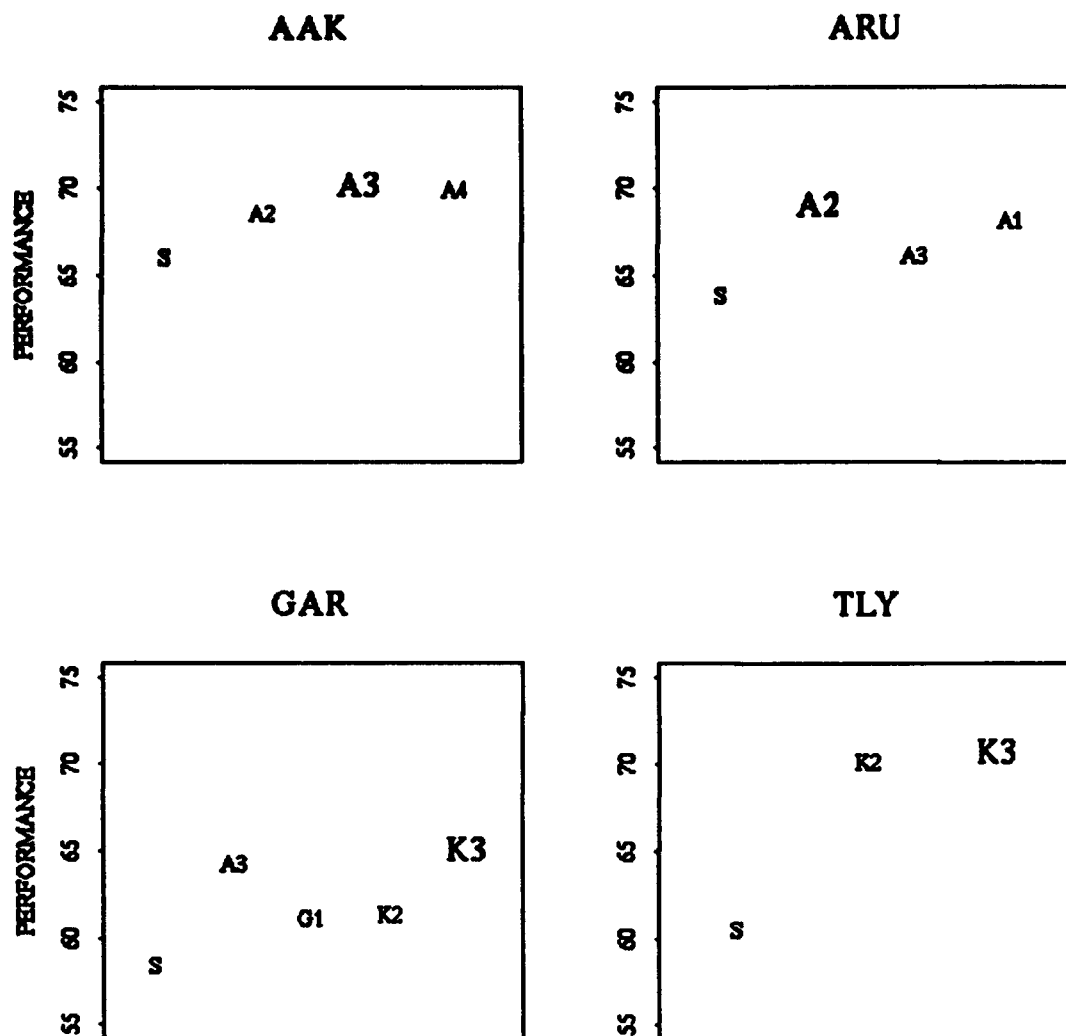


Figure 12: The combined performance for phase identification and azimuth estimation is displayed for four of the IMS/IRIS stations. The data set used for phase identification included all four detection groups (regional S, regional P, Teleseismic, and Noise). At each station, the performance was estimated for the standard recipe S, the optimum recipe for azimuth estimation from Riviere-Barbier et al. (1992), when it applied, and a selected subset of recipes that performed well for the S / P / T combined optimization experiment (see Figure 11). The resulting preferred recipes are highlighted.

Conclusions

Polarization analysis was optimized at IMS/IRIS 3-C stations to improve its usefulness in the IMS automated processing. The first test consisted of optimizing the recipe for initial phase identification alone. The frequency band used in the analysis was found to be the main processing parameter affecting the performance. The recipes previously found to optimize azimuth estimation (Riviere-Barbier *et al.*, 1992), as they do not include frequencies above 2 Hz, performed poorly, especially for the important identification of regional P detections. Including the 2-4 Hz band generally increased the performance. At TLY, adding the 4-8 Hz band (not part of the standard IMS recipe) resulted in further significant improvement.

Next, optimization of azimuth estimation was attempted at AAK, ARU, GAR, and TLY. This time, temporal parameters in the polarization recipe (such as length of overlapping time windows) affected the performance more than frequency band. The recipes that performed best included higher frequencies (at least the 2-4 Hz band) as for phase identification. These observations indicated that, at these stations at least, including higher frequencies in the recipe (which improves phase identification) did not significantly degrade the performance for azimuth estimation.

At AAK, GAR and TLY, combined optimization of phase identification and azimuth estimation was achieved with a wide-band recipe, including frequencies from 0.5 to 8 Hz, while at ARU, a recipe with a narrower band (up to 4 Hz only) gave better results. The standard IMS recipe performed poorly, mainly due to its inadequacy for azimuth estimation, which may be related to its lack of time resolution. No single recipe was found to be optimum for all stations considered. This is not surprising as the signal and noise characteristics are site-dependent. The fact that at a given station, one recipe could be found satisfactory for both phase identification and azimuth estimation is likely due to the fact that they both rely on optimum measurements of polarization. The polarization algorithm insures that only frequency bands with SNR above a given threshold contribute to the measurements, so that higher frequencies do not degrade azimuth estimation for teleseismic P, for example, as long as the SNR threshold is set high enough. Based on these results, it appears that careful parameterization of polarization analysis will make such a combined optimization feasible at other 3-C stations as well.

Acknowledgments

Ray Willemann performed the automated continuous data processing that resulted in the data set of detections used in this study. Flori Ryall performed the interactive analyst review that provided a reference phase identification for each detection.

References

- Bache, T. C., S. R. Bratt, J. Wang, R. M. Fung, C. Kobryn, and J. W. Given (1990). The Intelligent Monitoring System, *Bull. Seism. Soc. Am.* **80**, 1833-1851.
- Riviere-Barbier, F., A. Suteau-Henson, V. Z. Ryaboy, and J. A. Carter (1992). Analysis of Three-Component Data From IRIS/IDA Stations in the USSR, *Bull. Seism. Soc. Am.* **82**, 192-220.
- Suteau-Henson, A. (1991). Three-Component Analysis of Regional Phases at NORESS and ARCESS: Polarization and Phase Identification, *Bull. Seism. Soc. Am.* **81**, 2419-2440.

Stacking of Waveforms for Depth Estimation

Hans Israelsson

Introduction

In this note we define a procedure to stack waveforms recorded by a network of seismic stations for detection of depth phases, sP and pP. Procedures for stacking waveforms to enhance surface reflected phases have been developed and tested by Roy (1984), who identified depth phases from the maxima of stacked signal envelopes. In this note we aim at a procedure that *automatically* searches for a depth on the basis of surface reflected phases. Such a depth, hereafter called a 'candidate depth', is given as an interval over which possible depth phases are enhanced. The procedure only requires the epicenter of the event to be processed, and the first arrival times of the associated waveforms. It uses waveforms recorded in the teleseismic window, i.e., 30-90 degrees, as records obtained at shorter distances may be corrupted by the complexity of wave propagation in the regional distance range. The stacking procedure is applied to data from the world wide seismic station network of the GSETT-2. During this experiment, as described by Bratt (1992), waveforms recorded at a world wide network of seismological stations were collected and compiled from April 22 through June 2, 1991.

Data

For the analyses here we selected waveforms that could be associated with events reported by NEIS with a body wave magnitude, $mb(\text{NEIS}) > 4.0$, and that were based on observations at more than 10 stations. Furthermore, events with depths estimated by NEIS to be deeper than 200 km were omitted.

The waveform data were automatically retrieved from the GSETT-2 database at the Center for Seismic Studies. One or more waveforms in the teleseismic window were available for 488 events, the geographical distribution of which is shown in the map of Figure 13. Two of the events were underground nuclear explosions, both with locations in the South Pacific and marked with a cross in Figure 13. The magnitude of the events were between $mb=4.1$ and 6.4 and had depths estimated or constrained by NEIS between 5 and 196 km, apart from the two explosions. In all, 3,512 waveforms were processed. They were recorded at 40 stations, 30 single stations and 10 arrays with apertures varying from a few to a few tenths of km. The geographical distribution of the stations, which are indicated by the designated station codes in Figure 13, is highly non-uniform. In fact, almost 50% of the stations are concentrated to Europe over an area less than about 10% of the earth's surface. The distributions of waveforms over events and over stations were also

GSETT-2 : EVENTS AND STATIONS

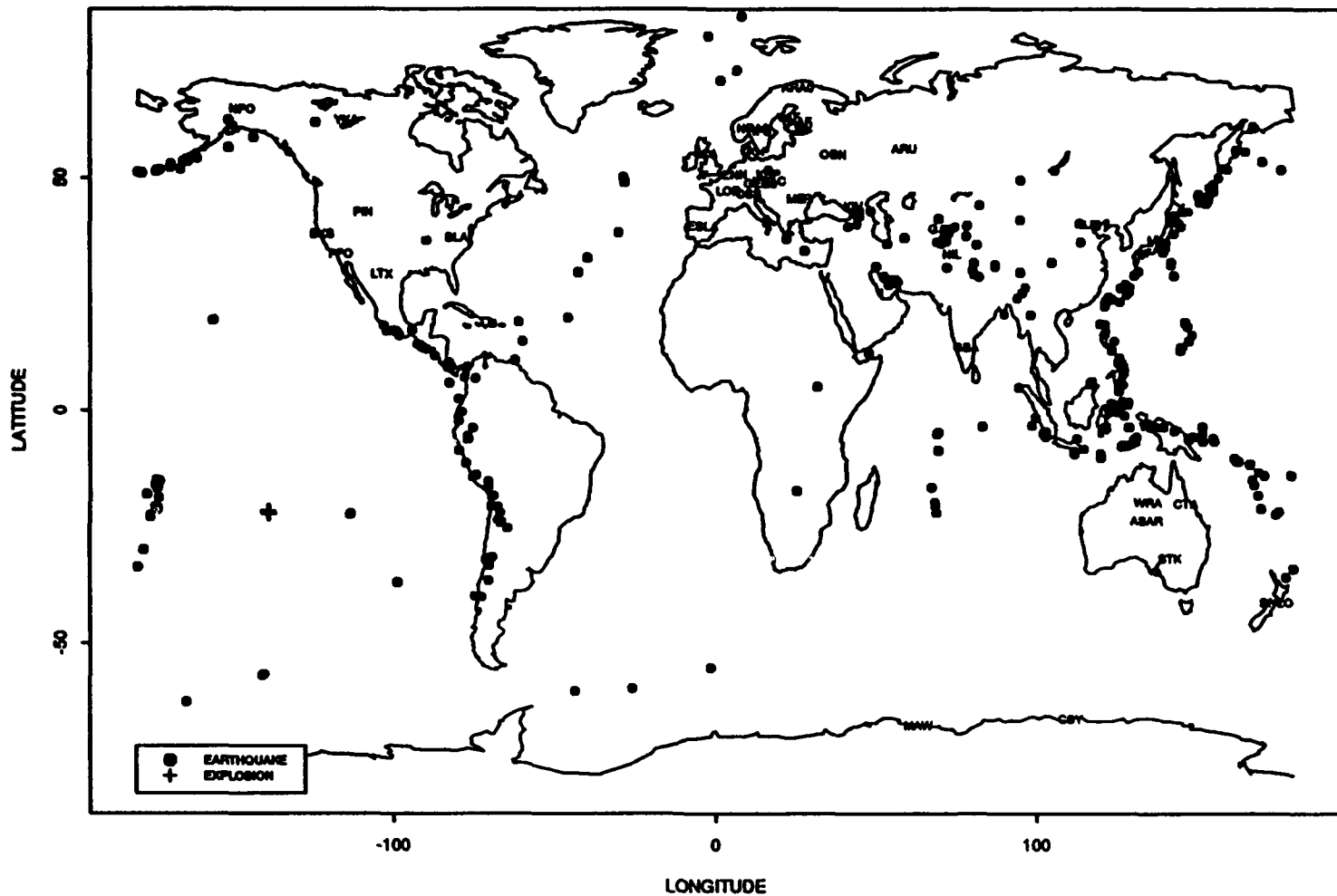


Figure 13: The map shows the geographical distribution of the events and the seismic stations for which waveform data were analyzed. The two underground nuclear explosions in the South Pacific are marked with crosses.

uneven. The number of waveforms per event varied between 1 and 34 with a median of 6, and the number of waveforms per station varied between 2 and 280 with a median of 78. Only vertical component recordings were used in the processing and analysis, and for array stations phased beams were used to the largest extent possible.

Depth Traces

Before stacking waveforms associated with a given event, each waveform was processed in several steps in order to increase the signal-to-noise ratio, compensate for differences in delay or move out of the depth phases, and to minimize the possibility of mistaking a PcP phase for a depth phase. Furthermore, each waveform was transformed into a binary trace with a STA/LTA detector to enhance possible secondary depth phases and to avoid destructive interference in the stacking procedure from large coda levels at stations with no depth phases. The steps of the signal processing are illustrated in Figure 14.

Frequency filtering

It has been observed that depth phases from earthquakes at depths below 200 km appear to have less high frequency than the direct P because their paths traverse the structure above the focus of an earthquake twice and are subject to more significant attenuation. (Blandford, private communication) To examine similar effects for earthquakes at shallower depths, Figure 15 shows the ratio of the periods of pP/P and sP/P for phases that were positively identified during the GSETT-2. The ratios are plotted as a function of the delay time, i.e. arrival times of pP - P and sP-P respectively. The ratios have a large scatter and there is no consistent difference in the periods of pP and sP on one hand and of direct P on the other. However, the smoothed trends obtained by robust regression (Cleveland, 1979) suggest that the pP and sP appear to have slightly more low frequency than does direct P.

In order to maintain as broad a frequency range as possible and to allow for differences in noise and receiver responses among the stations, the limits of the band pass filter (3 pole phase free Butterworth) were based on spectral analysis of noise prior to the onset of the initial P.

Binary trace

Stacking aimed at enhancing depth phases that are based on bandpass filtered waveforms or waveform envelopes may suffer from destructive interference from waveforms with high coda levels and with no clearly developed surface reflected phase. Therefore we applied a STA/LTA detector, with windows of 1 and 5 s length respectively, to the

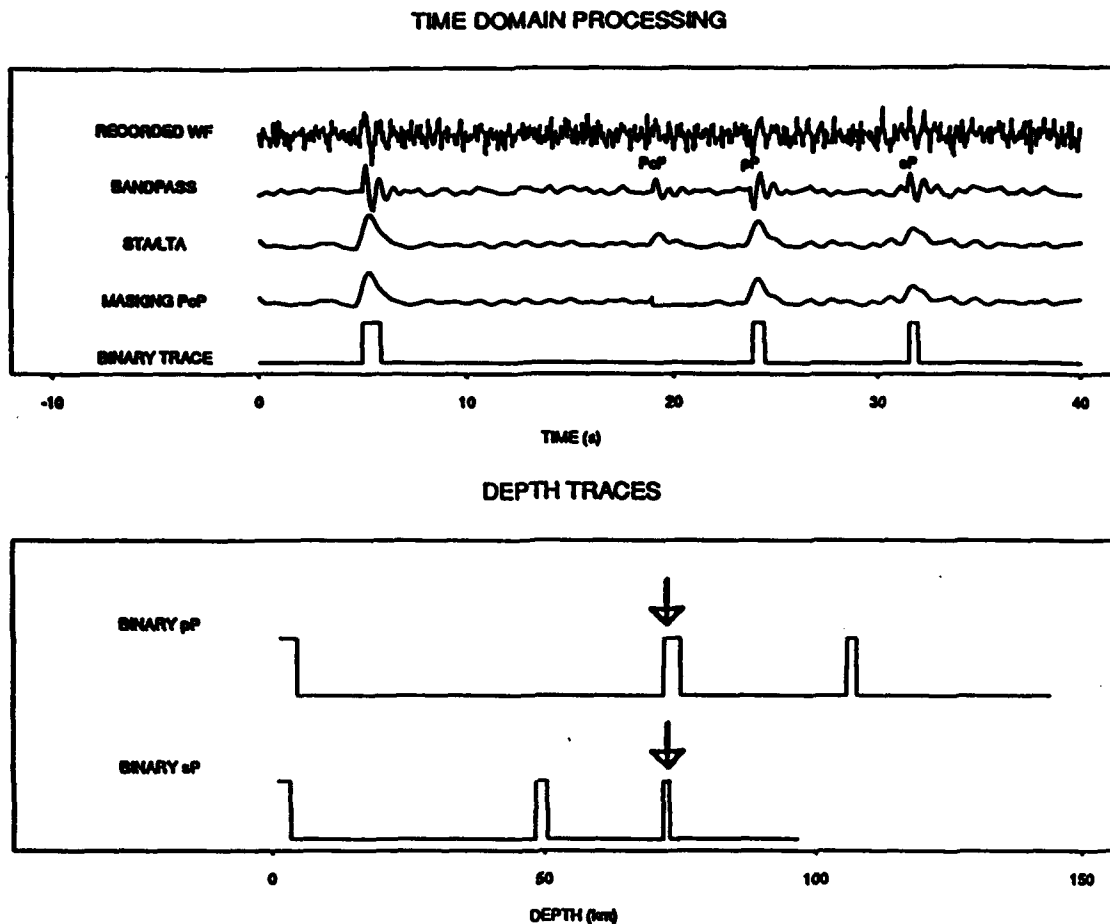


Figure 14: The signal processing and transformation in the time domain, upper frame, and in the depth domain, lower frame. The time domain processing involves bandpass filtering to enhance the signal-to-noise ratio, forming of a STA/LTA trace, masking of window for expected arrival time of PcP, and transformation into a binary trace. The binary trace in the time domain is mapped into two binary traces in the depth domain, one each for pP and sP.

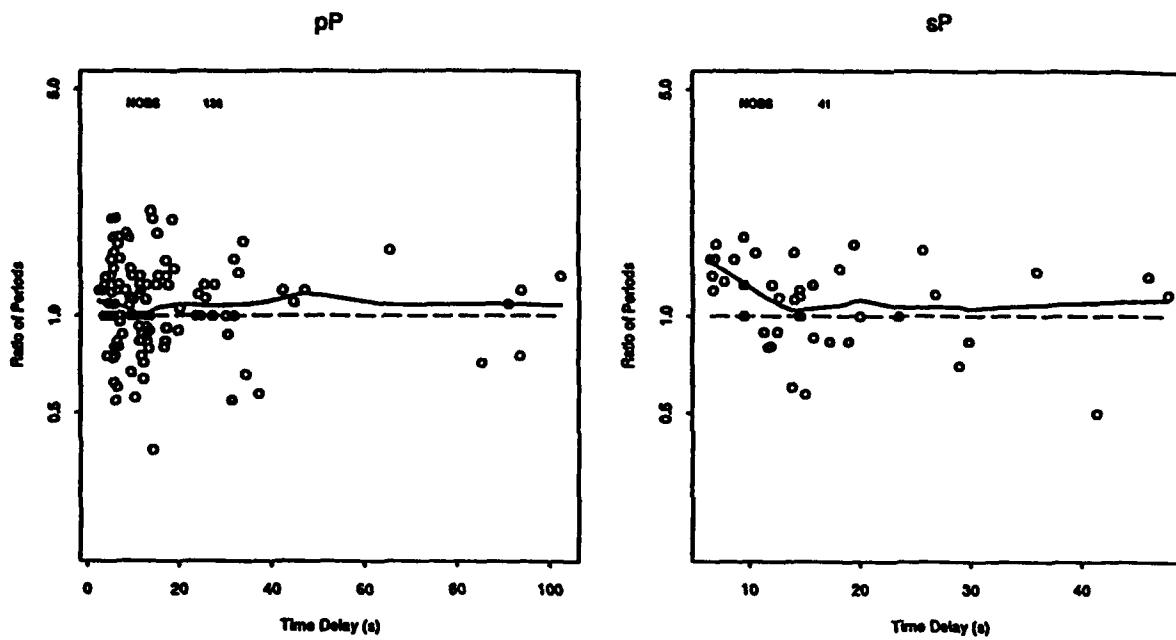


Figure 15: The scatter diagrams shows the ratios of the periods of pP/P , to the left, and of sP/P to the right, as a function of the delay times.

waveforms. This STA/LTA trace is then converted into a binary trace, which is 0 or 1 if the STA/LTA ratio is less than or greater than a threshold of 1.75, respectively. In Figure 16 we have compiled all the STA/LTA traces into a record section as a function of epicentral distance. The part of the traces with STA/LTA greater than the threshold are indicated as black dots. The expected arrival time of PcP for depths between 0 and 200 km is indicated. No clear clustering of detected phases appears along the lines indicated for the expected PcP, and the section gives a general impression of randomness with no other significant features. The generally white area 5-10 s following the direct P, may be partly due to the saturation of the STA/LTA ratio caused by the primary phase which usually has the largest amplitudes.

Masking of PcP window

Even if the PcP phase does not stand out as a striking feature on the record section in Figure 16, we mask, or zero the binary trace for a 2 s window centered at the expected arrival time of PcP. This avoids mis-identifying PcP phases as depth phases in cases where PcP is clearly developed.

Transformation into depth traces

Before binary traces calculated from waveforms recorded at different distance ranges could be stacked together we made a transformation from the time domain to the depth domain. This compensated for possible differences in delay or move-out of the depth phases relative to the direct P for different epicentral distances. The move-out also strongly depends on the depth of the event. For example, pP move-out is about 1 and 9 s between 30 and 90 degrees for earthquakes at 50 and 200 km depth, respectively.

Each binary trace was thus mapped into two depth traces one for the pP and one for sP. A depth trace for pP, for example, is obtained by converting the delay time from the onset of direct P into the corresponding depth using a travel time table. For this study we used the JB travel time tables. As the synthetic example in Figure 14 illustrates for a case with clearly developed pP and sP phases, the binary depth traces for pP and sP will have signals that line up at the same depth, around 70 km in this example.

Stacking of Binary Traces and Candidate Depths

After calculating the binary traces, they were combined into stacks for pP and sP by straight summation. Only binary traces corresponding to waveforms with signal-to-noise ratios larger than 3.0 were used in the stacking. Selected examples of binary and stacked traces together with the recorded waveforms are shown in Figure 17 a-c for three

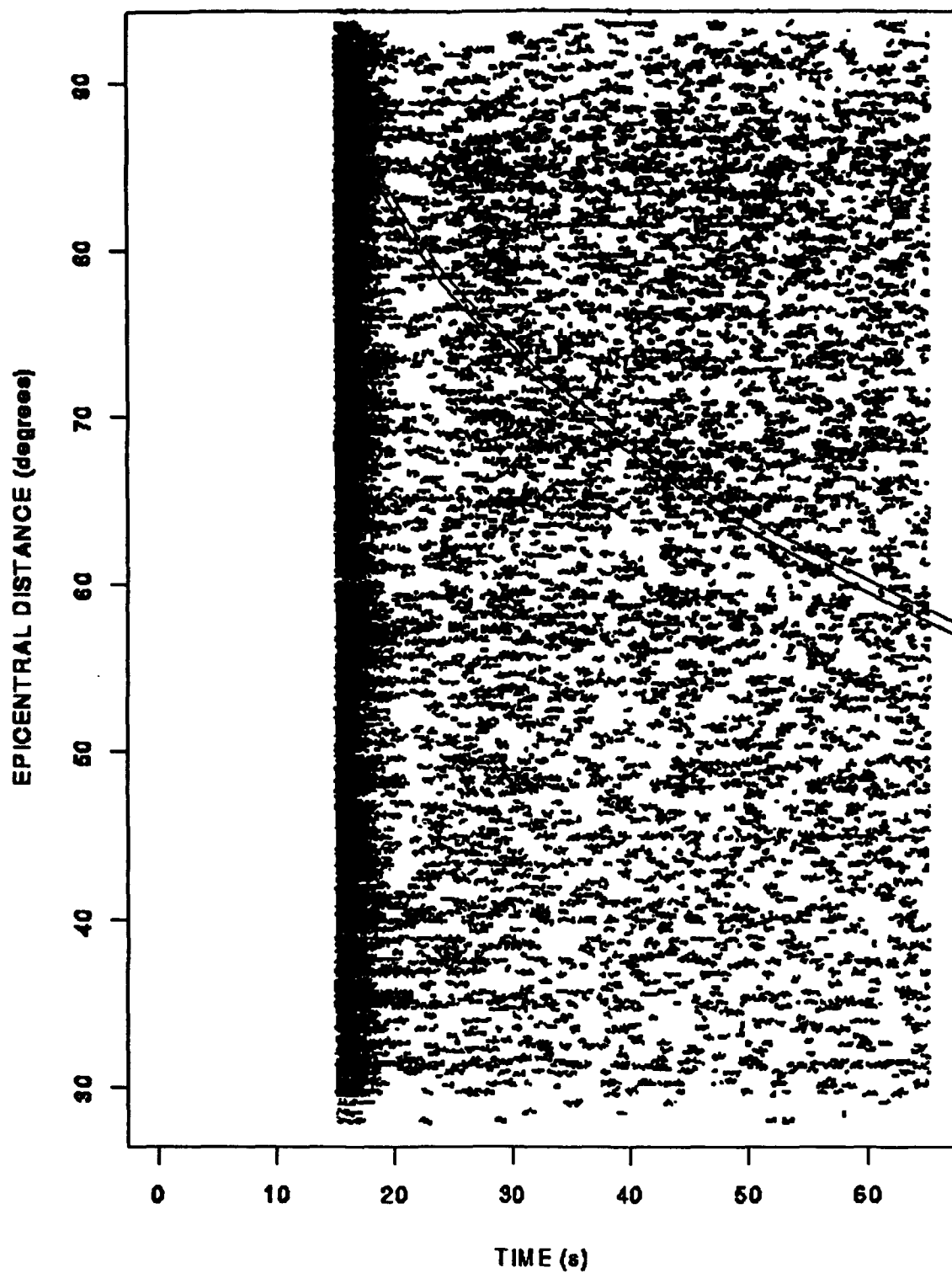


Figure 16: STA/LTA traces plotted as a function of epicentral distance for all the waveforms. Only the parts of the traces with the STA/LTA above the threshold, 1.75, were marked as black dots.

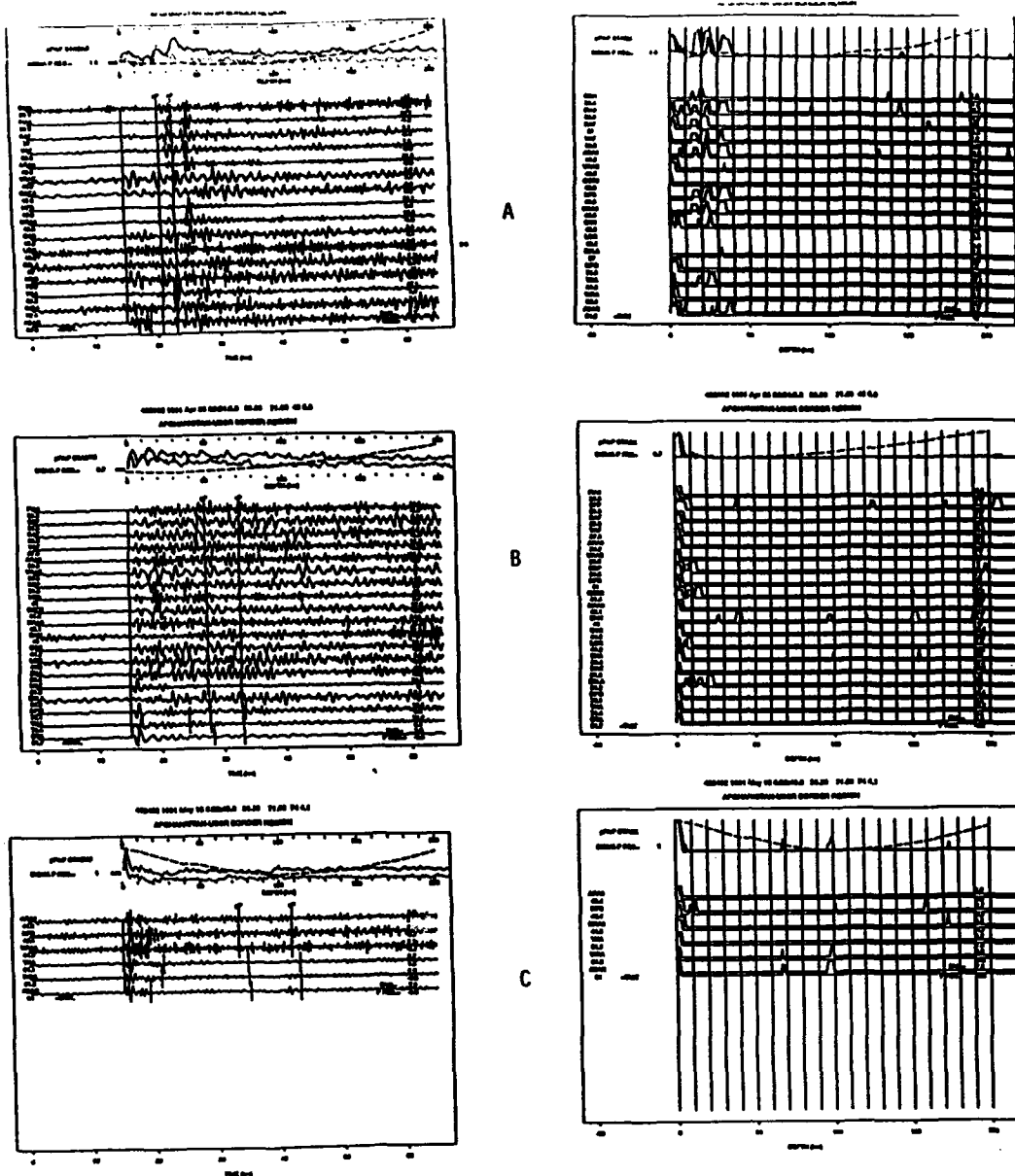


Figure 17: The figure shows waveforms and binary traces sections for three events in the Afghanistan-USSR border region on : (a) 91/05/13 at 23:55:33.7, (b) 91/04/26 at 22:24:05.3, and (c) 91/05/13 08:32:43.8. Station codes and epicentral distances are indicated to the right of each waveform. The waveform sections also include, at the top, envelope stacks of pP and sP as a function of depth and the standard deviation of the first arrival time P residuals as a function of depth (SIGMA P RES in the diagrams). The signal-to-noise ratio, SNR, and the P residual for the NEIS hypocenter solution are shown to the right for each waveform.

earthquakes near the Afghanistan-USSR border region. The three figures have the same format and each one includes one section with the recorded waveforms (bandpass filtered) and one section with the binary traces. In Figure 17a for the event on May 13 at 23:55:33.7, clear depth phases can be seen on many of the filtered traces. The signal-to-noise ratio and arrival time residual(s) are indicated at the end of each trace. As waveforms with SNR less than 3 were not used in the stacking, the stacked traces are based on a total of 10 traces, 6 of which are in Fennoscandia, all with quite similar appearance. Above these traces are also stacks of the envelopes of the waveforms transformed to a depth scale (also indicated at the top). There is one stack, respectively, for pP (thick heavy line) and sP (thick shaded line). The two stacks have two clear secondary peaks that line up at a depth of about 25 km. The binary trace section of Figure 17a also shows clear detections of the depth phases on the individual station traces as well as on the binary stacks at the top of the section. In the binary trace section, the horizontal scale for all traces is depth. Figure 17b is almost the opposite of Figure 17a with regard to observability and detectability of depth phases. Although this is a somewhat larger event with more waveforms that generally also have larger SNR, any clearly identifiable depth phases that appear on most of the traces can not be identified. 13 of the 17 traces with sufficient SNR recorded at European stations and they all have similar features. Possible depth phases can only be seen at three stations (HFS, GEC2 and KSP). The stacked envelope shows a maximum at about 10 km depth for pP, but there is no peak on the sP stack that lines up with this maximum. On the binary trace section few secondary phases were picked by the STA/LTA detector and although they line up to show a secondary maximum on the stack, the width of the initial phase is too wide to clearly separate it. Finally, the example in Figure 17c is the most typical of the data analyzed here with regard to the number of available waveforms. Secondary phases can be noted on at least two of the five filtered records and they add up constructively to show a maximum in the depth envelope stack corresponding to a depth of about 100 km from pP. However, this maximum is somewhat ambiguous as there is a maximum around 45 km as well. The stacking on the binary section separates clearly between these two possibilities. Only the depth around 100 km is now apparent. Clearly this is not sufficient to positively estimate the depth. As the example in Figure 17c is the most representative of a typical event analyzed in this study, we use the stacked binary depth trace to identify 'candidate' depth intervals as described in the following, rather than attempting to assign an exact depth to each event.

Such candidate depths were defined from the stacked binary traces with clearly defined signals (see Figure 18). For the purpose of the analysis here, we used the following automatic procedure. A given stacked depth trace, for pP or sP, was searched for a unique signal maximum after the signal corresponding to the initial P had come to zero. That is to say, an uninterrupted depth range with a maximum larger than any other value of

the depth trace, except for the initial P. The depths corresponding to the beginning and end of the interval in which the maximum occurred define a depth interval for the trace. As the pP often is recorded more clearly than sP phases, the candidate depths from the sP trace is just a non-linear translation of the depth of pP trace.

Applicability

In order to get some idea of the performance of the stacking procedure in defining 'candidate' depths, we examined the events for which depths could and could not be obtained without any consideration of the quality of the obtained candidate depths themselves. The applicability may be determined by several factors, such as the actual depth of the event, the number of available waveforms, and the distribution of the stations around the source azimuth. Furthermore, there may be significant regional effects. It has, for example, been suggested that scattering and defocusing of P and S by lateral variations in the crust and upper mantle above the focus may cause significant reduction in the amplitude of surface reflections. The distribution of the events and waveform data used in this study was not sufficient to study these factors in isolation or to apply additive models that would separate the effects of various factors. Therefore, we look at each factor separately.

Figure 18a shows the distribution of depth, as determined by NEIS, for the events for which 'candidate depths' could and could not be defined. Figure 18b shows the percentage of events with candidate depths as a function of depth. The data in these two figures are limited to events for which depth was determined from three or more waveforms. We note that most of the NEIS depths were constrained to either 10 or 33 km (Figure 18a) and that a significant portion of the events that are constrained had 'candidate' depths. The data in Figure 18b does not suggest any clear effect of focal depth, although one might have expected that the chances of defining a 'candidate' depth would increase with increasing depth.

Figures 19a-b show the geographical distribution of the events with and without 'candidate' depth marked with plus signs and open circles, respectively. For continental events in Eurasia, a regional pattern is evident. For example, many events in the Hindu Kush area and around the Indonesian archipelago have candidate depths, whereas few events in Southern Iran have candidate depths. Candidate depths were not obtained for the two underground nuclear explosions in the South Pacific.

In Figure 20 we show the success and failure rates as functions of the number of waveforms and azimuthal coverage. Azimuthal coverage is defined as the number of 45 degree angular sectors around the source to station azimuth for which there is one or more stations. Before counting the number of sectors, they were centered at the median azimuth

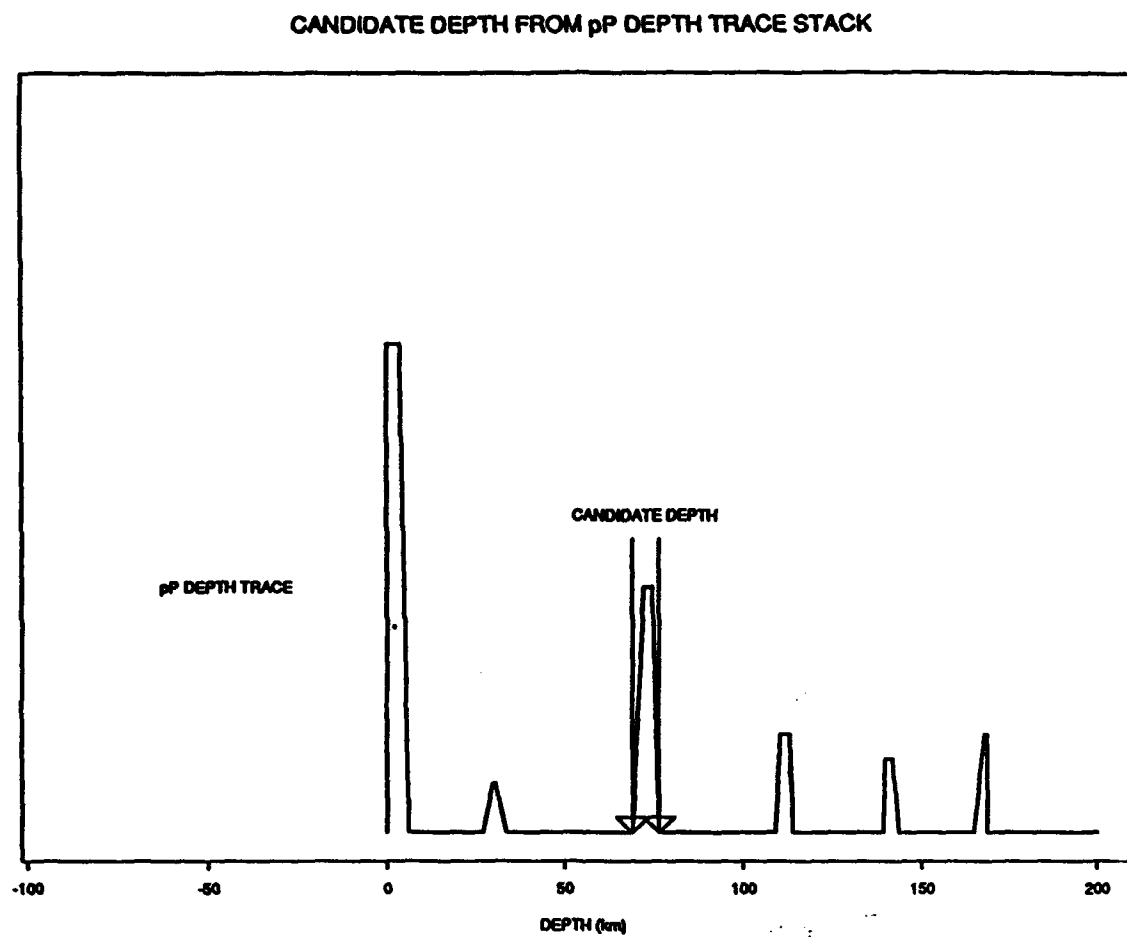


Figure 18: (a) The figure shows how the candidate depth is defined from a pP depth trace stack.

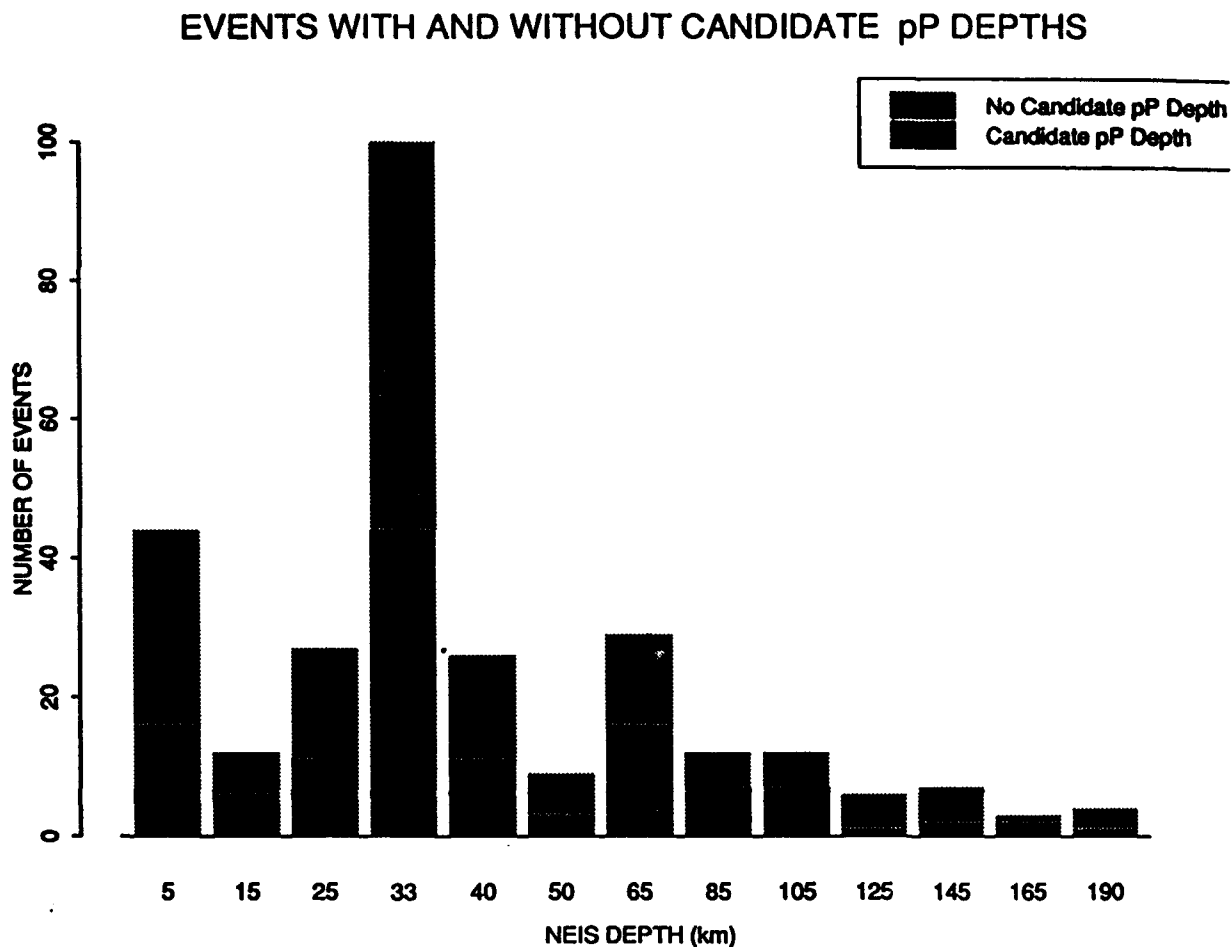


Figure 18: (b) The barplot shows the number of events with and without candidate depth as a function of depths reported by NEIS. Most of the NEIS depths were constrained to 33 km and a significant portion of those had candidate depths.

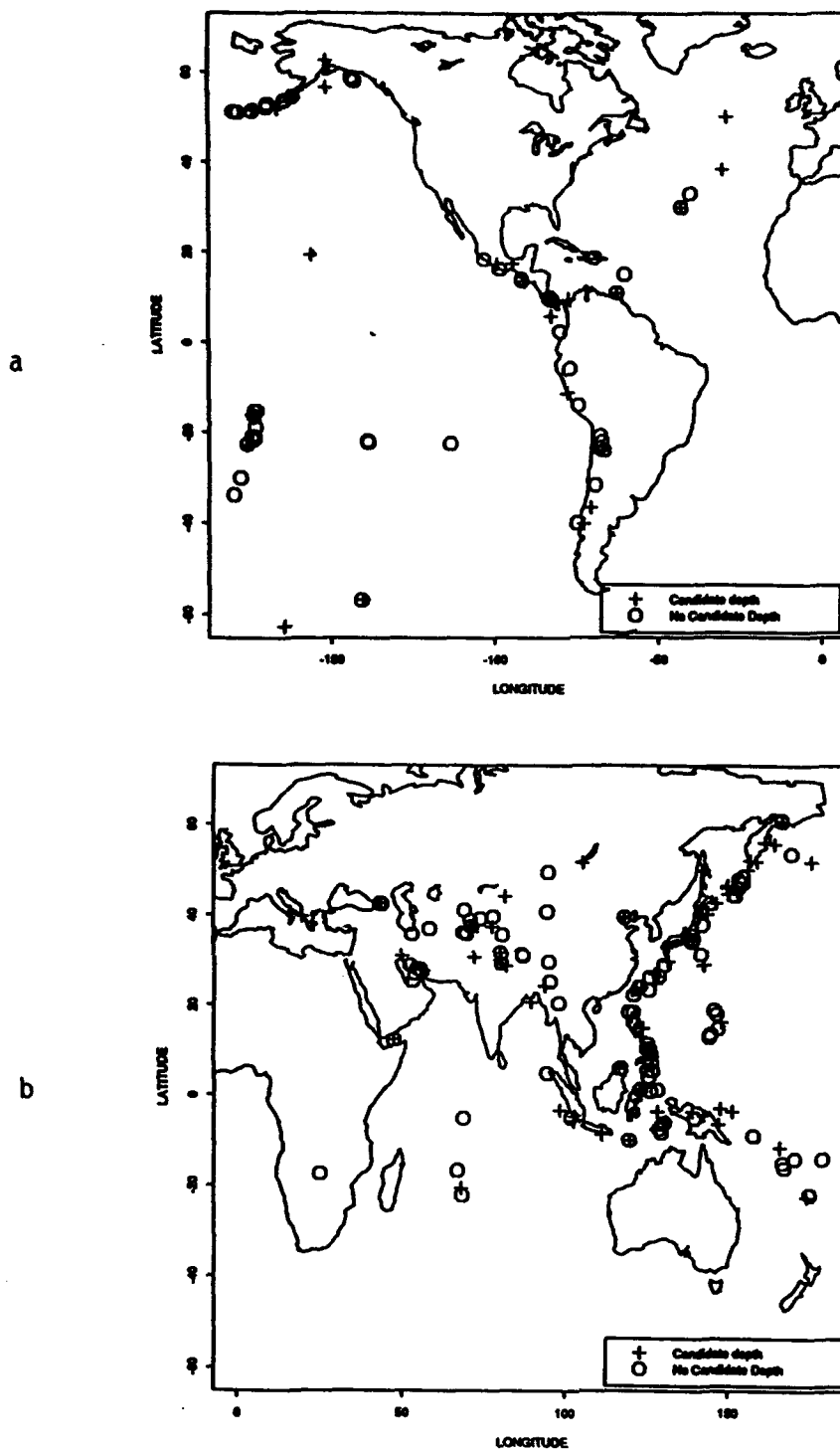


Figure 19: The geographical distribution in the Western (a) and Eastern (b) hemispheres of events with and without candidate depths.

of the stations. This means that cases where all stations are clustered within 45 degrees will be counted as one 45 degree sector, whereas an arbitrary reference of the azimuth sector might have yielded two 45 degree sectors. As in Figure 20 plus signs and open circles mark cases where a candidate depth could and could not be obtained respectively. The success rates, defined as the percent of events for which 'candidate' depths were defined are given vertically and horizontally as a function of the number of 45 degree sectors covered and number of waveforms available, respectively. With four or more sectors the success rate is about or above 50% and 9 or more waveforms are required to consistently achieve this rate. We note from the plus signs and open circles that there is a significant number of events for which the number of waveforms is smaller than 9 but the number of 45 degree sectors covered is larger than 4 for which candidate depths were obtained.

Comparison of Candidate and NEIS Depths

The quality of the derived 'candidate' depths are difficult to assess due to the obvious lack of ground truth in many instances. In Figure 21 we compare the NEIS depths and depths taken as the average of the lower and upper limits of the candidate depths. Comparisons are made as a function of the number of phases in the stacked trace, 1, 2, 3 and more than 3. The number of events for each case is indicated in the diagrams. Somewhat arbitrarily, we accepted a difference of 20 km between the two types of depths for agreement ("agree." in the diagrams). This large acceptance difference was partly based on the fact that a large percentage of the NEIS depths were constrained to 10 or 33 km. The comparisons in Figure 21 show reasonable agreement for 3 or more phases, although there are 4 events, 2 at 10 and 2 deeper than 100 km by NEIS, for which there is a clear discrepancy between the 'candidate' and the NEIS depths. The agreement rates are, as one would expect, smaller for stacks based on 1 and 2 phases only.

Earthquake Source Radiation Pattern and Depth Phases

As has been noted by Douglas et al. (1990), theoretical modelling of seismograms from double couple sources radiating pulses of around 1 s duration show that the most prominent arrivals on short period seismograms should be the direct P, pP, and sP. Indeed, Pearce (1980) developed a method to constrain the focal mechanism from relative amplitudes of P, pP and sP. However, the observations in the past of the character of P seismograms show that this model is frequently contradicted.

Moment tensors have been determined by HVD for many of the earthquakes analyzed here for which waveform data were available at two or more stations. These moment tensor solutions, which are obtained from long period data, were used to calculate 'theoretical' amplitude ratios for pP/P and sP/P. Algorithms for the radiation from moment ten-

EFFECT OF AZIMUTHAL COVERAGE

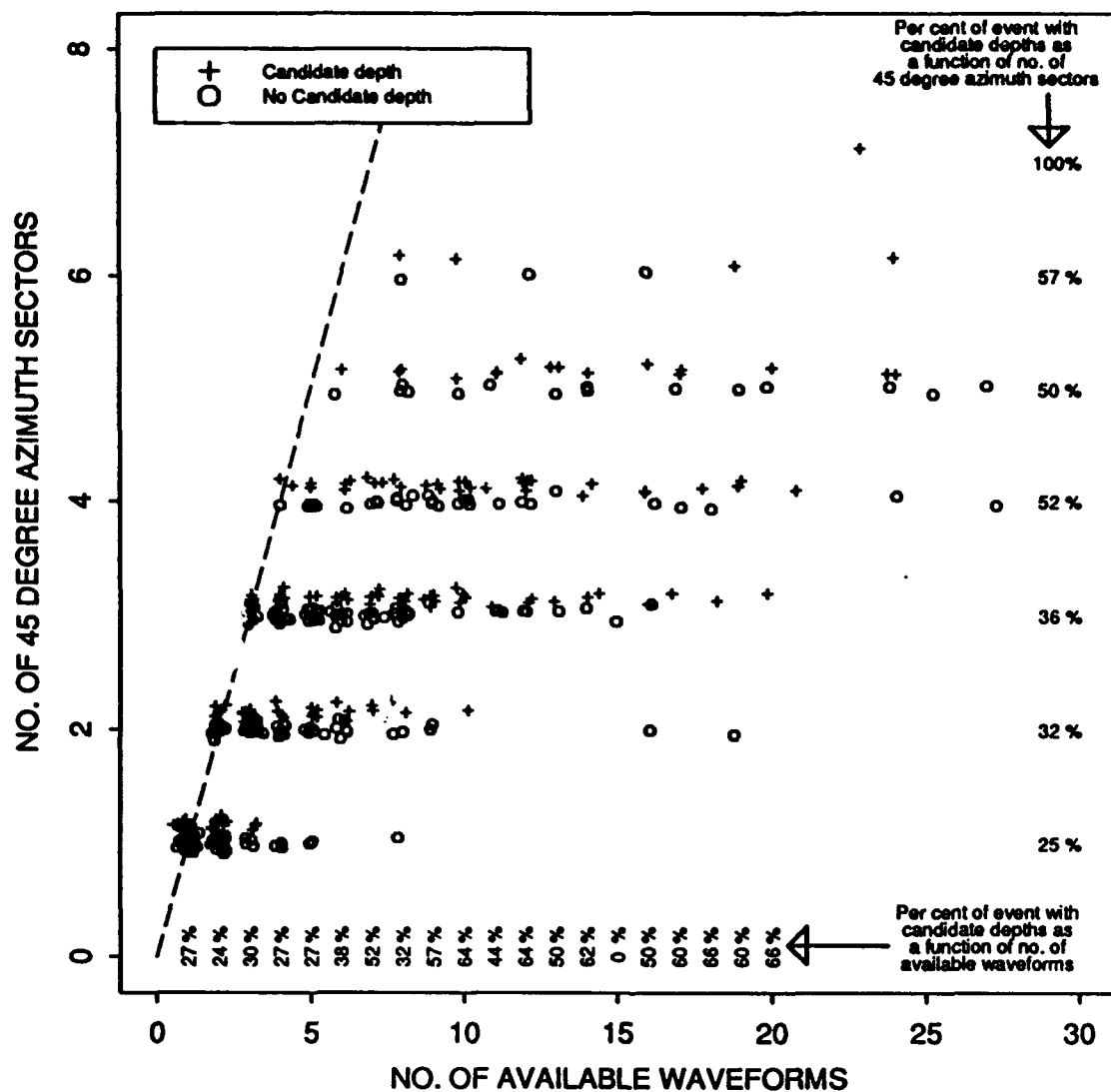


Figure 20: Success rates, given as percentages, to define candidate depths as a function of the number of waveforms and azimuthal coverage. Azimuthal coverage is given as the number of 45 degree sectors around the source to station azimuth for which there is one or more station with waveform data.

sors by Kennett (1988) together with the procedure to calculate the reflection coefficients of surface reflected phases defined by Pearce (1980) were employed for this purpose. The theoretical ratios were compared with those obtained from the waveform data. The 'observed' ratios were all calculated for a frequency band 0.8-2.0 Hz. In the calculations we used the depths reported by NEIS and omitted events with constrained depths, i.e. depths of 10 or 33 km.

In Figure 22 we show the correlation coefficient of calculated and observed ratios plotted as a function of the difference in pP delay time and the source duration as reported. Source duration was subtracted from the pP delay because there may be interference between direct P and pP for events at very shallow focal depth and with long source durations. We show the correlation coefficient of pP and sP ratios separately and also the geometric mean of these two correlation coefficients. Only events for which five or more waveforms were available are included in the comparison. High mean correlation coefficients were observed for only 2 out of 36 events. Figure 23 shows the actual observed and calculated ratios for one of the events, on April 26 at 17:36:59.4, 7.4 N 127.7 E and 74 km depth. It should be noted that 14 of the events occurred at such a depth and had such duration that interference between P and pP is likely. The poor correlation between the observed and calculated ratios could be due to several factors, but the results illustrate the unpredictability of depth phases from simple models of radiation patterns.

Concluding Remarks

In this note we have defined an *automatic* procedure of waveform stacking for estimating focal depth of a seismic event. As input it requires the epicenter and a preliminary estimate of the focal depth together with recorded waveforms and first arrival times. The procedure provides a 'candidate depth', defined as an interval over which stacked binary traces have a maximum value. The procedure should be seen as a tool assisting analysts working with global network waveform data in their effort to determine focal depths by presenting possible depth solutions.

The stacking procedure was tested on waveform data for 488 events collected during the GSETT-2. The capability to define a candidate depth depends on several factors and a large azimuthal coverage of recording stations is identified as one such factor of importance. A candidate depth could be defined for about 50% of the events for which the azimuthal coverage was 180 degrees or more.

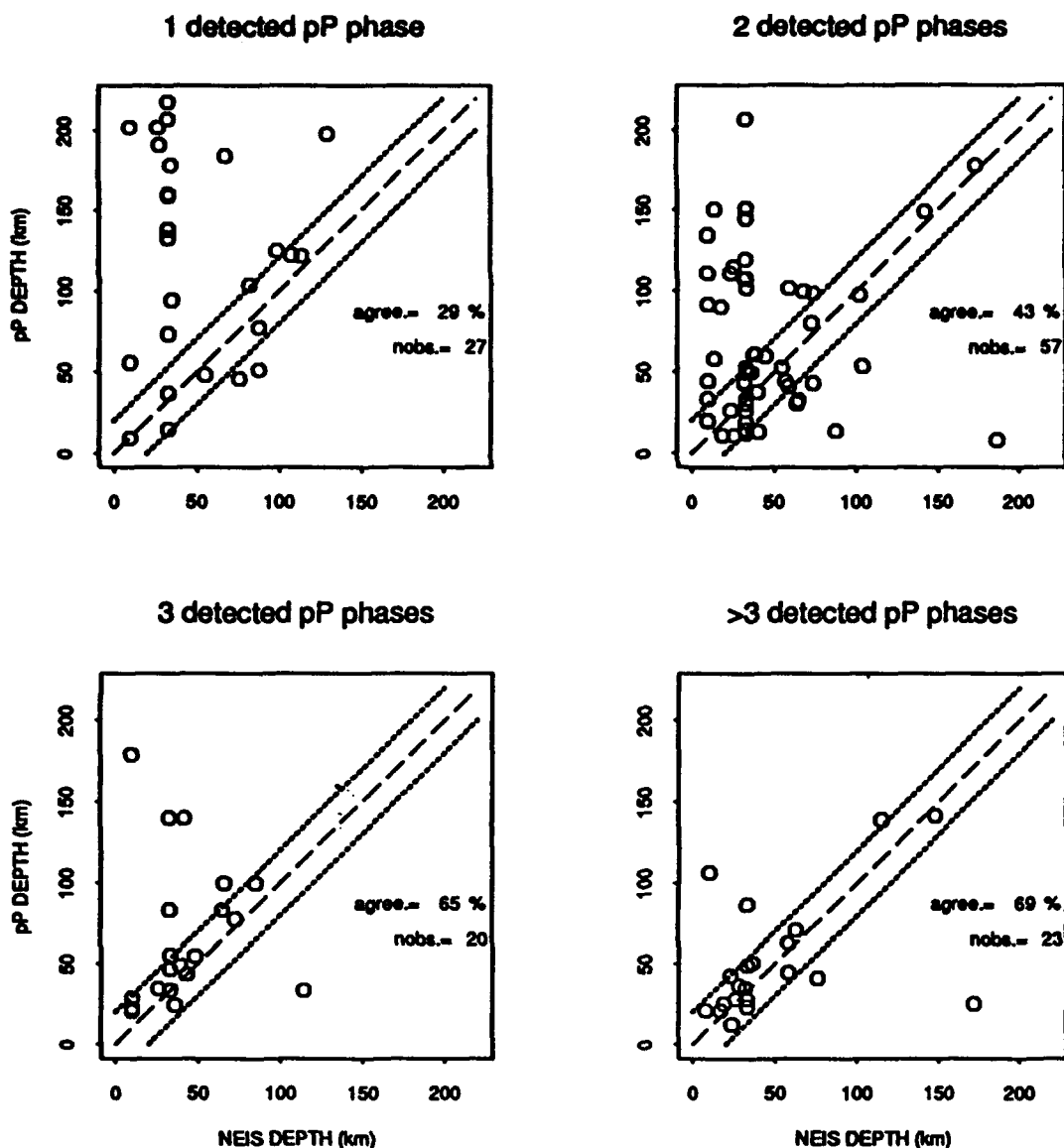


Figure 21: Depths taken as the average of the lower and upper values of the candidate depths ('pP DEPTHS' in the diagrams) compared with NEIS depths. Comparisons are made as a function of the number of phases in the stacked trace, 1, 2, 3, and more than 3. Somewhat arbitrarily, a difference of 20 km between the two types of depth is accepted for agreement ('agree.' given as percentages in the diagrams).

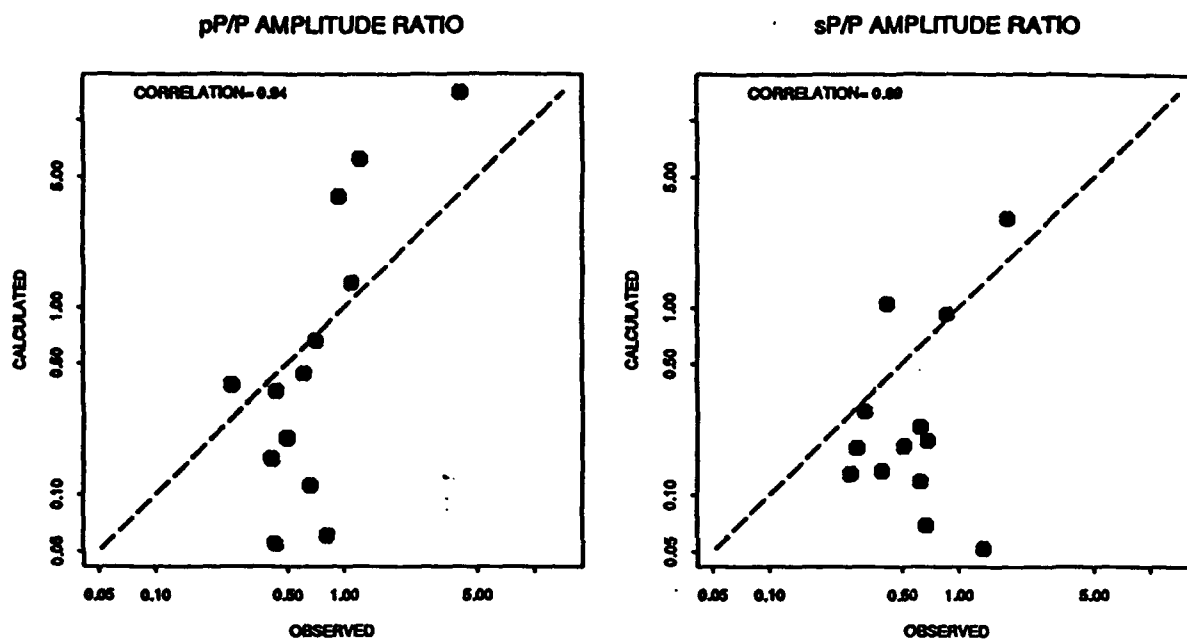


Figure 22: Comparison of theoretical and observed amplitude ratios pP/P and sP/P for the event on 91/04/26 17:36:59 with latitude 7.40 N and longitude 126.71 E and mb(NEIS)=5.5.

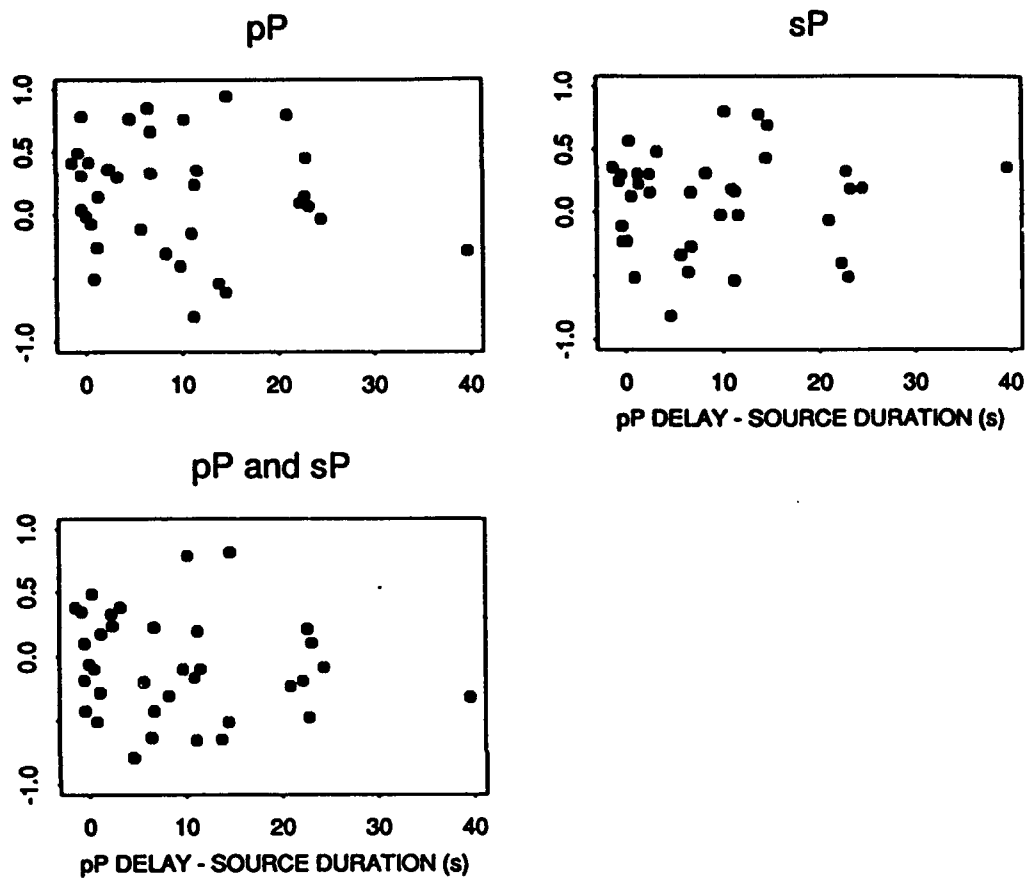


Figure 23: Correlation coefficients for observed and theoretical pP/P and sP/P amplitude ratios plotted against the difference between pP delay time and source duration for GSETT-2 events that were recorded at more than 5 stations.

The capability of the automatic stacking procedure may be improved by tuning some of its parameters as no attempts were made to optimize the performance. The parameter settings are somewhat arbitrary, but represent, it is felt, reasonable values. Furthermore the procedure can be extended to include recordings at distances closer than 30 degrees.

Comparisons of observed amplitude ratios for pP/P and sP/P phases based on the amplitude level at the delay time predicted from focal depths determined by NEIS with those calculated from moment tensor solutions determined by HVD for 36 of the events showed little correlation. Data for only two of the events appeared to have clear correlations. The lack of correlation could be attributed to several factors; incorrect NEIS depths; invalidity of the extrapolation of the moment tensors from long to short period data; and/or interference of direct P and pP due to shallow focal depth and long source duration. Whatever the reason may be, the results illustrate the difficulty of reconciling observed amplitude ratios from those calculated from the radiation pattern of the source, although for some events there is apparent agreement between observed ratios and those predicted from simple modelling.

References

- Bratt, S.R. (1992), GSETT-2: An experiment in Rapid Exchange and Interpretation of Seismic Data, EOS, 48:513.
- Cleveland, W.S. (1979), Robust Locally Weighted Regression and Smoothing Scatterplots, JASA, 74:829-836
- Douglas, A. L. Richardson and M. Hutchins (1990), Surface reflections and S-to-P conversions on P seismograms, Geophys.J.Int., 100:303-314.
- Kennett, B.L.N. (1988), Radiation from a moment tensor source, in Seismological Algorithms (Ed. D.K. Doornbos), Academic Press, 427-442.
- Pearce, R.G. (1980), Fault plane solutions using relative amplitudes of P and surface reflections; further studies, Geophys. J. R. astr. Soc., 60: 459-487.
- Roy, F. (1984), Source depth estimation using multi-station waveform data, Bull. Seism. Soc. Am., 74, 1623-1644.

Constraining Origin Time with S/P Travel Time Ratios and Depth Estimation

Hans Israelsson

Introduction

In this note we study with synthetic examples the constraint on focal depth provided by origin times determined from travel time ratios of P and S waves. We also analyze travel time ratios for Pn and Sn waves recorded by the IMS arrays and determine and compare depths for about 70 events - presumed earthquakes as well as presumed chemical explosions in and near Fennoscandia.

Constraining Origin Time With S/P Travel Time Ratio

It is common knowledge that accurate depth determinations based on only P wave arrival times often are difficult to obtain (Lomnitz, 1977). This is due to the limitations of such observations to separate depth and origin time, which sometimes result in a near indeterminacy of the two parameters. This can be illustrated by the following somewhat simplified consideration. Assume that the epicenter of an event, the depth of which is to be determined, is known and that n observed P arrival times, to_i , with similar standard errors, s , are available for the determination. Forming the residuals, $r_i = to_i - tc_i$, between to_i and theoretical arrival times, tc_i , calculated from a tentative origin time and depth and a given travel time model, the adjustments in depth, dh , and origin time, dt , are related to the residuals, r_i , by a standard regression relation: $r_i = dt + dh (dT/dh)_i$. The depth derivative dT/dh is obtained from the travel time model (derivative for the ISAPEI91 model is shown graphically in Figure 24 as a function of distance for different depths). The variance of the dh estimated from this regression can be written as:

$$v(dh) = \sigma^2 \cdot \left[\sum \left(\frac{dT}{dh_i} - \overline{\frac{dT}{dh}} \right) \right]^{-1}$$

This means that the variance of the depth is inversely proportional to the variance of the depth travel time derivatives. The curves in Figure 1 show that the derivatives are almost constant with little variance beyond 30 degrees and that events based only on P observa-

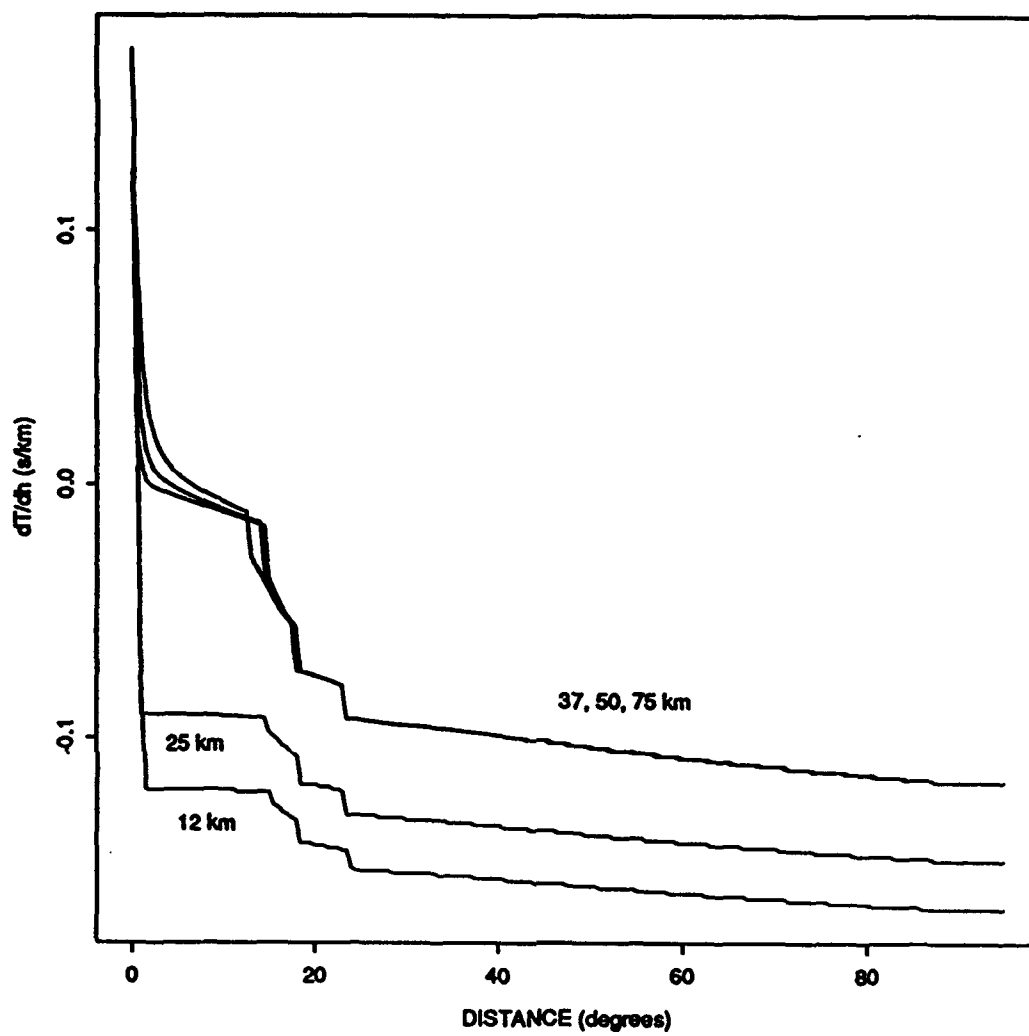


Figure 24: The derivative dT/dh as a function of distance for depths between 12 and 75 km.

tions in this distance range clearly will have depths that are poorly estimated.

If the origin time can be determined from observations of phases other than P, however, a location constrained to that origin time may provide an accurate estimate of the focal depth (Evernden, 1969). For example, arrival times of S and P waves, t_s and t_p , can be used to determine the origin time, T , if the travel time ratio for S/P waves, r , is known: $T = (r t_s - t_p)/(r-1)$. Travel time ratios for S/P waves are usually quite stable over some distance range, as illustrated by the calculated ratios for the travel times of JB, IASPEI91, and IMS in Figure 25. The standard deviations for the ratios vary from fractions of a percent to about 1%. Clearly lateral variations in travel time will increase the scatter, but travel times can be calibrated to improve precision.

Use of S arrival times by standard location algorithms will automatically improve the possibility of separating depth and origin time. Over the years, several rules of thumb on the sensitivity of focal depth solutions to the inclusion of S arrival times have been developed and studied (Gomberg *et al.* 1990). From the non-linear nature of the hypocenter determination problem, however, it is not obvious that the straightforward and standard incorporation of S arrival times provides depth solutions similar or equal to those based on an origin time constrained by S/P arrival time ratios.

In Figure 26 we show comparisons based on synthetic calculations, which suggest that a solution based on a constrained origin time may indeed have smaller standard error than a standard solution, at least under certain circumstances. In the figure, the standard deviations of estimated depths are compared for two hypothetical networks, both with 5 stations at about the same distance from the epicenter (15 degrees). The depth solutions are based on P arrival times at all stations and on S times at one and five stations in the upper and lower frames respectively. Algorithms in a hypocenter determination program, (LOCEX) originally developed by Julian (1974) were employed in the simulations. Gaussian arrival time errors obtained by a random noise generator were added to theoretical arrival times and depths were estimated for 3000 event randomizations at depths going from 10 to 50 km in steps of 2 km. In the simulations we assumed that the S/P travel time ratio was without error. The dashed lines in the two frames to the right represent standard error equal to actual depth. The depths obtained from constrained origin times have systematically smaller standard deviation, up to about a factor of 1.5 - 2, than the standard depth solutions. The differences are less pronounced in the case with 5 S_n phases. Constraining the origin time with the S_n/P_n travel time ratio in the case with only one S_n phase gives much more weight to the S_n observation than the free depth location does and it may therefore be possible to reduce the standard deviations with the free depth solution if the S_n observations were given more weight.

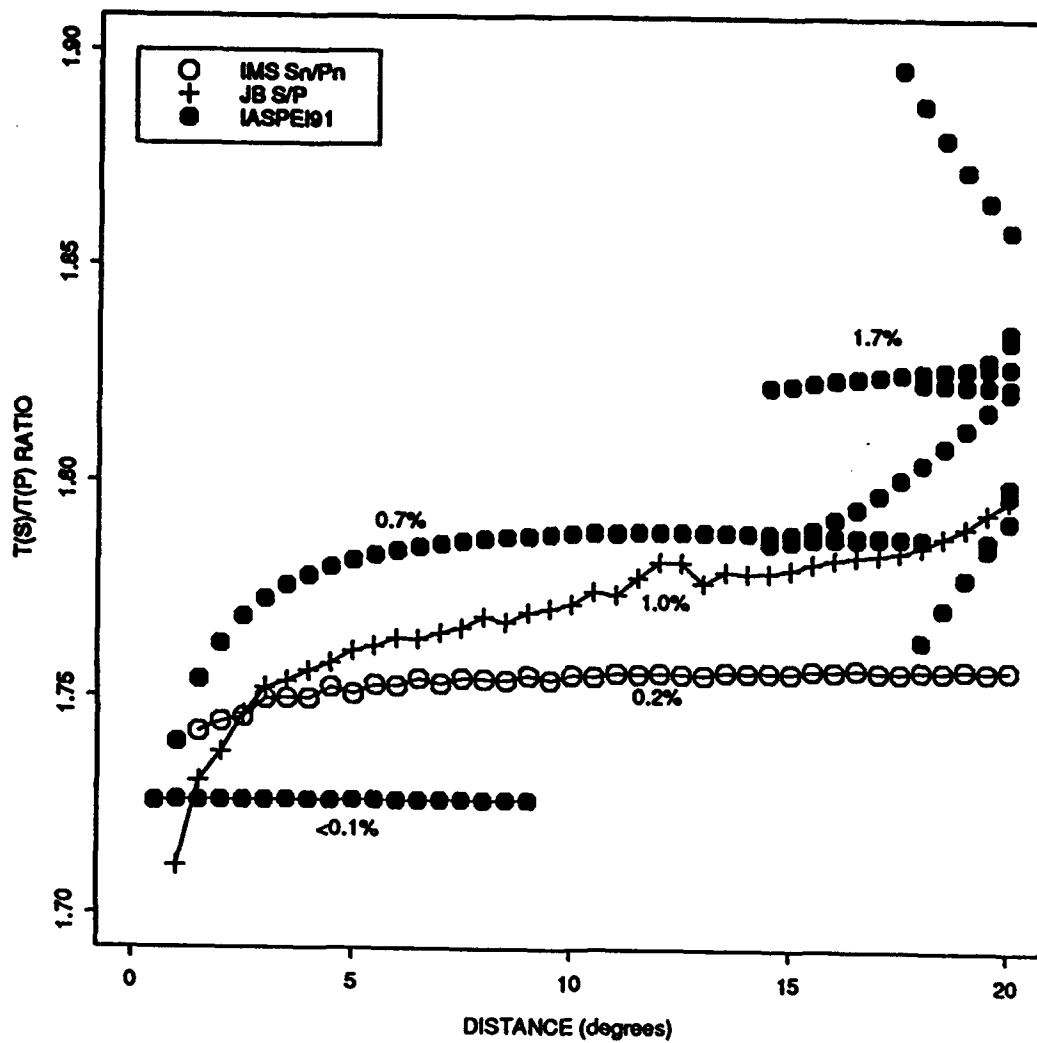


Figure 25: The ratio for travel times of S and P as a function of epicentral distances for different velocity models.

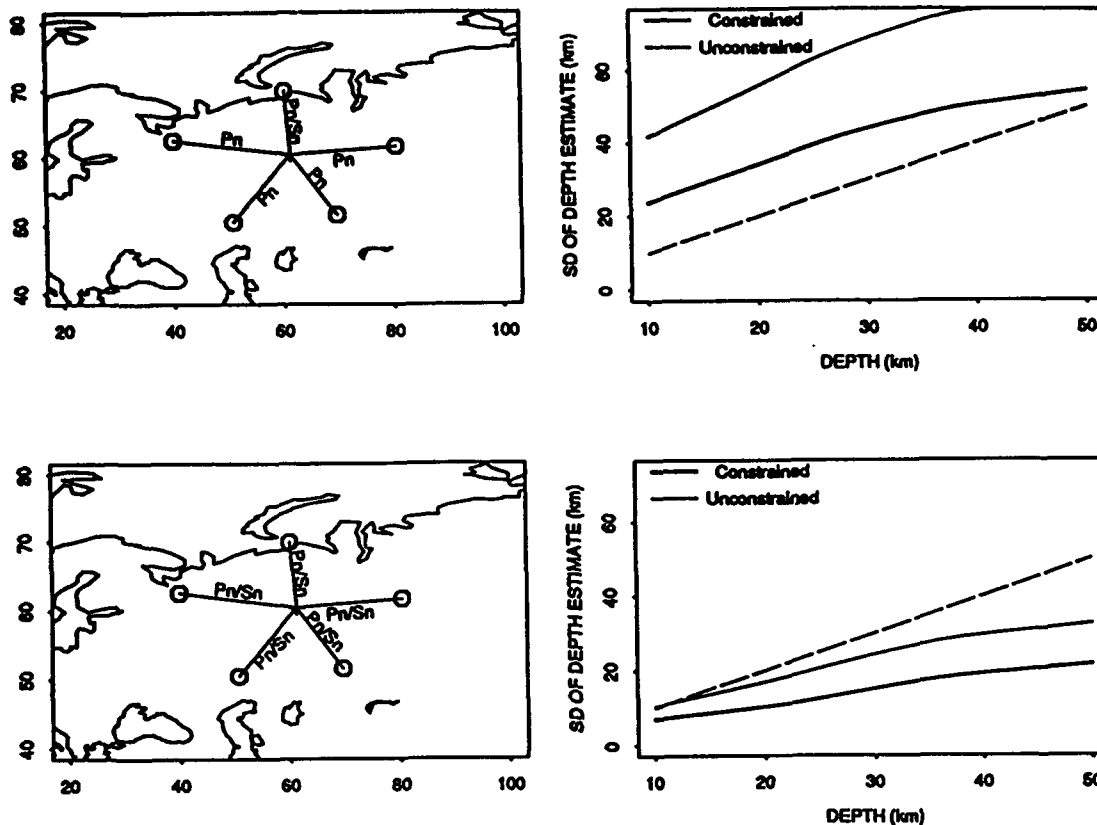


Figure 26: Comparisons of the standard deviations of the depth estimates obtained with and without constrained origin times for two synthetic examples, with recorded phases of Pn and Sn as illustrated by the maps to the left.

Ts/Tp Ratios From IMS Data

In order to get some idea of the stability of the S/P travel time ratio we analyzed arrival times for Pn and Sn in the IMS data base. The results are summarized in Figure 27 by comparisons of origin times determined from Pn and Sn arrival times at the three arrays in Fennoscandia. For each pair of arrays, a ratio, r , was fit to the computed origin times of common events that minimized the differences in origin times. The bias and the standard deviations, SD, given for each array pair in the figure were obtained as the median of the differences in origin time and a robust estimate of the standard error. We note that the values vary somewhat among array pairs with a range of about 1%. Furthermore, the values that involve the ARCESS array (ARA0) are also slightly higher than 1.756, which is the average value for Sn/Pn over the distance range 5 to 20 degrees in the travel time tables used by IMS. The estimates of the S/P travel time ratios obtained here are completely independent of the IMS or any other travel time model. The estimated standard deviation of the origin time based on one observation is 2-2.5 s.

A large standard error in the S/P travel time ratio will clearly result in a large standard error of the origin time as illustrated by Figure 28, which shows curves for standard error in origin time as a function of epicentral distance. The curves were obtained by simulations using a Gaussian random number generator and assuming standard errors of 0.7 and 1.4 s in P and S arrival times, respectively.

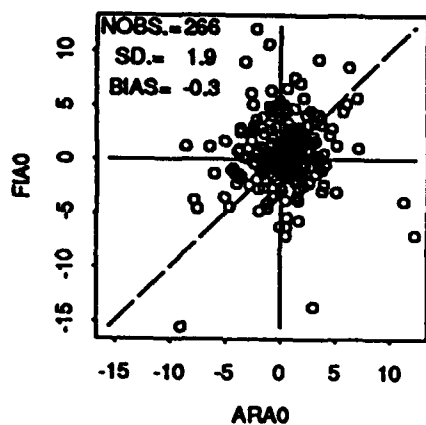
If we assume that the standard errors in the arrival times of P and S, sp and ss respectively, are independent and that $ss = 2 sp$, we can estimate the standard error in sp from the estimates of the standard error of the origin time, sT , in Figure 27. The formula above gives $sp = 0.7$ s and $ss = 1.4$ s. These estimates are comparable to the standard deviations of the residuals for Pn and Sn arrival times shown in Figure 29. The SD1's are robust estimates (include about 98% of the data) and the SD2's include all data i.e., outlying observations.

Some of the scatter in the arrival time residuals above may be a result of the uncertainty in the determinations of the event locations. The ground truth data base at CSS (Grant and Coyne, 1992) provide epicenter determinations independent of the IMS locations. Here we use observations for a suite of earthquakes near Steigen in Northern Norway (see map in Figure 30) to analyze residuals and S/P travel time ratios. The map in Figure 31 shows the clustering of the events which, with the exception of 2 events, are within 10 km. The epicenter determinations were reported by Bergen Seismological Observatory in Norway and were based on measurements at a local network of 5 stations.

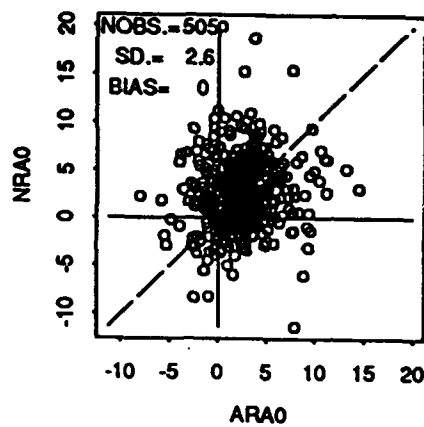
The arrival time residuals for Pn and Sn - defined as observed arrival time minus that computed with the IMS travel time model and the origin times reported by Bergen - shown in Figure 32 show significant scatter. Apart from measurement errors, the large scatter may be

Comparison of origin times from Sn-Pn times

ts/tp ratio= 1.76



ts/tp ratio= 1.774



ts/tp ratio= 1.754

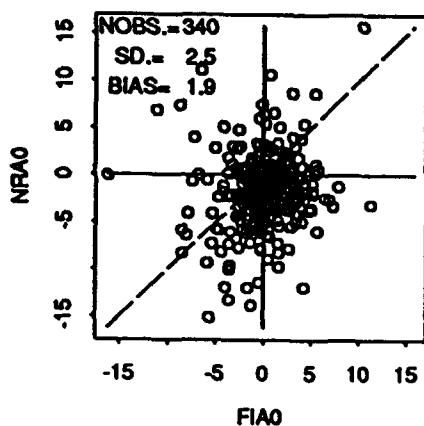


Figure 27: Comparisons of origin times calculated from travel time ratios of S and P waves and the associated estimates of the travel time ratios.

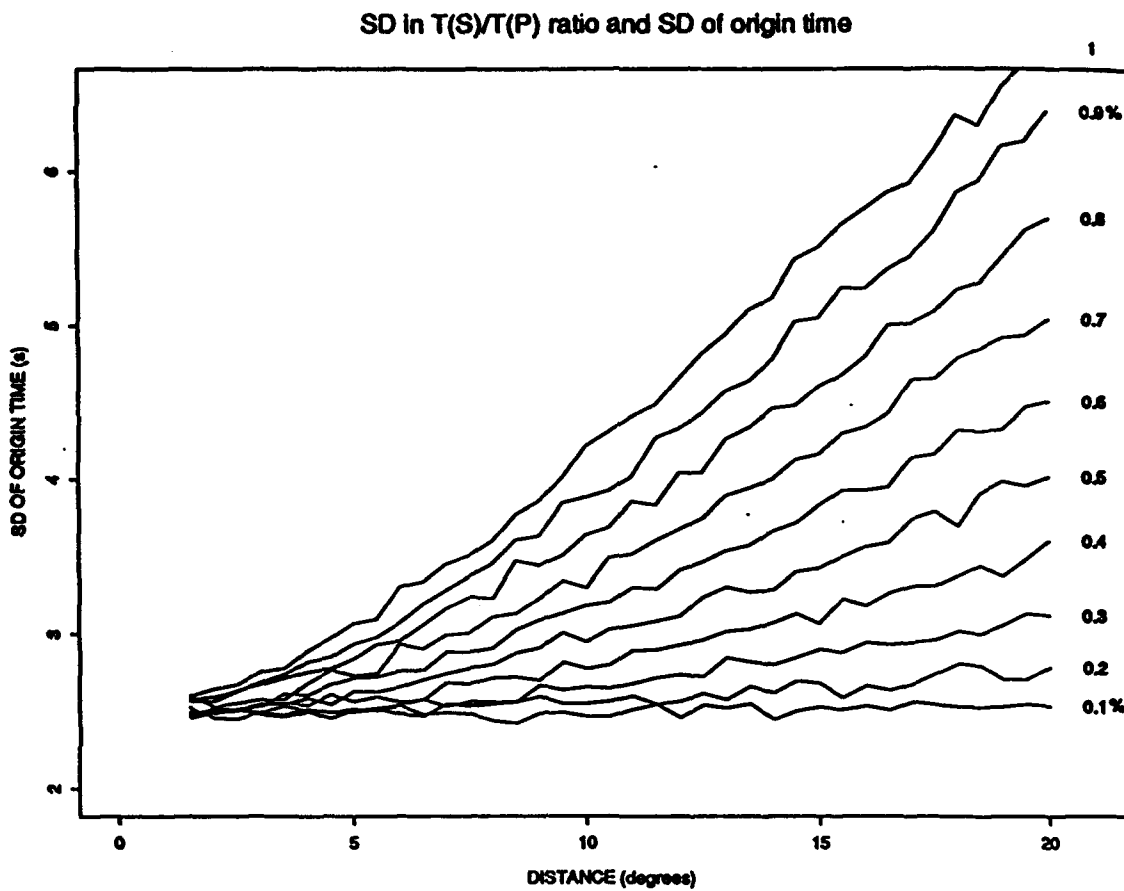


Figure 28: Standard deviation of origin time for different standard deviations in the S/P. from 0.1 to 1 per cent, as a function of epicentral distance. The curves were obtained with a Gaussian random number generator with the standard deviations of the P and S arrival times being 0.7 and 1.4 s, respectively.

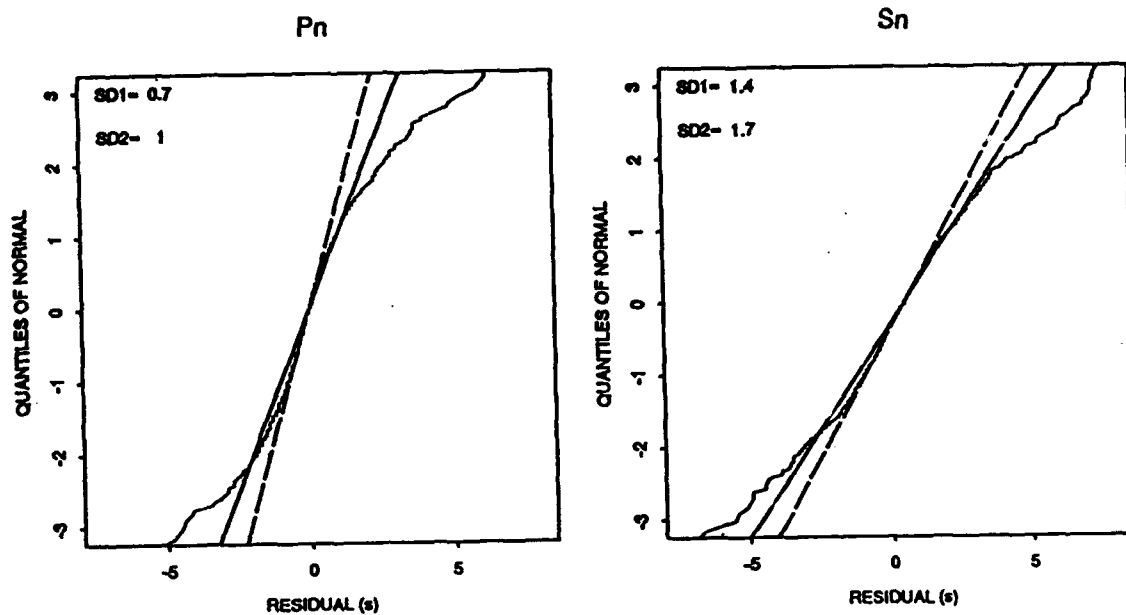


Figure 29: Empirical distribution functions of P_n and S_n arrival time residuals for IMS data. The lines represent approximations to Gaussian distributions; the dashed and solid lines correspond to robust and conventional estimates of the standard deviations ($SD1$ and $SD2$ respectively).

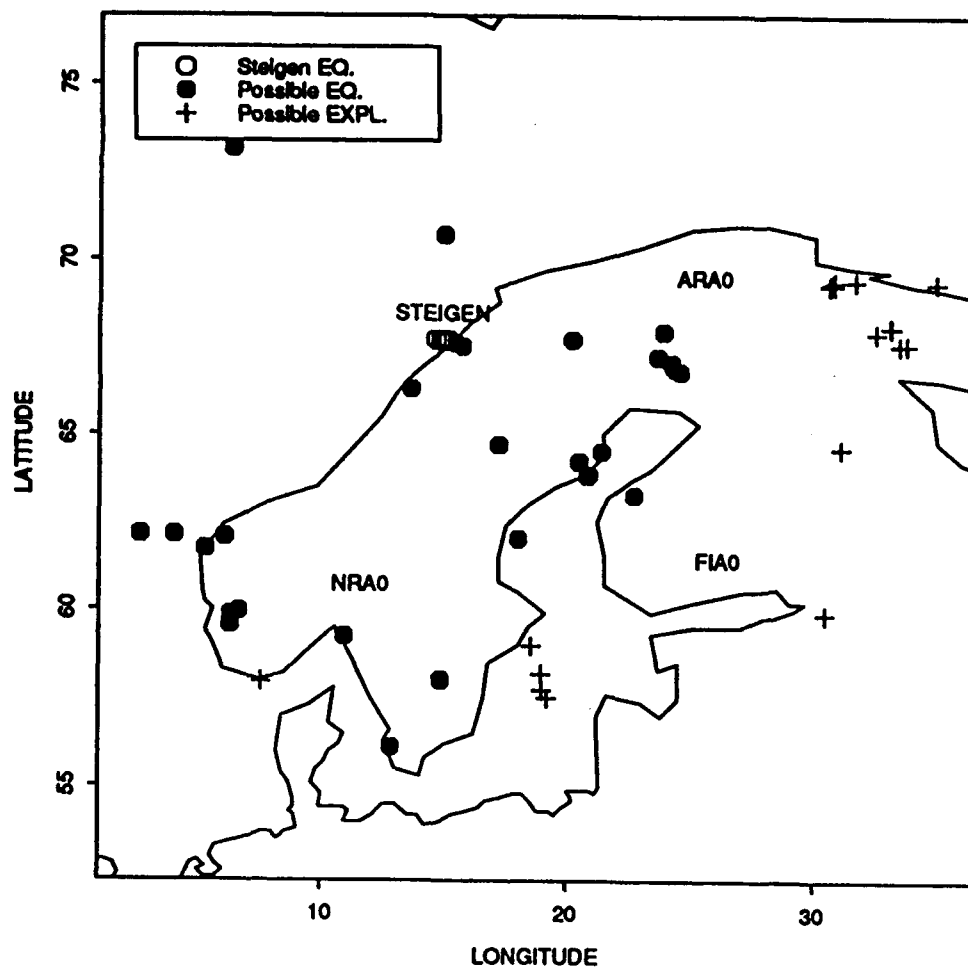


Figure 30: Epicenters of the events that were analyzed and the locations of the mini arrays.

Epicenters Steigen earthquakes

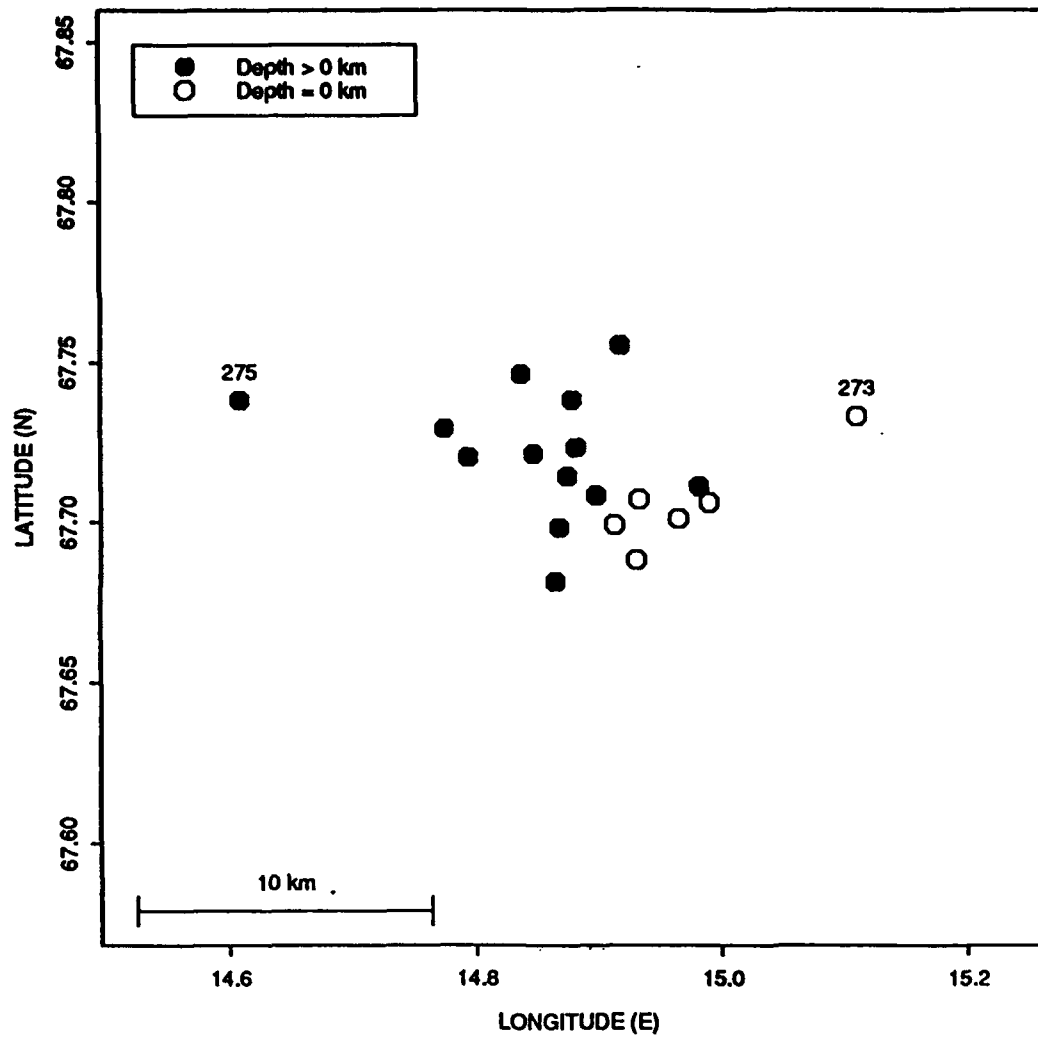


Figure 31: Epicenters of the Steigen earthquakes determined by the Bergen Seismological Observatory.

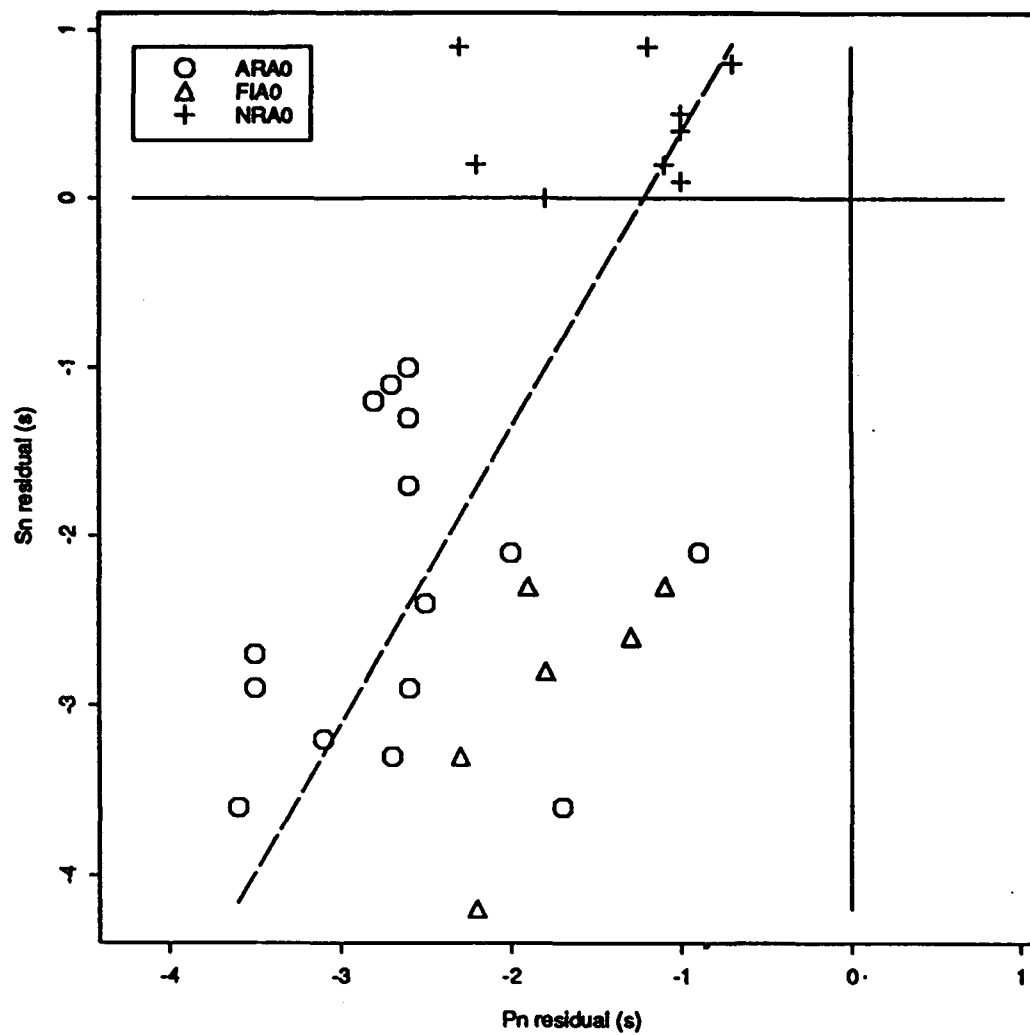


Figure 32: Comparison of Pn and Sn residuals of the Steigen earthquakes.

caused by errors in the origin times. Except for two outlying data points each for ARA0 and NRA0, the Pn and Sn residuals for a given array also correlate as one might expect with the derivative, $dT(Sn)/dT(Pn)=1.75$, indicated as a dashed line in the diagram. However, the median residuals for Pn and Sn also suggest lateral variations in Pn and Sn as indicated by Table 4. The fastest Pn travel time, to ARA0, is about 1.5s less than that to NRA0. We also note that the Sn travel times to these arrays are about 2 s slower than one would expect from a 1.75 S/P travel time ratio, whereas the travel time of Sn to FIA0 relative to P is more in accordance with a 1.75 S/P ratio.

The scatter in the Pn and Sn residual is also reflected in the S/P travel time ratios, which are all slightly above that for the IMS travel time tables (Figure 33). We note that both NRA0 and ARA0 appear to have larger ratios than does FIA0.

Examples of Depth Estimation Using IMS Data

We applied the LOCEX program to events shown in the map of Figure 30, both with a free depth and with the origin time constrained by the S/P travel time ratio. The events and the resulting depth estimates are listed in Table 4. The events include the suite of 14 earthquakes near Steigen analyzed above. In addition there are two groups of events, the nature of the source of which has not been firmly established, but which are likely to be earthquakes and explosions - mining or under water. These two event types are indicated as possible earthquakes and explosions respectively in Table 4 and are marked with different symbols in Figure 30.

The point estimates of the two types of depth estimates are compared in Figures 34 and 35. The scatter diagram in Figure 34 shows that the two types of estimate generally agree, but there are also differences. Several of the events designated possible explosions are placed at depths below 1 km by the free depth method. Furthermore, there are several possible earthquakes that have point estimates at zero depth for the free depth method. Apparent inconsistencies like these can be noted for depth estimates based on constrained origin time as well, but they appear less frequently as demonstrated by the histograms in Figure 35, where the empirical distributions of the depth estimates of the two kinds of events and the two methods are compared.

The differences observed in the two kinds of depth estimates is no evidence that depth from constrained origin time would generally provide the more accurate depth for several reasons. For one thing, the data analyzed here is limited to a fairly small number of events, the exact depths of which are not known. Furthermore, the uncertainties of the point estimates have not been analyzed here as that would require some consideration beyond standard statistical practice for the depths based on constrained origin times. Nevertheless it is

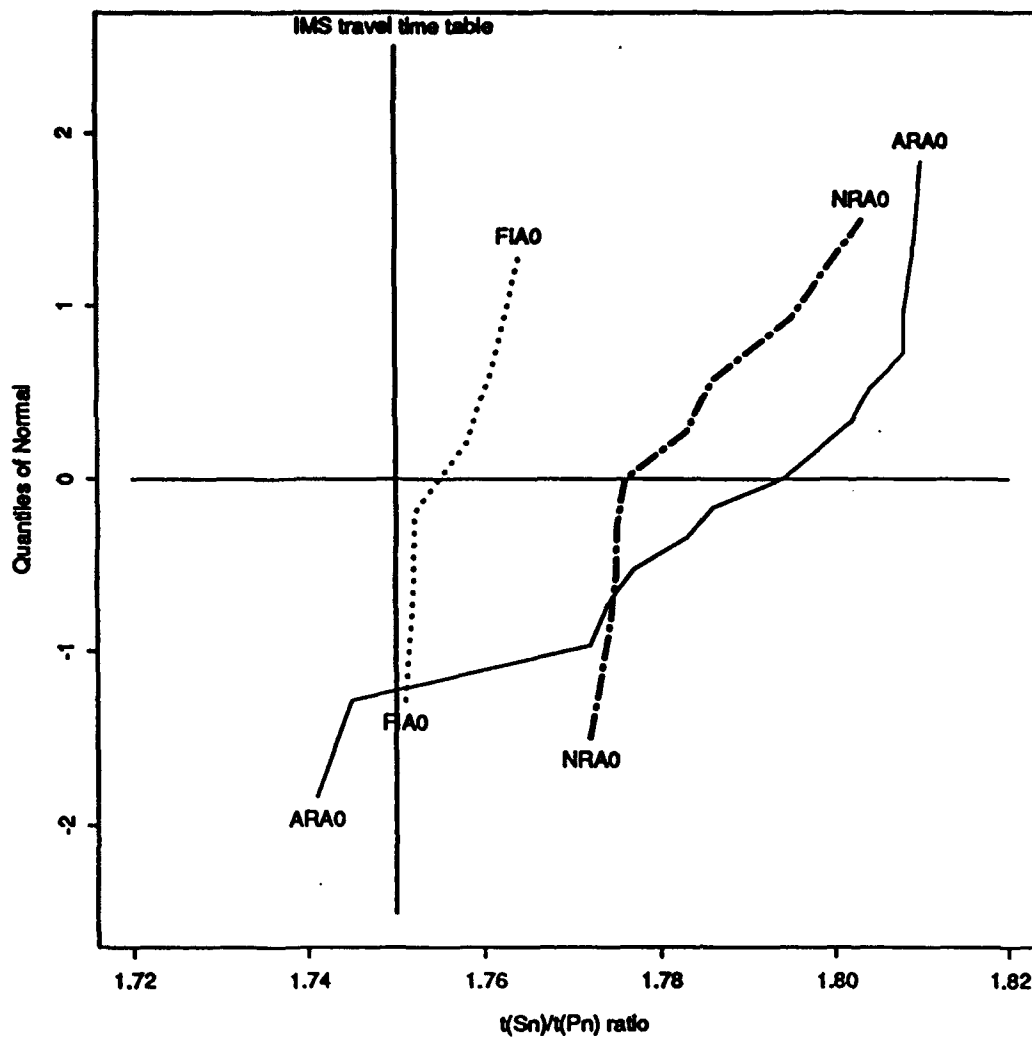
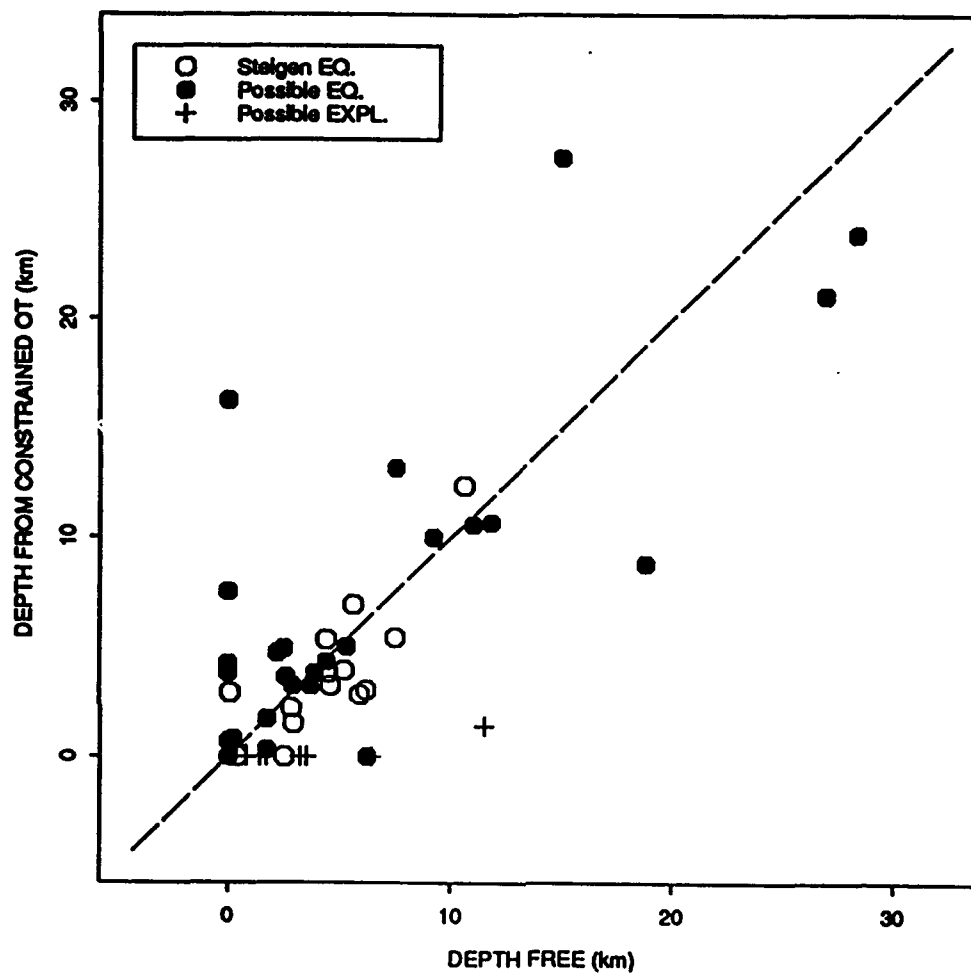


Figure 33: Empirical distribution functions of the S/P travel time ratios to ARA0, FIA0, and NRA0 for the Steigen earthquakes.



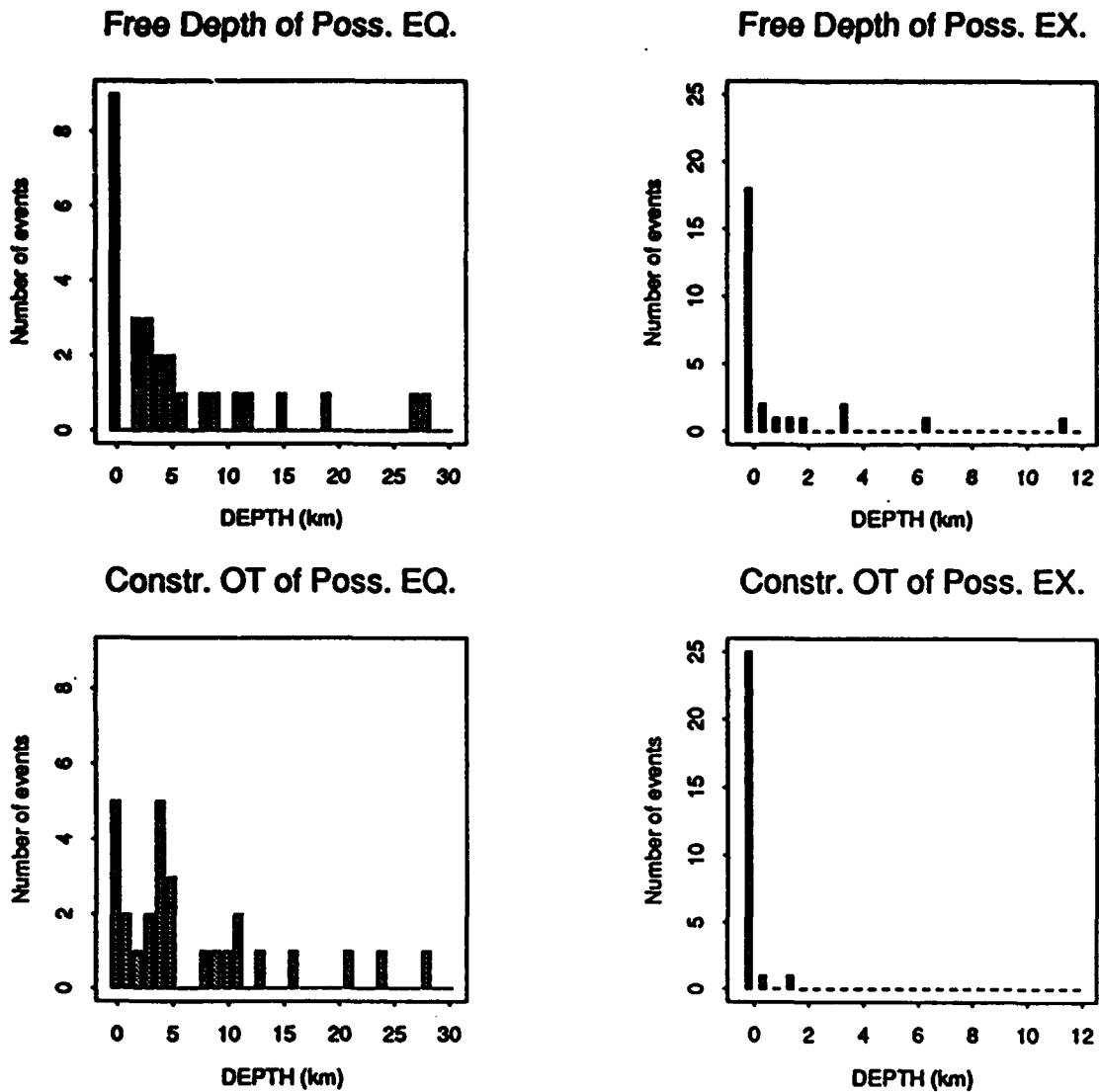


Figure 35: Histograms of depths for possible earthquakes and mining events determined with conventional free depth method and with origin times constrained with S/P travel time ratio.

felt that the results warrant further analyses and comparisons of the qualities of depth estimates based on constrained origin times.

Concluding Remarks

In this note we have used simple simulations and calculations on actual data to compare depth estimates obtained by standard location algorithms with those based on origin times constrained with S/P travel time ratio. Because of the limited scope of the simulations and the data analyzed the observed improvement in the depth estimates based on constrained origin times has to be confirmed with more comprehensive evaluations. The variability in the estimates of S/P ratio for Fennoscandia also suggest that to be truly useful, the regional dependence of has to be mapped.

References

- Evernden, J.F. (1969), Identification of earthquakes and explosions by use of teleseismic data, *J. Geophys. Res.*, 74: 3828-3856.
- Gomberg, J.S., Shedlock, K. M. and S.W. Roecker (1990), The effect of S-wave arrival times on the accuracy of hypocenter estimation, *Bull. Seism. Soc. Am.*, 80: 1605-1628.
- Grant, L and J. Coyne (1992), Ground Truth Data for Seismic Discrimination, in *Proceedings of the 14th annual PL/DARPA Seismic Research Symposium*, 16-18 September, (Eds. J.F. Lewkowitz and J.M. McPhetres), Phillips Laboratory, Hanscom Air force Base, MA. Report PL-TR-92-2210
- Lomnitz, C. (1977), A procedure for eliminating the indeterminacy in focal depth, *Bull. Seism. Soc. Am.*, 67:533-535.

Table 4: Event source parameters and depth estimates

IMS Hypocenter Solution						Depths (km)		Type of event
Date	origin time	Lat.	Lon.	Depth	ML	Free	Const r. OT	
90/02/06	22:55:42	63.28	22.67	0.0	1.52	3.9	3.8	Poss. eq.
90/03/29	04:11:19	62.07	6.06	0.0	2.30	2.2	4.7	Poss. eq.
90/05/24	09:51:50	56.12	12.82	0.0	1.52	26.9	21.1	Poss. eq.
90/08/22	04:08:30	63.86	20.81	0.0	2.12	11.0	10.6	Poss. eq.
90/10/28	02:26:10	66.85	24.50	0.0	1.97	18.8	8.8	Poss. eq.
90/10/30	23:08:11	67.65	15.41	0.0	2.29	9.2	10.0	Poss. eq.
91/04/17	17:47:29	67.11	24.16	0.0	2.11	0.0	4.2	Poss. eq.
91/06/13	10:48:23	67.75	20.16	0.0	2.49	0.0	0.0	Poss. eq.
91/07/13	01:42:21	67.99	23.86	0.0	2.19	1.7	0.3	Poss. eq.
91/09/23	19:20:28	64.52	21.34	0.0	3.15	0.0	7.5	Poss. eq.
91/10/28	13:14:34	59.57	6.28	0.0	2.75	0.0	16.3	Poss. eq.
91/10/28	16:21:27	63.83	20.78	0.0	2.15	0.0	0.0	Poss. eq.
91/11/08	01:20:36	58.01	14.84	0.0	2.21	6.2	0.0	Poss. eq.
91/12/11	16:00:23	66.95	24.26	0.0	2.19	4.4	4.3	Poss. eq.
91/12/15	15:18:48	62.03	17.99	0.0	2.74	5.3	5.0	Poss. eq.
92/01/01	08:03:58	67.75	14.84	12.1	4.50	0.1	2.9	Steigen eq.
92/01/01	08:39:02	67.72	14.85	12.1	1.60	2.9	1.5	Steigen eq.
92/01/04	03:43:43	67.71	14.93	0.0	2.00	2.5	0.0	Steigen eq.
92/01/04	04:15:04	67.71	14.90	12.1	3.60	5.6	6.9	Steigen eq.
92/01/04	06:00:53	67.70	14.87	12.1	5.50	7.5	5.4	Steigen eq.
92/01/04	09:06:31	67.75	14.92	12.1	2.50	4.4	5.3	Steigen eq.
92/01/05	01:20:50	67.73	14.78	15.5	1.70	5.2	3.9	Steigen eq.
92/01/05	05:11:56	67.71	14.99	0.0	1.50	10.6	12.4	Steigen eq.

Table 4: Event source parameters and depth estimates

IMS Hypocenter Solution						Depths (km)		Type of event
Date	origin time	Lat.	Lon.	Depth	ML	Free	Const r. OT	
92/01/06	08:26:22	67.70	14.96	0.0	1.30	4.6	3.2	Steigen eq.
92/01/10	07:46:36	67.27	23.63	0.0	2.44	7.5	13.2	Poss. eq.
92/01/10	22:25:42	67.71	14.98	2.2	-9.99	2.8	2.2	Steigen eq.
92/01/25	11:57:34	67.69	14.93	0.0	1.80	0.4	0.0	Steigen eq.
92/01/25	12:16:48	67.71	14.88	12.1	3.80	5.9	2.8	Steigen eq.
92/01/25	12:26:29	67.73	15.11	0.0	1.90	6.2	3.0	Steigen eq.
92/01/25	19:12:52	67.74	14.61	12.1	1.80	4.5	3.8	Steigen eq.
92/02/19	06:39:33	59.24	10.89	24.5	3.26	28.3	23.9	Poss. eq.
92/04/16	10:21:43	64.23	20.43	0.0	2.34	0.0	0.7	Poss. eq.
92/06/10	08:22:07	58.98	18.53	0.0	2.58	0.0	0.0	Poss. expl.
92/06/10	11:46:33	69.32	30.56	0.0	2.71	0.0	0.0	Poss. expl.
92/06/19	11:35:40	69.29	30.56	0.0	2.66	0.0	0.0	Poss. expl.
92/06/20	23:01:32	67.56	15.68	6.8	2.74	0.2	0.8	Poss. eq.
92/06/23	12:21:33	58.19	18.96	0.0	2.50	0.0	0.0	Poss. expl.
92/06/23	12:36:11	57.52	19.20	0.0	2.60	0.0	0.0	Poss. expl.
92/06/23	12:40:30	57.73	18.99	0.0	2.51	0.0	0.0	Poss. expl.
92/06/28	12:23:33	61.74	5.29	0.0	2.62	2.5	4.9	Poss. eq.
92/07/01	07:12:23	59.88	30.45	0.0	2.54	0.0	0.0	Poss. expl.
92/07/03	11:32:54	69.37	30.71	0.0	2.52	0.8	0.0	Poss. expl.
92/07/11	14:32:28	62.13	4.03	7.3	2.64	15.0	27.4	Poss. eq.
92/08/03	11:16:02	66.32	13.58	11.8	2.69	11.8	10.7	Poss. eq.
92/08/06	07:32:41	59.85	6.30	4.7	3.15	3.7	3.2	Poss. eq.
92/08/28	18:37:52	59.94	6.62	8.6	2.63	2.9	3.2	Poss. eq.

Table 4: Event source parameters and depth estimates

IMS Hypocenter Solution						Depths (km)		Type of event
Date	origin time	Lat.	Lon.	Depth	ML	Free	Const r. OT	
92/09/23	11:37:02	69.38	30.73	0.0	2.62	1.7	0.0	Poss. expl.
92/09/30	12:22:51	69.30	30.77	0.0	2.86	0.0	0.0	Poss. expl.
92/10/17	02:19:38	62.14	2.65	0.0	2.98	2.6	3.6	Poss. eq.
92/10/23	14:50:23	69.38	34.92	0.0	2.54	3.2	0.0	Poss. expl.
92/10/30	12:54:53	69.39	30.73	0.0	2.78	0.0	0.0	Poss. expl.
92/11/18	10:20:08	64.61	31.07	0.0	2.69	0.0	0.0	Poss. expl.
92/11/20	13:26:30	69.29	30.61	0.0	2.89	6.4	0.0	Poss. expl.
92/11/22	04:46:45	67.61	33.47	0.0	2.57	0.0	0.0	Poss. expl.
92/11/30	14:10:39	69.42	31.64	0.0	2.90	0.0	0.0	Poss. expl.
92/12/11	13:16:31	69.31	30.62	0.0	2.59	0.0	0.0	Poss. expl.
92/12/18	12:09:52	68.11	33.13	0.0	2.62	3.5	0.0	Poss. expl.
92/12/25	12:29:41	69.43	30.79	0.0	2.69	0.0	0.0	Poss. expl.
92/12/30	11:30:59	67.94	32.50	0.0	2.55	11.5	1.4	Poss. expl.
92/12/30	15:05:25	69.34	30.65	0.0	2.74	0.0	0.0	Poss. expl.
93/01/05	10:19:35	64.71	17.17	1.8	3.66	0.0	3.8	Poss. eq.
93/01/08	21:44:08	73.17	6.30	0.0	2.82	1.7	1.7	Poss. eq.
93/01/11	04:11:48	57.95	7.58	0.0	2.75	0.4	0.5	Poss. expl.
93/01/15	12:28:23	69.35	30.63	0.0	2.50	0.0	0.0	Poss. expl.
93/01/16	12:30:11	68.12	33.07	0.0	2.67	1.4	0.0	Poss. expl.
93/01/29	12:40:20	69.38	30.69	0.0	2.82	0.0	0.0	Poss. expl.
93/01/30	13:07:09	67.62	33.76	0.0	2.53	0.0	0.0	Poss. expl.
93/02/05	12:13:38	69.39	30.74	0.0	2.64	0.1	0.0	Poss. expl.
93/02/05	16:07:56	70.71	14.92	0.0	2.58	0.0	0.0	Poss. eq.

Assessing Depth Estimation Capability: Examples for Global Networks

Hans Israelsson

Introduction

Estimating the depth of seismic events is one important function of station networks. Depth is an important discriminant for differentiating between explosions and earthquakes and it is an important parameter in studies of seismic activity and associated geophysical processes. Yet the capability to estimate depths of seismic networks are rarely established and station networks are rarely designed to allow depth estimation in an optimum manner.

In this note we perform some computational experiments to outline the depth estimation capability of the GSETT-2 global network and a hypothetical network consisting primarily of high sensitive array stations. We also discuss the use of stations in the oceanic areas to supplement the hypothetical network to enhance its capabilities of depth estimation in the oceans.

The Networks

Simulations of the detection capability of the GSETT-2 network (see Bratt, 1992) have been carried out by Bratt (1993) and are summarized in the map of Figure 36a. The contours were obtained by the NetSim software package (Serenio et al., 1990) and parameters developed and employed by Bratt (1993). The capabilities can be compared with that of a hypothetical network of 50 sensitive stations (ALPHA network) in Figure 36b (also studied by Bratt, 1993). Finally, in Figure 36c are the contours of the detection threshold for another hypothetical network consisting of the ALPHA network supplemented with 50 oceanic stations, selected from sites of existing or previously operated seismic stations in oceanic areas, with noise and detection characteristics equal to those of a typical oceanic station (SNZO) of the GSETT-2 network. The potential of oceanic stations for explosion monitoring have earlier been analyzed and discussed by Phillips and McCowan (1978). Median thresholds, ranges, and standard deviation are given for different geological regions - oceanic, tectonic, shield/platform - following the regionalization by Jordan (1981). We are systematically using medians instead of mean values since grid points for which capabilities are calculated may be close to some stations and therefore will be low. Similarly, we use a robust estimate of the standard deviation that is insensitive to outlying data values. The ALPHA network has a more uniform detection capability although the

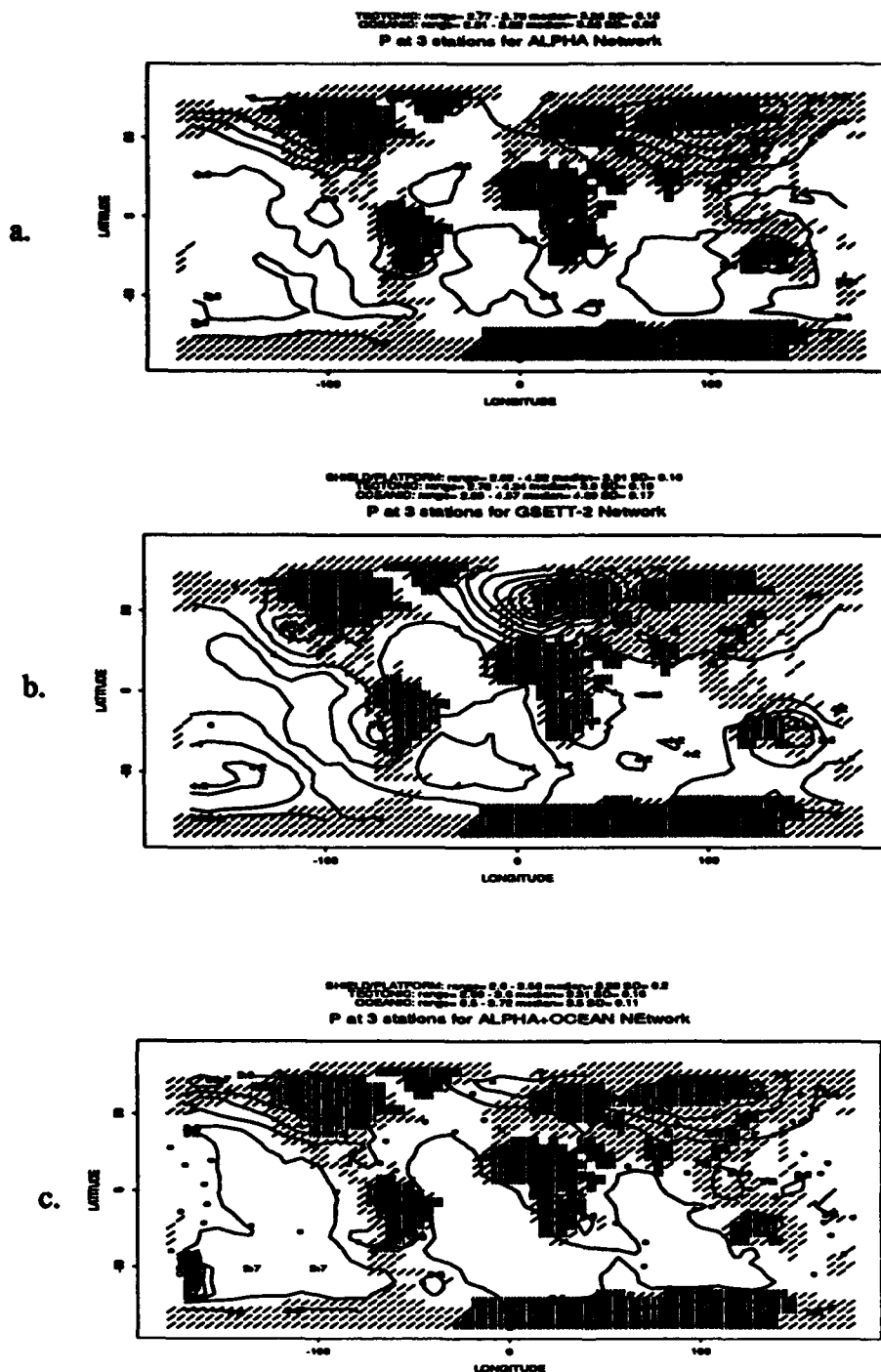


Figure 36: The 90% detection thresholds of the GSETT-2 network (a), the ALPHA network (b), and a network consisting of the ALPHA stations and 50 oceanic stations (c).

detection threshold is about two tenths of a unit higher in oceanic areas than in other areas.

Station detection thresholds for the teleseismic detection window at the 50% level are shown in the histograms of Figure 37. They were obtained as the median thresholds from NetSim calculations with one station networks. Since the medians represent detection thresholds at 90 degrees distance, a factor of 0.35 magnitude units (corresponding to the attenuation difference between 90 and 60 degrees, 60 degrees being in the center of the teleseismic detection window) were subtracted. These thresholds showed close agreement with thresholds for the GSETT-2 station distribution obtained from comparisons of detected and undetected events reported by the NEIS. The mb(NEIS) were corrected for bias using empirical corrections from the results of Ringdal (1986). The distribution of the detection thresholds for the ALPHA+OCEANIC network is dominated by the 50 oceanic stations. Phillips and McCowan (1979) refer to observations of low noise levels in one early ocean seismometer experiment. Subsequent studies have, however, not substantiated these early observations (Hedlin and Orcutt, 1989). Hence the large noise amplitude and comparatively high detection threshold for the oceanic stations.

Depth Estimation and Simulations

There are several techniques for estimating focal depth, the most commonly employed of which is the estimation resulting from the standard location of first arrival times of P phases. It is common knowledge that such estimates are usually associated with large uncertainties unless the variance of the travel time derivatives with respect to depth of the recording stations is large. Depth estimates based on secondary phases often can often dramatically improve the quality of the estimate, but secondary phases are not always available.

Depth estimates used for the purpose of explosion monitoring do not necessarily have the same requirements as those for precise focal depth determinations of earthquakes. For example, assessing depth accuracy based on S wave arrival times (one of the most efficient depth estimation methods) Gombert et al. (1990) concluded that in order to achieve an accuracy of about 1.5 km would require S waves recorded within 1.4 times the focal depth. Applying this criterion for world-wide seismicity would require a network with a very large number of stations. For explosion monitoring it is merely sufficient to establish that the focal depth is deeper than some limit, say 10 km. Here, however, we will look at actual depth estimates rather than upper limits. We analyze depth estimation based on two kinds of secondary phases (1) surface reflected pP and sP recorded at teleseismic distances and (2) S waves recorded primarily at regional distances.

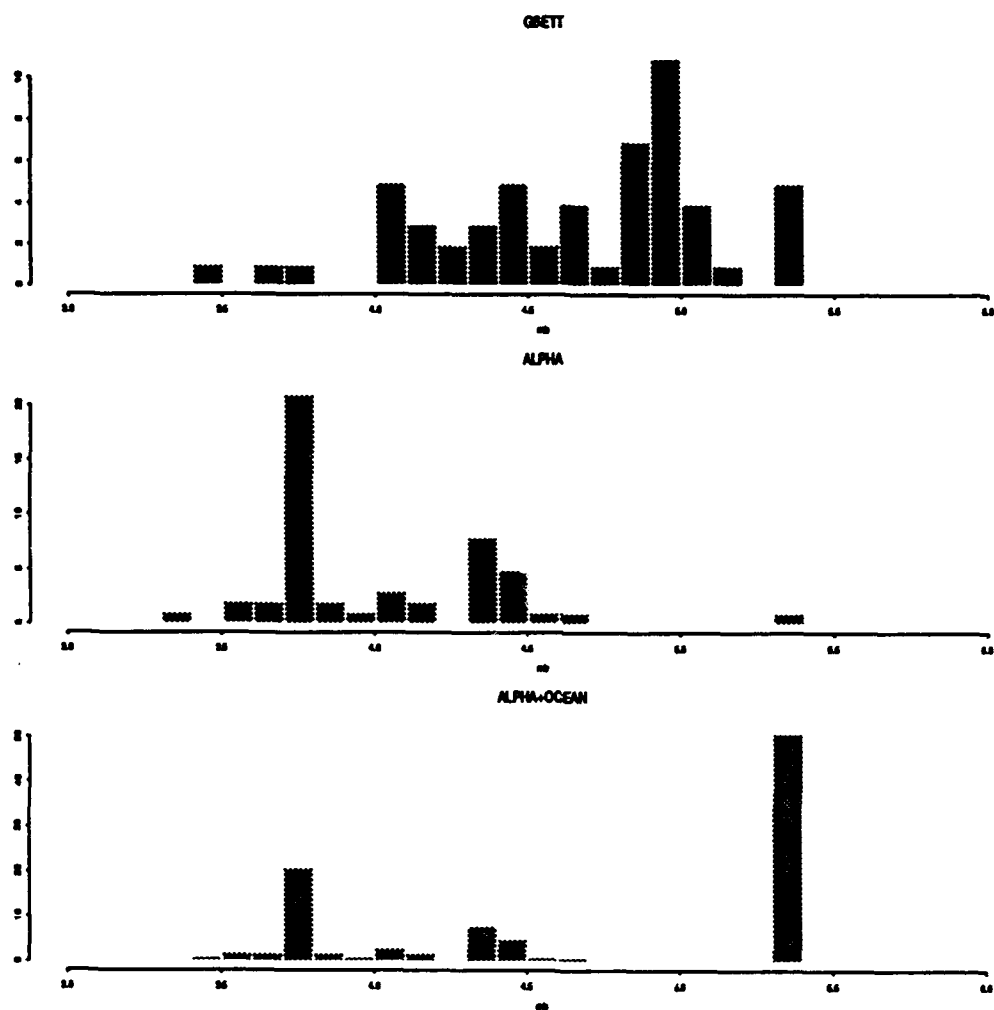


Figure 37: The 50% detection thresholds of the teleseismic window for station in the GSETT-2 and ALPHA networks and a network consisting of the ALPHA stations and 50 oceanic stations.

Surface Reflected Phases - Moveout and Azimuthal Coverage

From past experience it appears that the observability of depth phases, pP and sP, from earthquakes is, in many instances unpredictable, and is therefore difficult to model. Simple models for the radiation pattern of double couple sources of short duration, 1 s or so, have in several cases been demonstrated to accurately describe the excitation and recording of such these phases. It appears, however, that the success rate of this model has not been firmly established and it seems that in a large number of cases, other factors dominate the character of recorded P seismograms (Douglas et al., 1990). Therefore we limited the modelling of the accuracy of depths determined from depth phases to simple factors that from experience control their observability to some degree azimuthal coverage of recording stations, and the degree of moveout of the depth phases that recording stations may provide. Both these factors are determined by the geometry of the station network. Only stations that detect the event in the teleseismic window (30-90 degrees) are assumed to contribute to moveout and azimuthal coverage. This is somewhat conservative as depth phases may be detected and positively identified at shorter distances in spite of the complexity of regional wave propagation.

The moveout is given as the percentage observed of the total moveout possible in the distance range 30 to 90 degrees and was obtained by Monte Carlo simulations similar to those employed in the location module of the NetSim program (Serenio et al., 1990). For a given network - GSETT and ALPHA - the moveout provided for an event with given location and magnitude represents the average of a large number of randomizations of signal and noise amplitudes assuming the 50% detection thresholds shown in Figure 37. The results are summarized in Figure 38 for the GSETT and the ALPHA networks; the ALPHA and ALPHA+OCEAN network provided very similar results. For each of the two networks in Figure 38, the median of the percent moveout is shown as a function of magnitude. Medians are given according to type of geological region - oceanic, tectonic, and shield/platform. The median of the detection thresholds for the three types of geological region (see Figure 36a-b) are also indicated on the diagrams as a shaded zone for the sake of comparison. We note that the ALPHA network reaches close to 100% moveout at about magnitude 4.0 and only at the low end of the range for the detection thresholds does the moveout go below 50%. The trend for the GSETT-2 network relative to its detection thresholds is rather similar, except that even at larger magnitudes, 100% moveout is not attained.

In Figure 39 we compare similar curves for the azimuthal coverage given as the percentage of 8, 45 degree azimuth sectors, in which the event was detected. The results in Figure 39 were obtained with simulations similar to those used for the moveout. For each simulation, the azimuthal coverage of the detecting stations was calculated by counting the num-

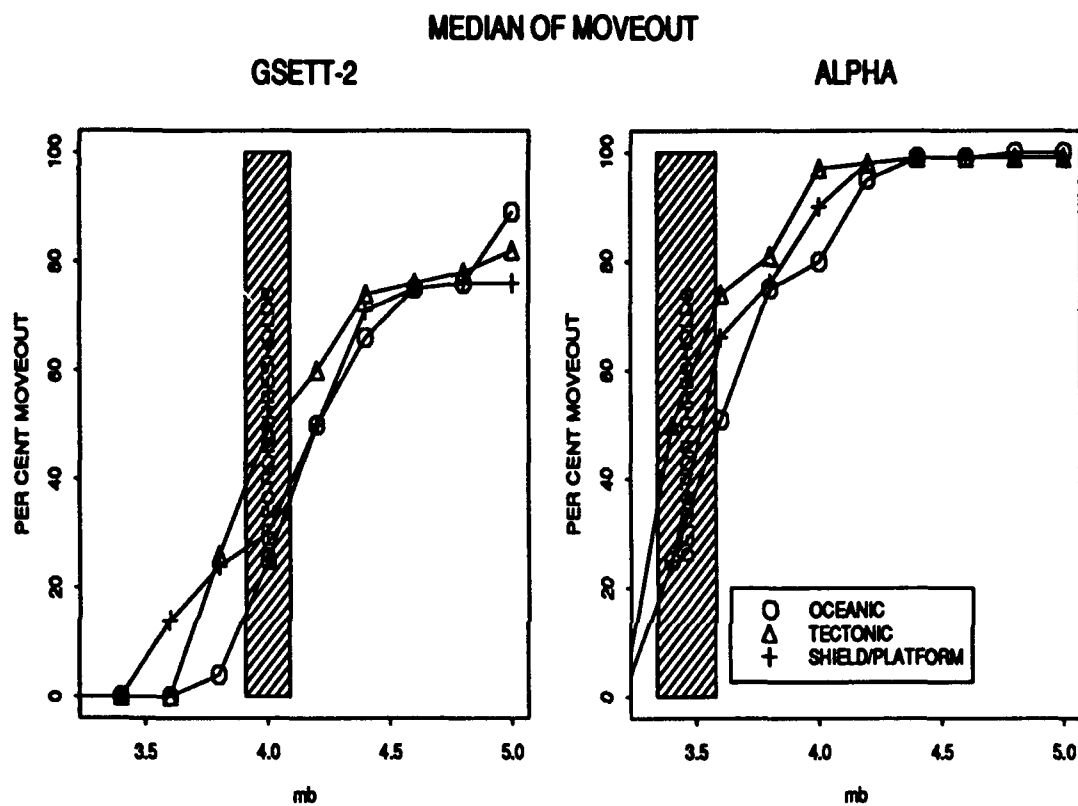


Figure 38: Median of the moveout observed of the total possible moveout in the distance range 30 to 90 degrees (in per cent) as a function of ganitude, mb, or median of the detection thresholds (see Fig 36a-b)

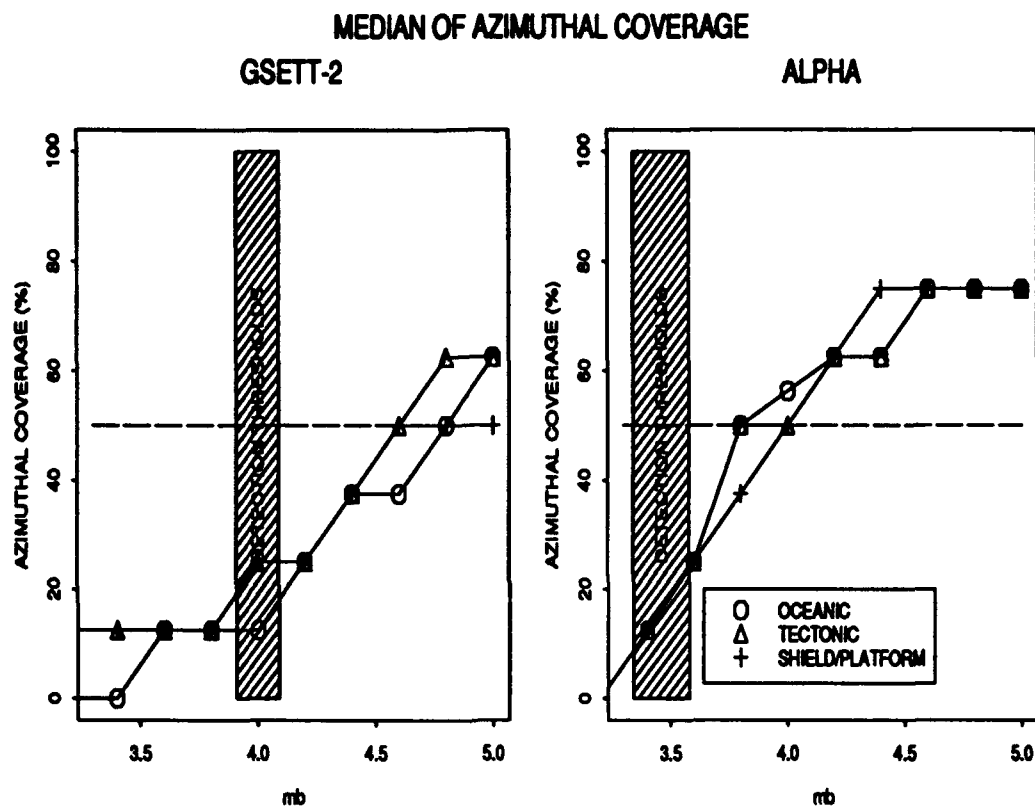


Figure 39: Median of azimuthal coverage given as the percentage of 8, 45 degree azimuth sectors in which the event was detected for the GSETT-2 and the ALPHA network. The shaded zones represent the median of the detection thresholds (see Fig 36a-b).

ber of 45 degree azimuthal sectors around the source to station azimuth that were covered by one or more detecting stations. Centering of the azimuth at the median of the station azimuth was done prior to the counting in order to avoid stations clustered in one 45 degree sector being counted as two sectors. The 50% coverage is indicated as a dashed line in the diagrams. Analysis of GSETT-2 indicated that 50% azimuthal coverage improves the probability of detecting and positively identifying depth phases. The curves in Figure 39 for the GSETT-2 network do not reach this level until well over half a magnitude unit above its detection thresholds, whereas this gap for the ALPHA network is less pronounced, but still significant. This means that for events between the detection threshold and the 50% level, the probability of detecting depth phases will be reduced.

Depth Errors Using S Phases

The use of S wave arrival times for the depth estimation is well established and its shortcomings and capabilities lend themselves more easily to modelling than do surface reflected phases. We employed the NetSim program with simulation parameters used for GSE by Bratt (1993) and describe the depth error with 90% confidence limits obtained by Monte Carlo simulations. In order to illustrate the effect of S waves on the estimated depth error we compare the ratio of the depth errors from determinations with only P waves and with both P and S waves in Figure 40. The event magnitude was set to $m_b=4.0$ and the depth to 25 km. There is, as one should expect, a general improvement - the ratio is larger than 1.0. However, there is also significant variation in the ratio; the median for the different geological regions varies from about 20 to 100%, but, as indicated by the ranges, improvements can be over 500%.

Figures 41 and 42 summarize simulations of the depth error for depth estimates based on S waves as a function of m_b for the three networks. The event is assumed to be at 25 km (indicated with a dashed horizontal line) and curves for the median and upper limit are shown in Figures 41 and 42, respectively. As in Figure 38 and 39, the range of the median detection thresholds (from Figure 36) are included in the diagrams for the sake of comparison. The curves for the ALPHA and the ALPHA+OCEAN networks in Figure 41 and 42 are quite similar suggesting very little effect of the oceanic stations on the depth error for events with magnitudes below 5.0. In order to achieve improvement of the ALPHA+OCEAN network relative to the ALPHA network, the detectability of the oceanic stations have to be enhanced.

For all three networks there is a clear gap between the depth estimation capability as described by the 90% error limits and the detection thresholds. We define the gap as the difference between the magnitude at which the 90% error equals 25 km (the actual depth of the event) and the 90% detection threshold. The gap is most pronounced for oceanic

SHIELD/PLATFORM: range= 0.9 - 2.18 median= 1.27 SD= 0.22
TECTONIC: range= 0.9 - 4.41 median= 1.4 SD= 0.31
OCEANIC: range= 0.8200000000000001 - 5.84 median= 2 SD= 0.78

Ratio of S and P depth error

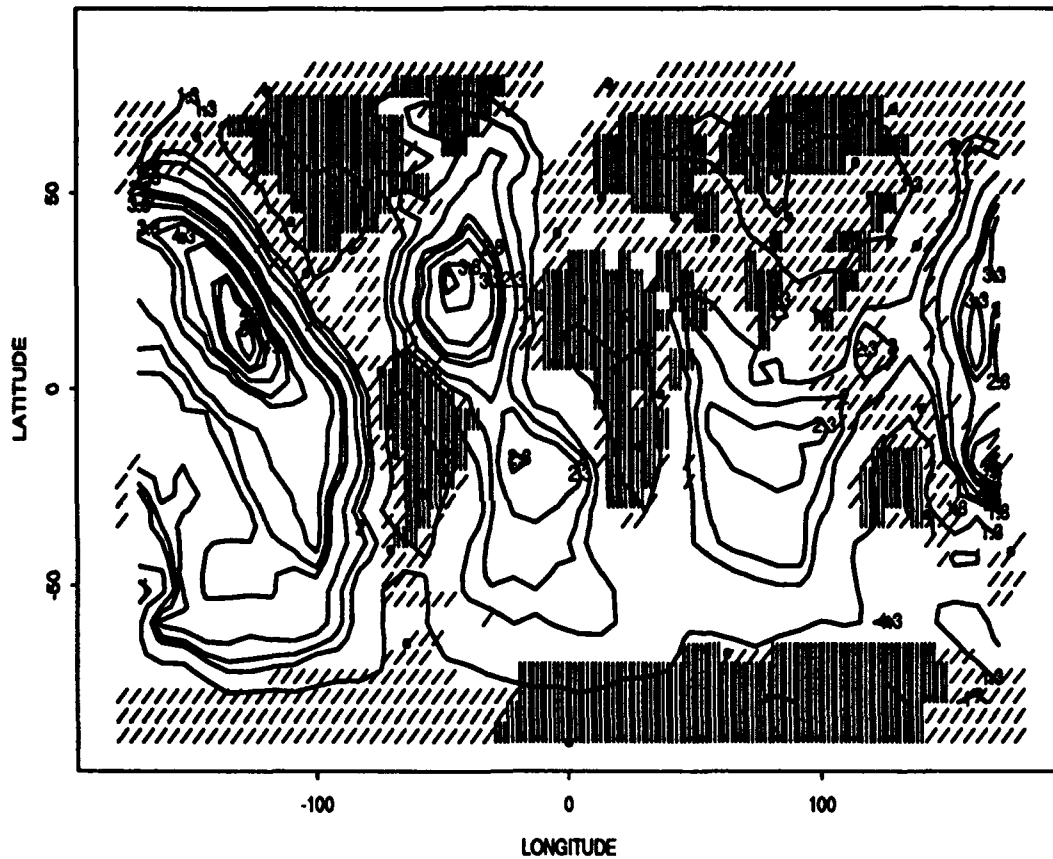


Figure 40: The ratio of depth errors from determinations with only *P* waves and with both *P* and *S* waves.

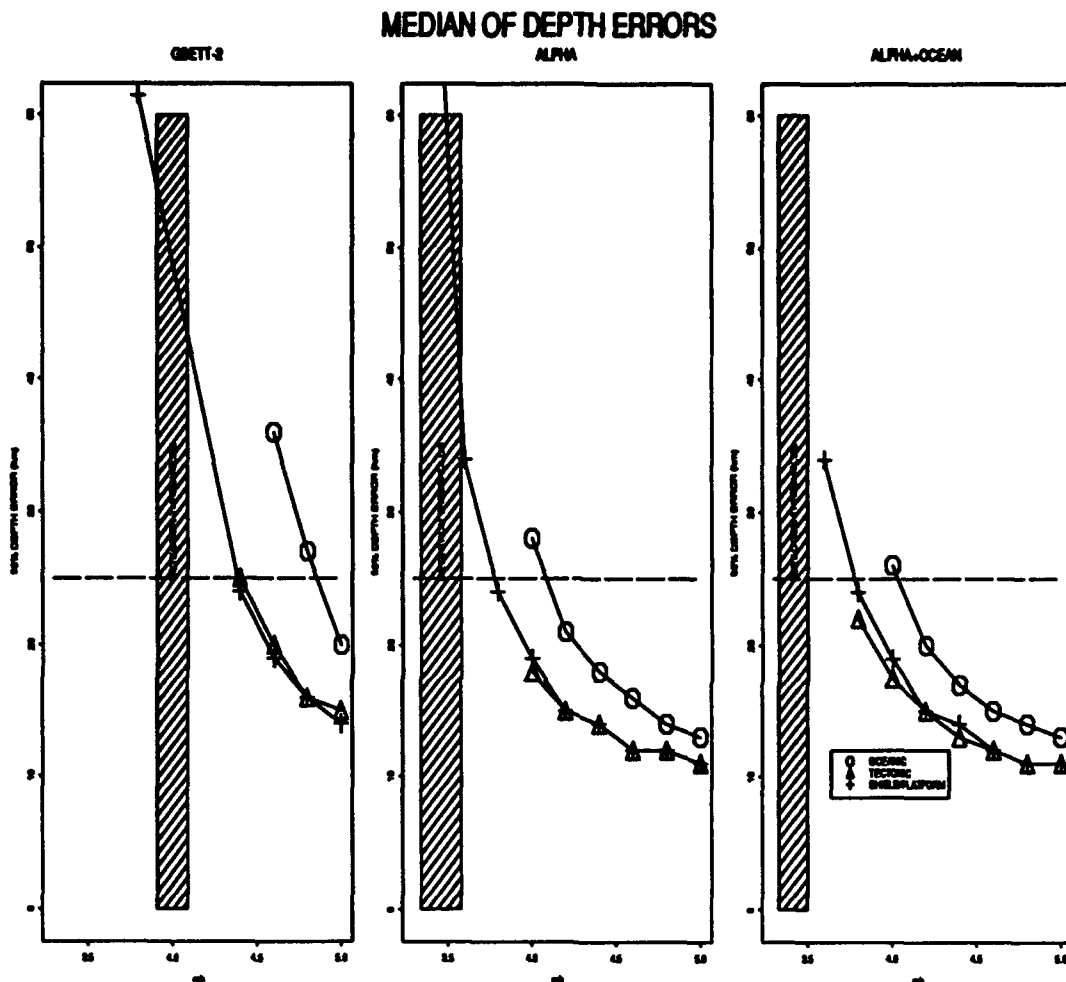


Figure 41: Median of depth error as a function of mb for estimates based on P and S waves for three networks: GSETT-2, ALPHA, and ALPHA + a 50 station oceanic network. The shaded zones represent the median of the detection thresholds (see Fig 36a-b).

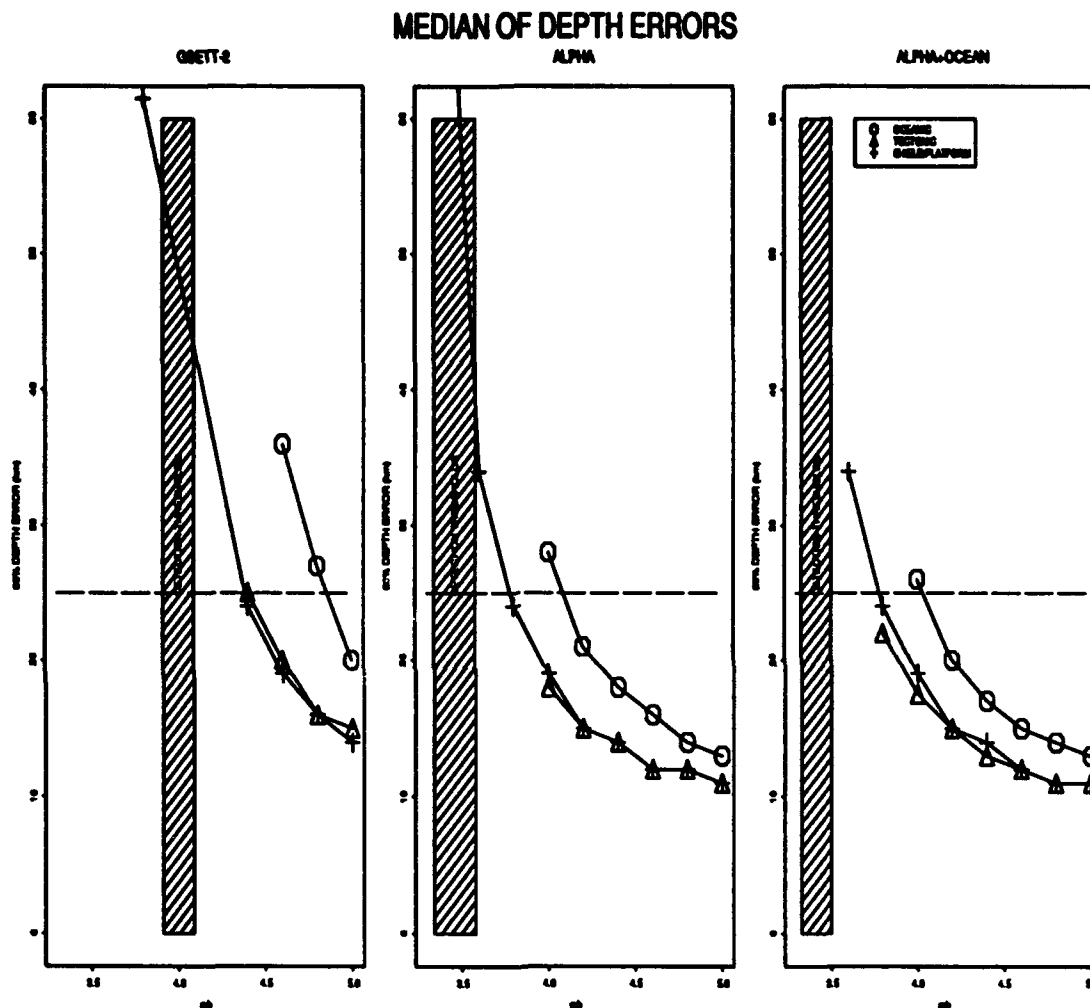


Figure 42: Upper limit of depth error as a function of m_b for estimates based on P and S waves for three networks: GSETT-2, ALPHA, and ALPHA + a 50 station oceanic network. The shaded zones represent the median of the detection thresholds (see Fig 36a-b).

structures for the GSETT network where it is almost one magnitude unit. For other cases it stays around 0.5 magnitude. The results in Figure 42, showing the upper limits of the depth error, show that the differences between oceanic and other structures are less pronounced than they are for the median value results in Figure 41. The gaps have, of course, widened compared to the median errors. For the GSETT network, the increase in the gap is dramatic, whereas for the ALPHA network it increases about 0.3 magnitude units for tectonic and shield/platform structure. The upper limit is perhaps conservative as a measure of the capability, but a large upper limit also reflects that there are areas with poor capability even if the median levels suggest a high capability.

One reason for the gap between detection threshold and depth estimation capability may be due to the apparent lower detection capability of S waves as illustrated by the example in Figure 43. Here the difference in detection thresholds (90%) for detecting both P and S waves, and only P waves at three stations is contoured. As S waves are often difficult to identify and properly time the requirement of detecting S waves at three stations rather than just the minimum one was used. The median difference in thresholds in Figure 43 is a few tenths of a magnitude unit, but, as indicated by the ranges, can reach higher values close to a magnitude unit.

The gap between detection and depth estimation capabilities means that some events will have depths that are only poorly determined. In order to illustrate this effect we applied the depth estimation simulations to the ALPHA network, not to events as a function of magnitude on an equally spaced grid, as above, but to events that model the world wide seismic activity. For this purpose we generated a sample of earthquakes corresponding to 5 days of activity with the simulation program by North (1983). This sample included 2997 events with magnitudes down to $m_b=2.58$. For each event, we then calculated the depth error using a large number of Monte Carlo simulations. The resulting depth errors are compared in Figure 44 with the actual depths of the synthetic events. Only events that were detected with 90% probability are included in the diagrams of Figure 44. In the left and right frames we show the differences between the 90% error and depth vs. magnitude and actual depth, respectively. Separate symbols - plus signs and open circles - are used for events with the difference less than and greater than 0 indicated as a dashed line. This separation maps events with acceptable and poorly determined depths relative to the actual depths. Events below the line would be "screened" as earthquakes, whereas data points above the dashed line are too large to allow such a classification. A screening level of 0 km may be too low for monitoring purposes and it may be more prudent to set it at, say 10 km. We note from the scatter diagram to the right that events with actual depths shallower than 10 km are generally not "screened" as earthquakes. This is desirable as they represent a depth shallow enough for at least theoretically be explosions. The 10 km depth line is indicated

SHIELD/PLATFORM: range= 0.14 - 0.79 median= 0.39 SD= 0.17
 TECTONIC: range= 0.14 - 0.77 median= 0.34 SD= 0.15
 OCEANIC: range= 0.17 - 0.67 median= 0.33 SD= 0.1

Difference in S and P detection capability

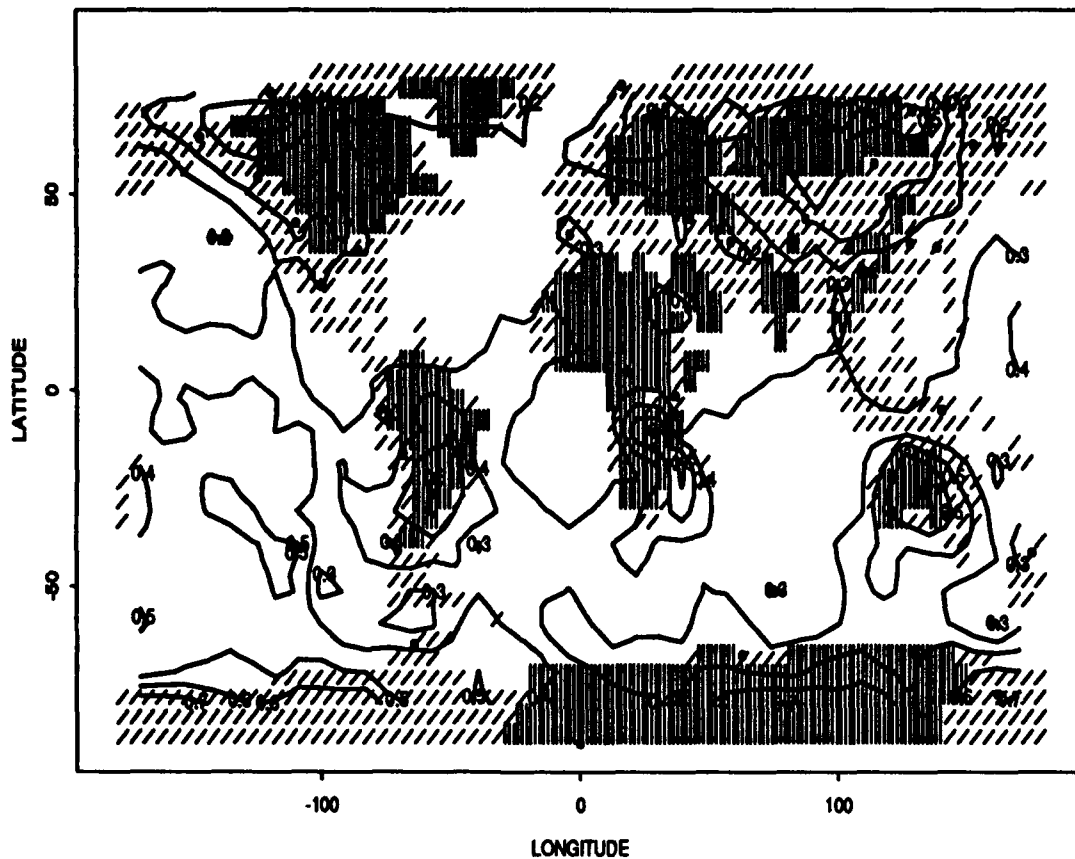


Figure 43: The difference in detection thresholds (90%) for detecting both P and S waves, and only P waves at three stations.

SHIELD/PLATFORM: range= 0.14 - 0.79 median= 0.39 SD= 0.17
 TECTONIC: range= 0.14 - 0.77 median= 0.34 SD= 0.15
 OCEANIC: range= 0.17 - 0.67 median= 0.33 SD= 0.1

Difference in S and P detection capability

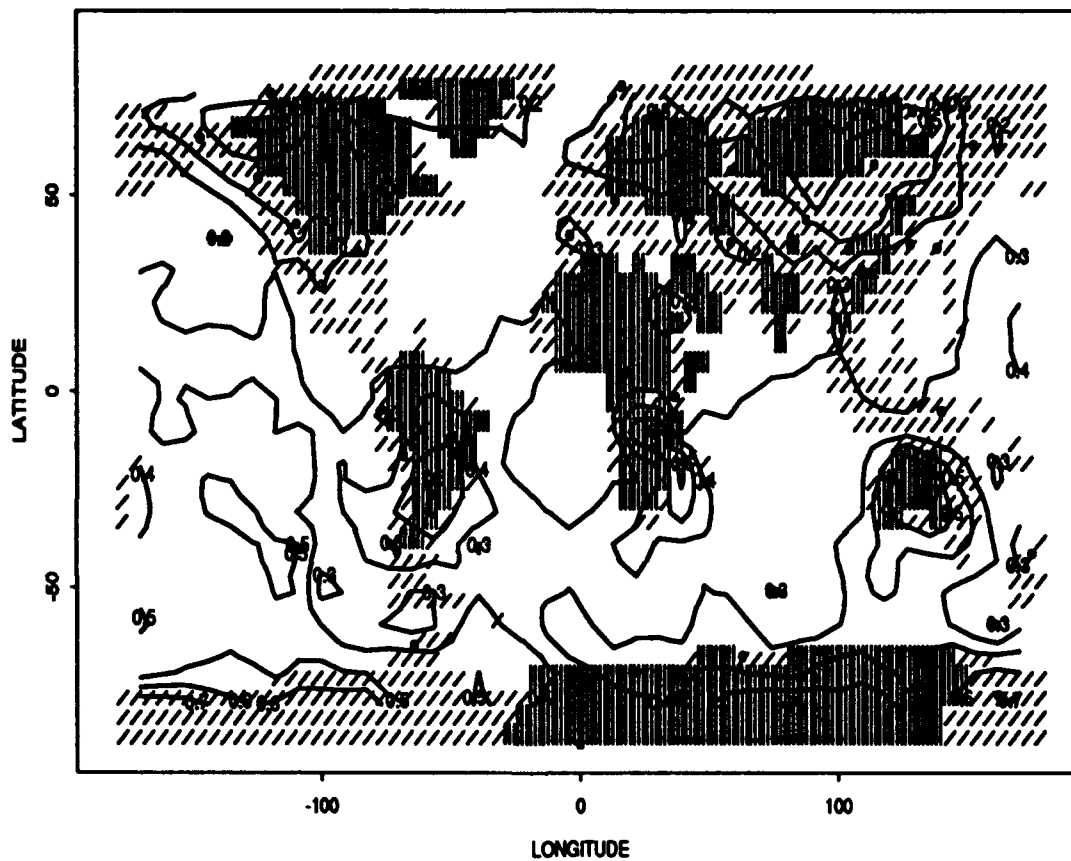


Figure 43: The difference in detection thresholds (90%) for detecting both *P* and *S* waves, and only *P* waves at three stations.

in the right frame, which also gives the number of events at depths below 10 km that are not screened, 135 or 27 events/day. This corresponds to about 25% of the total number of events that were detected with a 90% probability. Although the actual depth strongly determines this number, the left frame also indicates that these are primarily small events most of which have magnitudes less than $m_b=4.0$. The m_b detection thresholds (from Figure 36) are indicated in the left frame. Finally, the geographical distribution of the events are shown in Figure 45, where events that are above the "screening" line and at depths below 10 km are marked filled circles. There is no clear concentration of these events.

Concluding Remarks

The simulations and examples presented here suggest that the ALPHA network has not only a much lower and more geographically uniform detection threshold than the GSETT-2 network, but has a much improved depth estimation capability as well.

The simulations also suggest that only marginal improvements would be obtained by adding 50 oceanic stations to the ALPHA network, unless the sensitivity of these ocean based stations are significantly improved as compared to typical levels of stations in operation, currently and in the past.

Although the observability of depth phases is, in large degree, unpredictable and difficult to model generally, it appears that the ALPHA network is well distributed to observe such phases in the teleseismic window with regard to moveout of depth phases, as well as to azimuthal distribution around event azimuths. These qualities are reduced, however, near the detection threshold, and there is a gap of a few tenths of a magnitude unit where the probability of observing depth phases appears low.

There is a similar gap for depth estimates based on P and S wave arrival times. On the average, this gap does not appear as pronounced for events in tectonic and shield/platform areas. The simulations indicate that the gap is partly caused by the lower detection capability of S waves of the ALPHA network and therefore may be narrowed with enhanced detectability of S waves. The significance of narrowing the gap is illustrated with examples of synthetically generated events. A fairly large percentage of a large daily average of detected and located events at depths below 10 km would otherwise have poorly constrained depths. One important function of the BETA network of the GSE system would be to strengthen observations of S waves for depth determinations. The GAMMA network could also contribute in this regard, but its role in the GSE system is currently not clearly defined.

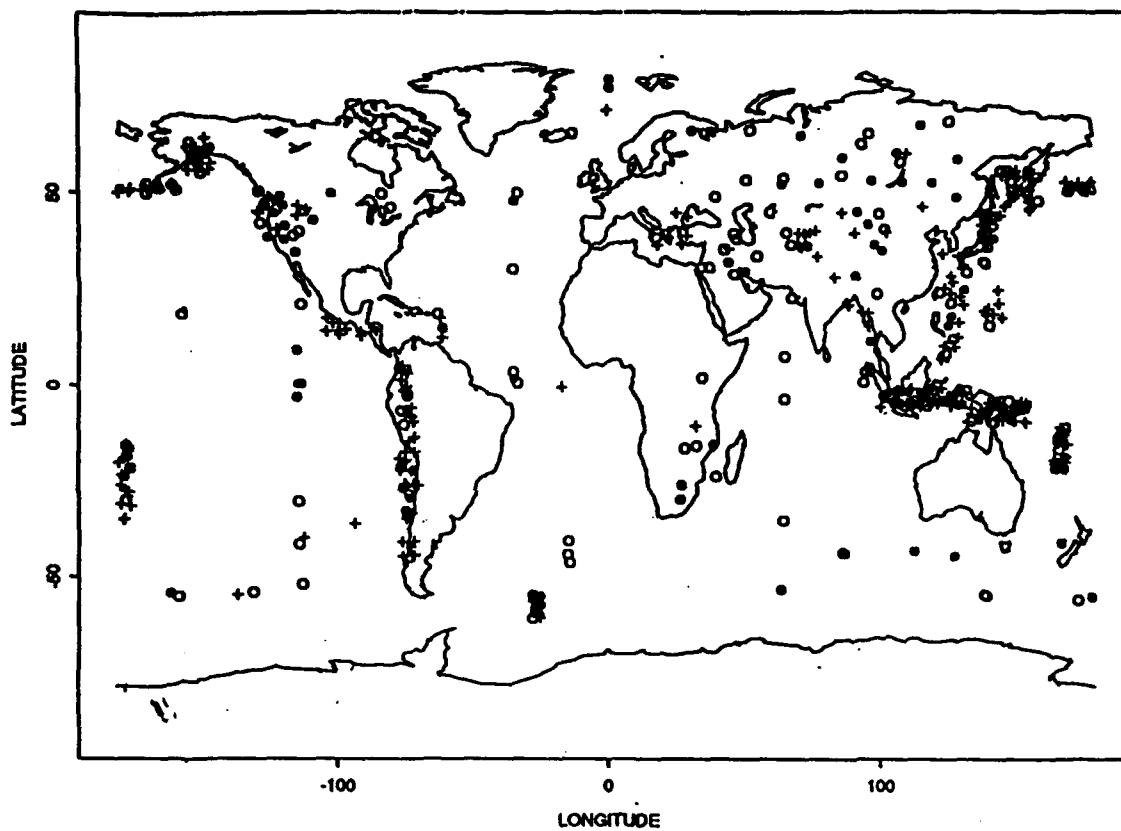


Figure 45: *The geographical distribution of the simulated events.*

References

- Bratt, S.R. (1992), GSETT-2: An experiment in rapid exchange and interpretation of seismic data, EOS, 48:513.
- Douglas, A., Richardson, L. and M. Hutchins (1990), Surface reflections and S-to-P conversions on P seismograms, Geophys. J. Int., 100:303-314.
- Gomberg, J.C., Shedlock, K.M. and S.R. Roecker (1990), The effect of S-wave arrival times on the accuracy of hypocenter estimation, Bull. Seism. Soc. Am., 80: 1605-1628.
- Hedlin, M.A.H. and J.A. Orcutt (1989), A comparative study of island, seafloor and sub-seafloor ambient noise level, Bull. Seism. Soc. Am., 79, 172-179.
- Jordan, T.H. (1981), Global Tectonic Regionalization for Seismological Data Analysis, Bull., Seism. Soc. Am., 71:1131-1141.
- North, R.G. (1983), Syntnetic Detection Generator - Program package, (manuscript).
- Phillips, J.D. and D.W. McCowan (1978), Ocean bottom seismometers for nuclear monitoring and research: a reassessment, in Seismic Discrimination, Semiannual Technical Summary 31 March 1978, Lincoln Laboratory, Lexington Mass.
- Ringdal, F. (1986), Study of Magnitudes, Seismicity, and Earthquake Detectability using a Global Network, Bull. Seism. Soc. Am., 76, 1641-1659.
- Sereno, T.J., Bratt, S.R. and G. Yee (1990), NetSim: A computer program for simulating detection and location capability of regional seismic networks, Annual. Tech. Rep. SAIC 90/1163, Sci. Appl. Int. Corp., San Diego, Calif., 1990.